Title

There's a Model for That: Memory, Propagation, and Prediction of Time-Dependent Electronic Structure

Author

Ranka, Karnamohit Ajit

Publication Date

2023

UNIVERSITY OF CALIFORNIA, MERCED

There's a Model for That: Memory, Propagation, and Prediction of Time-Dependent Electronic Structure

A dissertation submitted in partial satisfaction of the
requirements for the degree
Doctor of Philosophy

in

Computational Chemistry

by

Karnamohit Ranka

Committee in charge:

Dr. Hrant P. Hratchian, Chair
Dr. Christine M. Isborn, Advisor
Dr. Harish S. Bhat
Dr. Aurora Pribram-Jones
Dr. David Strubbe

2023

The dissertation of Karnamohit Ranka is approved, and it is acceptable in quality and form for publication on microfilm and electronically:

(Dr. Christine M. Isborn, Advisor)

(Dr. Harish S. Bhat)

(Dr. Aurora Pribram-Jones)

(Dr. David Strubbe)

(Dr. Hrant P. Hratchian, Chair)

University of California, Merced

2023

DEDICATION

To Kunal bhau and dadiji.

To my family.

EPIGRAPH

It does not matter how slowly you go as long as you do not stop.
—Confucius

TABLE OF CONTENTS

LIST OF FIGURES

LIST OF TABLES

ACKNOWLEDGEMENTS

I acknowledge the wisdom and support of my advisor, Dr. Christine Isborn, who has always been in my corner and given me valuable advice throughout my time at UC Merced. This endeavor would have been impossible without you.

I thank my collaborator and graduate committee member, Dr. Harish Bhat. You have taught me many things and have always been encouraging.

I thank my committee chair, Dr. Hrant Hratchian, who has provided valuable guidance, advice and help throughout my time in the Ph.D. program, and my committee members, Drs. Aurora Pribram-Jones and David Strubbe for their kind words and encouragement. I thank all my committee members for their valuable discussions and for their questions that led me to improve my research work.

I thank my mentor, Dr. Ajith Perera, for being kind to me during a part of my life when I needed it the most. I will forever be grateful to you for helping me with understanding and encouraging words which helped me to carry on.

I thank each member of my family for always being there for me, throughout the ups and downs of my life in India and the United States. Thank you for being so understanding, encouraging and for always looking out for me despite the distance between us.

Finally, I thank all the friends I have made thus far in my life, whether I have known you for a few minutes or many years. I would never have survived this journey were it not for every single one of you. You have given me the wisdom, opportunity, patience, courage and mental resilience necessary for me to be able to reach this stage of my life. Thank you!

VITA

2017	M. S. in Chemistry, University of Florida (Gainesville, Florida, United States)
2013	B. S. and M. S. in Chemistry, Indian Institute of Science Education and Research (IISER), Bhopal (Bhopal, Madhya Pradesh, India)

PUBLICATIONS

Ranka, K., Isborn, C.M. "Size-Dependent Errors in Real-Time Electron Density Propagation," *The Journal of Chemical Physics* 158(17), 174102 (2023). DOI: 10.1063/5.0142515

Gupta, P., Bhat, H.S., **Ranka, K.**, Isborn, C.M. "Statistical Learning for Predicting Density-Matrix Based Electron Dynamics," *Stat* 11, e439 (2021). DOI: 10.1002/sta4.439

Bhat, H.S., **Ranka, K.**, Isborn, C.M. "Machine Learning a Molecular Hamiltonian for Predicting Electron Dynamics," *International Journal of Dynamics and Control* 8, 1089-1101 (2020). DOI: 10.1007/s40435-020-00699-8

Ranka, K., Zhao, N., Yu, L., Stanton, J.F., Polfer, N.C. "Radical Rearrangement Chemistry in Ultraviolet Photodissociation of Iodotyrosine Systems: Insights from Metastable Dissociation, Infrared Ion Spectroscopy, and Reaction Pathway Calculations", *Journal of the American Society for Mass Spectrometry* 29, 1791-1801 (2018). DOI: 10.1007/s13361-018-1959-1

Ranka, K., Perera, A., Bartlett, R.J. "Elementary reaction profile and chemical kinetics study of [C(^{1}D)/(^{3}P) + SiH_4] with the CCSD(T) method", *Chemical Physics Letters* 680, 61-68 (2017). DOI: 10.1016/j.cplett.2017.05.024

ABSTRACT OF THE DISSERTATION

There's a Model for That: Memory, Propagation, and Prediction of Time-Dependent Electronic Structure

by

Karnamohit Ranka
Doctor of Philosophy in Computational Chemistry

University of California Merced, 2023

Dr. Hrant P. Hratchian, Chair

Time-dependent electronic structure is an important means to understand the dynamics of electrons, and thus the associated time-dependent mechanisms, in chemical systems of interest. A popular method to model and study electron dynamics is real-time time-dependent density-functional theory, or RT-TDDFT. In practice, the implementation of RT-TDDFT (as well as linear response TDDFT) makes an approximation known as the adiabatic approximation, where the dependence of electron density at the current moment of time on that at previous moments in time (as well as the many-body interacting and non-interacting Kohn-Sham wave-functions) is completely ignored. Maitra et al have shown that this approximation fails for model systems, but the effects of this approximation with varying system-size are not known. We study electron dynamics of systems exhibiting charge-transfer by resonantly perturbing them and conclude that size-dependent errors, evaluated in terms of peak-shifting in linear absorption spectra and Rabi cycle dynamics, get progressively smaller as the system-size increases. Statistical learning methods have been shown to have an increasingly wide scope with respect to property prediction in quantum chemical problems in recent times. However, their use for predicting electron dynamics has been relatively underexplored. In collaboration with Dr. Bhat and his group (Applied Math, UC Merced), with a goal to train a Hamiltonian model for predicting accurate density evolution, we demonstrate that one can use time-dependent density-matrix trajectories to learn molecular electronic Hamiltonians which can be used to propagate density-matrices under arbitrary electric-field perturbations. In an effort to apply such learning methods to density-matrix data obtained from accurate wave-function methods such as time-dependent configuration interaction (TDCI), we explore the amount of memory required to reproduce accurate TDCI singles (TDCIS) density-matrix evolution in some molecular systems for various perturbations. In doing so successfully, we hope to explore the structure and application of statistical learning methods for training Hamiltonian models on accurate time-dependent electron-density data, predicting single reference density-matrix evolution and informing the construction of memory-inclusive exchange-correlation functionals in TDDFT.

Chapter 1

Introduction

1.1 The Schrödinger Equation

Electronic motion and distribution play a crucial role in determining the physical and chemical properties of atoms, molecules, ions, and matter in general. While negatively charged electrons have a low rest mass and can travel at speeds approaching that of light, most commonly available materials have electrons bound to relatively heavy, spatially small nuclear centers (comprised of neutrons and positively charged protons). Electronic and nuclear motion in most of these materials can be described using the time-dependent Schrödinger equation (TDSE), given as follows:

$$i\hbar\frac{\partial}{\partial t}\Psi(\mathbf{x},\mathbf{X},t) = \hat{\mathcal{H}}(\mathbf{x},\mathbf{X},t)\Psi(\mathbf{x},\mathbf{X},t), \tag{1.1}$$

where $\hat{\mathcal{H}}$ is the molecular Hamiltonian made up of one- and two-particle operators, and Ψ is the many-body molecular wave function, and $\mathbf{x}(\equiv \{\mathbf{r}_i, \sigma_i\})$ as well as $\mathbf{X}(\equiv \{\mathbf{R}_A, \mathbf{I}_A\})$ represent the collective spin and spatial coordinates of all the electrons and nuclei in the molecular system, respectively.

The externally unperturbed non-relativistic Hamiltonian used in Eq. (1.1) is:

$$\begin{aligned}\hat{\mathcal{H}}(\mathbf{x},\mathbf{X},t) \equiv \hat{\mathcal{H}}(\mathbf{r},\mathbf{R}) = &-\sum_A \frac{\hbar^2}{2m_A}\nabla^2_{\mathbf{R}} - \sum_i \frac{\hbar^2}{2m_e}\nabla^2_{\mathbf{r}_i} \\ &+ \frac{e^2}{4\pi\epsilon_0}\left(\sum_A\sum_B \frac{Z_A Z_B}{|\mathbf{R}_A - \mathbf{R}_B|} - \sum_A\sum_i \frac{Z_A}{|\mathbf{r}_i - \mathbf{R}_A|} + \sum_i\sum_{j<i}\frac{1}{|\mathbf{r}_i - \mathbf{r}_j|}\right).\end{aligned} \tag{1.2}$$

Here, $\hat{\mathcal{H}}$ is the molecular Hamiltonian, $-\frac{\hbar^2}{2m_\eta}\nabla^2_\eta$ is the kinetic energy operator for the particle whose spatial coordinates and mass are given by η and m_η, respectively, and the rest of the terms are two-body Coulomb operators describing nuclear-nuclear, electron-nuclear and electron-electron interactions. Z_A is the (positive) nuclear charge on nucleus A, $\mathbf{R}_A$ and $\mathbf{r}_i$ are the coordinates of nucleus A and electron i.

The molecular wave function is commonly factored into its nuclear and electronic parts, made possible by the fact that the electronic and nuclear motion occur on different timescales and thus their equations of motion can be separated. The Hamiltonian of the system becomes a sum of the separate nuclear and electronic one- and two-body terms and the two-body electron-nuclear interaction is parametrized by the molecular geometry: the nuclei are assumed frozen. This is known as the Born-Oppenheimer approximation, and it leads to factorization of the molecular wave function:

$$\Psi(\mathbf{x}, \mathbf{X}, t) = \Psi_n(\mathbf{X}, t)\Psi_e(\mathbf{x}, t; \mathbf{X}) \tag{1.3}$$

This allows one to split the Hamiltonian into an electronic part and a nuclear part. The relatively massive nuclei are often treated classically, and the problem boils down to solving the electronic TDSE (presented in atomic units below, which are used throughout the rest of this text):

$$i\frac{\partial}{\partial t}\Psi_e(\mathbf{x}, t; \mathbf{R}) = \hat{\mathcal{H}}_e(\mathbf{r}, t; \mathbf{R})\Psi_e(\mathbf{x}, t; \mathbf{R}), \tag{1.4}$$

where $\hat{\mathcal{H}}_e$ is the electronic Hamiltonian. It is:

$$\hat{\mathcal{H}}_e(\mathbf{r}, t; \mathbf{R}) = -\sum_i \frac{\hbar^2}{2m_e}\nabla^2_{\mathbf{r}_i} - \frac{e}{4\pi\epsilon_0}\sum_A\sum_i \frac{Z_A}{|\mathbf{r}_i - \mathbf{R}_A|} + \frac{e^2}{4\pi\epsilon_0}\sum_i\sum_{j<i}\frac{1}{|\mathbf{r}_i - \mathbf{r}_j|}. \tag{1.5}$$

Eq. (1.4) is a partial differential equation. Its exact solution is often impractical except for systems with a small number of electrons. However, one can proceed towards an approximate solution by assuming that Ψ_e can be described by a single Slater determinant built from a set of N one-electron wave functions or “orbitals” in an N-electron system (this is the case in the Kohn-Sham and the Hartree-Fock formalisms).[1, 2] Such an assumption may fail to adequately describe effects of relatively stronger electron correlation in certain systems, but this can be rectified by incorporating determinants built from other combinations of N orbitals chosen from a larger set of one-electron functions.[3, 4] Furthermore, in the cases presented in this dissertation, we will assume clamped nuclei. This is a fairly accurate approximation for fast electronic processes on the attosecond and femtosecond timescales.

The methods of propagation presented in this dissertation, time-dependent configuration interaction singles (TDCIS) and real-time time-dependent Hartree-Fock (RT-TDHF) theories, share the Hartree-Fock wavefunction as their ground state. The two techniques have also been shown to exhibit similar time-dependent behavior in some cases.[5] However, there are some key differences between the two methods in terms of how they incorporate the time-dependence of electronic motion, outlined in the proceeding sections.

1.2 Time-independent Methods

1.2.1 Hartree-Fock (HF) theory

The TDSE reduces to the time-independent version for stationary states, where one assumes separation of the time and electronic position variables due to stationarity of the wave function:[6]

$$\hat{\mathcal{H}}_{e,0}(\mathbf{x}, \mathbf{x}')\Psi_e^k(\vec{\mathbf{x}}) = E_e^k \Psi_e^k(\vec{\mathbf{x}}). \tag{1.6}$$

Here, E_e^k corresponds to the energy of the k-th electronic state.

In the case of a mean-field theory like the Hartree-Fock approximation Eq. (1.6) reduces to a set of self-consistent field (SCF) equations known as the HF equations:

$$\hat{f}(\mathbf{x})\phi_k(\mathbf{x}) = \varepsilon_k \phi_k(\mathbf{x}), \tag{1.7}$$

with $\hat{f}$ denoting the effective single-electron Fock operator, and ϕ_k being the k-th molecular orbital (MO). The number of MOs must be at least equal to the number of electrons and is usually greater, say M. The Hartree-Fock wave function, a single Slater determinant, is built from the MOs corresponding to the N lowest eigenvalues in Eq. (1.7), leading to a total of N occupied MOs and $(N-M)$ virtual MOs.

For the present case, the spatial parts of the electrons with α and β spins are restricted to be the same (i.e., all the electrons in the system are spin-paired) . This is known as the restricted HF (RHF) reference[7], and discussion pertains to this special case for the rest of the text.

The Fock operator in Eq. (1.7) is given by the following in atomic units (used throughout the rest of this text):

$$\begin{aligned}\hat{f}(\mathbf{x}) = &\left[-\frac{\nabla_{\mathbf{r}}^2}{2} - \sum_A \frac{Z_A}{|\mathbf{r}-\mathbf{R}_A|} + \hat{V}_{\text{ext}}(\mathbf{r})\right] \\ &+ \sum_j^{N/2} \left[2 \times \int d\mathbf{r}' \frac{\phi_j^*(\mathbf{r}')\phi_j(\mathbf{r}')}{|\mathbf{r}-\mathbf{r}'|} - \int d\mathbf{r}' \frac{\phi_j^*(\mathbf{r}')\mathfrak{P}(\mathbf{r},\mathbf{r}')\phi_j(\mathbf{r}')}{|\mathbf{r}-\mathbf{r}'|}\right],\end{aligned} \tag{1.8}$$

where $\mathfrak{P}$ is a two-electron permutation operator.

The HF wave function is constructed from the $(N/2)$ doubly occupied MOs as:

$$\Phi_{\text{HF}}(\vec{\mathbf{x}}) = \frac{1}{\sqrt{N!}}\mathcal{A}(\prod_i^{\text{occ.}} \phi_i), \tag{1.9}$$

where $\mathcal{A}$ is an anti-symmetry operator. Eq. (1.9) is the starting point for both the TDCIS (via the CIS method) and the RT-TDHF methods.

1.2.2 Configuration Interaction (CI) and Complete Active Space SCF (CASSCF) methods

CI singles (CIS) A natural step towards incorporating excited states into the electronic structure of the system is including the single-electron transitions between the occupied ($\{i, j, k\}$) and the unoccupied ($\{a, b, c\}$) orbitals obtained by solving the HF equations

$$\Psi_{\text{CIS}}^K(\vec{\mathbf{x}}) = \sum_{i,a} c_{ia}^K \Phi_i^a \tag{1.10}$$

Ψ_{CIS}^K is the configuration interaction singles (CIS) ansatz[8] for the wave function corresponding to the stationary state K of the system under consideration. It is a linear combination of the singly-substituted, spin-adapted Slater determinants built from the HF wave function (which represent the one-electron transitions).[1] We assume the CI coefficients c_ζ^K are normalized. In general, the CI wave functions correspond to the eigenstates of the system's field-free Hamiltonian and must satisfy Eq. (1.6). In the case of CIS, the ground state is the state described by the HF wave function. However, this is not generally true for a CI wave function if one includes two-electron transitions (doubles) or beyond in the ansatz, which add correlation to the ground state HF reference.[9]

Full CI Upon incorporating all possible N-tuply-substituted Slater determinants into the CI wave function, we get for the state K (analogous to Eq. (1.10))

$$\Psi_{\mathrm{FCI}}^K(\vec{\mathbf{x}}) = c_{\mathrm{HF}}^K \Phi_{\mathrm{HF}} + \sum_{i,a} c_{ia}^K \Phi_i^a + \sum_{i,j,a,b} c_{ijab}^K \Phi_{ij}^{ab} + \sum_{i,j,k,a,b,c} c_{ijkabc}^K \Phi_{ijk}^{abc} + \dots \qquad (1.11)$$

This gives us the full CI ansatz for the electronic wave function. Going beyond CIS means incorporating at least the doubly-substituted determinants into the wave function. In general, the ground state energy and wave function of an electronic system is determined variationally[7], which means the energy of the system is minimized with respect to the wave function, yielding optimized ground state and excited state wave functions (and, accordingly, a set of MO expansion coefficients, explained in Sec. 1.3.2, and CI coefficients). As this process involves taking expectation values of the Hamiltonian, which contains at most two-body operators, there are contributions from other $N > 1$-tuply substituted determinants to the ground state energy and wave function of the system: directly from the doubly-substituted determinants (via Slater-Condon rules[7] for integrals between the HF and doubly-substituted determinants), and indirectly from $N > 2$-tuply substituted determinants (via Slater-Condon rules for integrals between the doubly- and at most quadruply-substituted determinants, between triply- and at most pentuply-substituted determinants, and so on).

---

[1] the Brillouin theorem[7] and the fact that eigenstates of the Hamiltonian are orthogonal to each other ensure that the HF wave function does not have any contribution to the excited states and the singly-substituted Slater determinants do not contribute to the ground state in the CIS theory.

CASSCF It is apparent that the number of determinants needed to be incorporated into a full CI wave function ansatz grows exponentially with the number of electrons and the number of orbitals. This makes full CI a computationally infeasible method for larger systems. However, not all determinants contribute significantly towards improving the incorporation of electronic correlation, and often it is the substituted determinants involving frontier orbitals or orbitals of appropriate symmetry that are the most important for this purpose.[9, 10] In such cases, the truncation of the full CI ansatz can be achieved by restricting the set of orbitals (and indirectly the degree of substitution in the Slater determinants) considered for the CI expansion. This is known as choosing a complete active space (CAS). As is the case in full CI, the CAS coefficients (CI coefficients of the CAS truncation) are optimized to yield the ground state and excited state wave functions. If, in the process, the MO expansion coefficients from the SCF procedure outlined in Sec. 1.2.1 are also optimized, the method is known as CASSCF.

$$\begin{aligned}\Psi^K_{\text{CASSCF}}(\vec{\mathbf{x}}) = c^K_{\text{HF,CAS}}\Phi_{\text{HF,CAS}} + \sum_{i,a\in\text{CAS}} c^K_{ia}\Phi^a_i \\ + \sum_{i,j,a,b\in\text{CAS}} c^K_{ijab}\Phi^{ab}_{ij} + \sum_{i,j,k,a,b,c\in\text{CAS}} c^K_{ijkabc}\Phi^{abc}_{ijk} + \dots\end{aligned} \tag{1.12}$$

The electronic energies and properties calculated from the CASSCF method are typically not straightforward to converge and are sensitive to the choice of the active space.[9, 10] However, a sufficiently large active space approaching the size of the full CI wave function leads to accurate energies and properties within a given finite basis set size.

1.3 Time-dependent methods

1.3.1 Time-dependent CI singles (TDCIS)

Building upon the stationary HF ground state and CIS excited states (Eqs. (1.9) and (1.10)), and by using the superposition principle, we can further construct a *time-dependent* electronic wave function as a linear combination of the CIS wave functions:

$$\Psi_{\text{TDCIS}}(\vec{\mathbf{x}},t) = \sum_K a_K(t)\Phi^K_{\text{CIS}}(\vec{\mathbf{x}}) \tag{1.13}$$

Substituting Eq. (1.13) in Eq. (1.1) and using Eq. (1.6) gives a set of coupled equations:[11]

$$\begin{aligned} i\frac{\partial}{\partial t}a_M(t) &= \sum_N a_N(t)\langle\Psi^M_{\text{CIS}}|\hat{\mathcal{H}}_{e,0} + \hat{V}_{\text{ext}}|\Psi^N_{\text{CIS}}\rangle(t) \\ &= \sum_N a_N(t)\langle\Psi^M_{\text{CIS}}|\hat{\mathcal{H}}_e|\Psi^N_{\text{CIS}}\rangle(t). \end{aligned} \tag{1.14}$$

In matrix-form, we get:

$$i\frac{\partial}{\partial t}\vec{a}(t) = \mathrm{H}_e(t)\vec{a}(t). \tag{1.15}$$

Here, $\vec{a}$ is the time-dependent TDCIS wave function represented as a state-vector in the basis of the stationary CIS states. One way to solve Eq. (1.15) is to use the first order term of the Magnus expansion[12–14] as an approximation of the differential equation's solution:

$$\vec{a}(t+\Delta t) = \exp(-i\Delta t(\mathrm{H}_{e,0} + \mathrm{V}_{\text{ext}}(t)))\vec{a}(t). \tag{1.16}$$

One can obtain accurate electron dynamics by solving the TDCI equation of motion, Eq. (1.14), for various higher-order CI ansatzes beyond CIS.[11, 15–19] While the scaling of TDCI methods can be factorial in the number of electrons within the molecular system when using full CI, truncated CI ansatzes can be used to save computational costs, but are often still computationally more expensive than TDHF and TDDFT methods.[20, 21]

The set of reference orbitals, obtained upon solving the HF equations in the present case, and the subsequent CI states built from the corresponding Slater determinants remain unchanged during the TDCI propagation of the system's electronic wave function for a given molecular geometry. The time-dependence is incorporated entirely through the time-dependent expansion coefficients in the many-body TDCI wave function in the case where an external field is not applied.

1.3.2 Real-time time-dependent Hartree-Fock theory (RT-TDHF)

Time-dependent Hartree-Fock (TDHF) theory[22] evolves the one-electron orbitals in the HF theory according to the time-dependent Schrodinger equation for one particle. This results in a Liouville-von Neumann equation involving the time-dependent Fock operator:[23]

$$i\frac{\partial}{\partial t}\mathrm{P}'(t) = [\mathrm{F}'(t), \mathrm{P}'(t)]. \tag{1.17}$$

where F is the Fock matrix, and the primes denote that the basis in which the matrices are represented is orthogonal.

If the time-dependent HF orbitals, $\{\phi_i\}$, are expanded as linear combinations of a set of basis functions, $\phi_k(\mathbf{r},t) = \sum_\mu c_{\mu k}(t)\chi_\mu(\mathbf{r})$ ($\{c_{\nu i}\}$ being known as MO expansion coefficients), then we can define the density-matrix and the Fock matrix elements to be:

$$\mathrm{P}_{\mu\nu}(t) = 2\sum_i^{\mathrm{occ}} c_{\mu i}(t)c^*_{\nu i}(t), \tag{1.18}$$

$$\begin{aligned}\mathrm{F}_{\mu\nu}(t) = &\int d\mathbf{r}\ \chi^*_\mu(\mathbf{r})\Big[-\frac{\nabla^2_{\mathbf{r}}}{2} - \sum_A \frac{Z_A}{|\mathbf{r}-\mathbf{r}'|} + \hat{V}_{\mathrm{ext}}(\mathbf{r},t)\Big]\chi_\nu(\mathbf{r})\\ &+\int\int d\mathbf{r}\ d\mathbf{r}'\ \chi^*_\mu(\mathbf{r})\sum_{\lambda,\sigma}\Bigg[\frac{\chi^*_\lambda(\mathbf{r}')}{|\mathbf{r}-\mathbf{r}'|}\cdot[\mathrm{P}_{\lambda\sigma}\chi_\sigma(\mathbf{r}')\chi_\nu(\mathbf{r}) - \mathrm{P}_{\lambda\nu}\chi_\nu(\mathbf{r}')\chi_\sigma(\mathbf{r})]\Bigg].\end{aligned} \tag{1.19}$$

For the initial condition, Eq. (1.7) is solved and P(0) is formed from the occupied orbitals, each corresponding to an eigenvector of the field-free Fock operator F(0). F(0) and P(0) are transformed to an orthogonalized basis, $\{\chi'_\mu(\mathbf{r})\}$.

Eq. (1.17) can then solved discretely, where we here use the modified mid-point unitary transformation (MMUT) algorithm. MMUT propagation involves two steps: (1). building a unitary propagator, U, from F′; (2). using U to propagate P′,[23–26]

$$\begin{aligned}\mathrm{U}_m &= e^{-2i\mathrm{F}'(m)\Delta t},\\ \mathrm{P}'(m+1) &= \mathrm{U}_m\mathrm{P}'(m-1)\mathrm{U}^\dagger_m.\end{aligned} \tag{1.20}$$

Here, m denotes the time-step and Δt denotes the step-size. The matrix exponential term in Eq. (1.20) is evaluated by diagonalizing F' and U can be constructed using the eigenvectors and eigenvalues:

$$\begin{aligned}
\varepsilon(m) &= \mathrm{C}(m)\mathrm{F}'(m)\mathrm{C}^{\dagger}(m);\\
\mathrm{U}_m &= \mathrm{C}^{\dagger}(m)e^{-2i\varepsilon(m)\Delta t}\mathrm{C}(m),\\
\mathrm{P}'(m+1) &= \mathrm{U}_m\mathrm{P}'(m-1)\mathrm{U}_m^{\dagger}.
\end{aligned} \tag{1.21}$$

The MMUT propagation is restarted every 100 timesteps using what is called the Magnus 2[27] or EM2[28] propagator, to correct for energy drift that is often an artifact of leap-frog methods like MMUT:

$$\begin{aligned}
\mathrm{U}''_{k\tau} &= e^{-i\mathrm{F}'(k\tau)\Delta t},\\
\mathrm{P}''(k\tau+1) &= \mathrm{U}''_{k\tau}\mathrm{P}'(k\tau)\mathrm{U}''^{\dagger}_{k\tau},\\
\mathrm{F}''(k\tau+1) &\equiv \mathrm{F}''(\mathrm{P}''(k\tau+1), k\tau+1),\\
\mathrm{F}_{\mathrm{avg}}(k\tau, k\tau+1) &= \frac{1}{2}[\mathrm{F}'(k\tau)+\mathrm{F}''(k\tau+1)];\\
\mathrm{U}_{k\tau,\mathrm{EM2}} &= e^{-i\mathrm{F}_{\mathrm{avg}}(k\tau,k\tau+1)\Delta t},\\
\mathrm{P}'(k\tau+1) &= \mathrm{U}_{k\tau,\mathrm{EM2}}\mathrm{P}'(k\tau)\mathrm{U}^{\dagger}_{k\tau,\mathrm{EM2}}.
\end{aligned} \tag{1.22}$$

Here, $\tau(=100)$ is the number of timesteps after which the MMUT propagation is restarted, and $k(=0,1,2,3...)$ is an integer.

1.3.3 Real-time time-dependent density functional theory (RT-TDDFT)

Density-functional theory (DFT), a ground-state formulation, maps the one-body electron density of a many-body, interacting wave function to an external potential.[29] The corresponding Kohn-Sham (KS) formalism uses a fictitious system of non-interacting electrons to calculate the one-electron density in a self-consistent manner (similar to the HF equations, Eq. (1.7)).[30–33] The time-dependent counterpart of the KS formalism (TDKS), following from Eq. (1.1) and the Runge-Gross theorem[34], is described by the following equation:[35, 36]

$$i\frac{\partial}{\partial t}\phi_i^{\mathrm{KS}}(\mathbf{x},t) = \hat{h}_S[n,\{\phi_j^{\mathrm{KS}}\}](\mathbf{x},t)\phi_i^{\mathrm{KS}}(\mathbf{x},t), \tag{1.23}$$

where $\hat{h}_S$ is the KS Hamiltonian for a single electron, $\{\phi_i^{\text{KS}}\}$ are the KS orbitals and n is the one-electron density of the restricted, closed-shell system under consideration:

$$n(\mathbf{r}, t) = 2 \sum_i^{\text{occ}} |\phi_i^{\text{KS}}(\mathbf{r}, t)|^2. \tag{1.24}$$

Eq. (1.23) can be used to describe the evolution of the one-electron density, $n(\mathbf{r}, t)$, which is considered a fundamental quantity in TDDFT. Equivalently, when describing the evolution of the corresponding one-electron density-matrix, denoted P, it takes the form of the Liouville-von Neumann equation:[37]

$$i \frac{\partial}{\partial t} \mathrm{P}(t) = [\mathrm{H}_S(t), \mathrm{P}(t)]. \tag{1.25}$$

H_S represents the Hamiltonian matrix in a chosen orthogonal basis (which can be the KS orbitals or orthogonalized basis functions used to linearly expand the KS orbitals) and P represents the density-matrix in the same basis. The square brackets in Eq. (1.25) indicate the commutator between H_S and the density-matrix P.

The KS Hamiltonian, as any DFT Hamiltonian, is a functional of the time-dependent one-electron density (and in particular of the KS orbitals). The dependence of $\hat{h}_S$ on $n(\mathbf{r}, t) (\equiv n_t)$ (equivalently, that of $\mathrm{H}_S(t)$ on $\mathrm{P}(t)$) results in a nonlinear set of equations similar to the Hartree-Fock equations. The one-electron density produced by evolving the KS orbitals must always be equal to the interacting system's evolving density given both Hamiltonians include the same external potential.[38, 39] This poses some restrictions on the KS Hamiltonian, which is

$$\begin{aligned} \hat{h}_S[n, \{\phi_j^{\text{KS}}\}](\mathbf{x}, t) = &- \frac{\nabla_{\mathbf{r}}^2}{2} - \sum_A \frac{Z_A}{|\mathbf{r} - \mathbf{R}_A|} + \hat{V}_{\text{ext}}(\mathbf{r}, t) \\ &+ \int d\mathbf{r}' \frac{n(\mathbf{r}', t)}{|\mathbf{r} - \mathbf{r}'|} + v_{\text{XC}}[n_t, n_{t'<t}, \Psi_0, \Phi_0](\mathbf{r}, t). \end{aligned} \tag{1.26}$$

The fourth term in Eq. (1.26) is known as the Hartree potential, and corresponds to the mean-field electron-electron interaction energy contribution from the Coulomb operator, whereas v_{XC} is known as the exchange-correlation (XC) potential and is defined as the functional derivative of the XC energy with respect to the one-electron density. As the TDKS Hamiltonian must reproduce the interacting system's one-electron density and as the other terms in the TDKS Hamiltonian are only dependent on the instantaneous density distribution n_t, $v_{XC}(\mathbf{r}, t)$ must incorporate the initial state dependence (on both the interacting system one, Ψ_0, and the Kohn-Sham one, Φ_0) as well as the dependence on the intermediate TDKS densities $n_{t'<t}$, collectively known as "memory effects" (discussed further in Section 1.3.3.1).[38]

Such restriction on the XC potential of the Kohn-Sham Hamiltonian manifests as several exact conditions the XC potential, the Kohn-Sham density, and related quantities must satisfy in order for the density propagation to be exact, two of which are relevant to this study: (1). the adiabatic theorem, which states that the limit of a sufficiently slowly varying exact time-dependent XC potential is the exact ground-state XC potential corresponding to the density at a given time, and (2). the resonance condition, which implies that resonant frequencies of an exactly evolving system must not change with time.[38–41]

While incorporating memory effects completely within the XC potential allows one to propagate the one-electron density (or the corresponding density-matrix) exactly as the interacting system's using the TDKS method, the mathematical form of the effects is often unknown except for very small model systems where it can be numerically calculated. In practice, when using the real-time TDKS (RT-TDKS) method, the memory effects are often ignored. This assumption leads to what is known as the "adiabatic approximation", where the XC potential used corresponds to that of a system in its ground-state, with n_t input as its ground-state density. The adiabatic approximation does appear to work well in some instances, such as ionization,[42–45] where the electron removal may keep the system closer to the neutral reference state compared to electron excitation; however, it has been shown to fail for small, model systems, for example, those exhibiting charge-transfer nature in the excited state[38, 46]. While there are several proposed XC functionals and time-dependent formulations that incorporate memory effects at least partially, none of them satisfy the resonance condition, an important consideration when modelling coherent electron dynamics accurately.[47–50]

1.3.3.1 A note on memory effects

Hohenberg and Kohn, in 1964, proved that a unique map exists between a ground-state density and the corresponding external potential for an interacting system, effectively establishing the fundamental theorems of time-independent density-functional theory (DFT).[29] Later, Kohn and Sham, in 1965, showed that, if the density of an interacting system can be calculated in terms of a system of non-interacting one-particle states, there exists an exchange-correlation (XC) potential, $v_{\mathrm{XC}}[\rho_{\mathrm{KS}}(\vec{r})](\vec{r})$, that can reproduce the exact ground-state density of the interacting system.[30]

Analogous to the time-independent case, Runge and Gross, in 1984, showed that, for an interacting system evolving in time and given a particular initial state of the system, there exists a unique map (up to a purely time-dependent function) between the time-dependent external potential and the time-dependent density:

$$\rho(\vec{r},t) \overset{\text{1-1}}{\longleftrightarrow} v_{\mathrm{ext}}[\Psi(\vec{r},0)](\vec{r},t)\{+\mathcal{C}(t)\}, \tag{1.27}$$

where $\mathcal{C}(t)$ is a purely time-dependent function.[34, 51]

Within the Kohn-Sham (KS) formalism of non-interacting particles, this becomes the dependence of the exchange-correlation potential, v_{XC}, on the initial state, both interacting and non-interacting:

$$v_{\mathrm{s}}[\rho(\vec{r},t),\Phi(\vec{r},t=0)](\vec{r},t) = v_{\mathrm{H}}[\rho(\vec{r},t)](\vec{r},t) + v_{\mathrm{XC}}[\rho(\vec{r},t),\Psi(\vec{r},0),\Phi(\vec{r},0)](\vec{r},t). \tag{1.28}$$

Here, $\Psi(\vec{r},0)$ and $\Phi(\vec{r},0)$ are the initial interacting and non-interacting (Kohn-Sham) states of the system under consideration, respectively.

As the density-evolution is unique, it then follows that, if the evolving interacting state is known at any point in time in the past (of the density-evolution) and that state is chosen arbitrarily as the initial one, the evolving XC potential, being a functional of the density, will depend on the corresponding time-dependent density as well. This leads to the realization that v_{XC} depends on the densities at intermediate timesteps in the evolution, as well. Collectively, these dependencies are known as **memory effects**.[38, 52, 53]

In practice, however, the mathematical form of these memory effects isn't easily obtained. Maitra and co-workers (2018) have proposed multiple approximations to the exact expression (obtained by equating the current-density-evolution of the interacting and the non-interacting systems at a given time), but they are computationally resource-intensive. The exact expression itself involves knowledge of the exact evolution of the interacting system, information which is almost never available in practical applications, or good approximations to which might be expensive to evaluate, or even unstable.[50, 54, 55] There have been other, earlier approaches at designing XC potentials that account for the temporal non-adiabaticity and alleviate the errors due to the lack of memory effects. This is the case within TDDFT[56] as well as within time-dependent current-density-functional theory (TDCDFT)[57]. However, these approximations to the temporally non-adiabatic XC potential have problems associated with either the exact conditions associated with time-dependent XC functionals, or restrictions on the kinds of systems they can be used to simulate.[38, 57–61]

As a result, most calculations on molecular systems of finite sizes use the adiabatic approximation, arguments in favor of which include those application problems where the reference state of the system is not altered much (in other words, where the external potential, v_{ext}, is weakly perturbative): post-ionization dynamics, low-intensity scalar field potentials (e.g. when the density evolves in response to a potential turned on only for a finite time), etc.[38, 62–64] On the other hand, it has been shown by Maitra and co-workers that, for model systems, the adiabatic approximation fails dramatically, even with the use of spatially exact (often termed "adiabatically exact") XC functionals.[38, 65] It appears that in some cases where static correlation may play a dominant role the XC potential calculated using the adiabatic approximation fails to capture important features of the exactly evolving XC potentials.[66, 67] In cases of resonant frequency-driven dynamics, it has been observed that TDDFT can introduce some spurious shifts in the resonant energy of the system, an unphysical effect.[68, 69] It is interesting to note that, despite their inability to accurately propagate the electronic density in certain systems, some adiabatic XC potentials can still predict excitation energies of finite systems quite accurately within the linear response regime.[46]

1.3.4 TDHF and Kohn-Sham TDDFT

Time-dependent Hartree-Fock (TDHF) theory has developed independently of Kohn-Sham TDDFT, but can be thought of as a special case of the generalized Kohn-Sham formalism.[70, 71] One can then choose the XC potential used in Eq. (1.26) to be the exchange operator from the HF theory (the last term in Eq. (1.8)). The TDHF method, owing to the nonlinear dependence of the Fock operator on the electronic density, suffers from similar issues related to memory effects as TDDFT methods (see Sec. 1.3.3).[72] TDHF theory does not formally account for memory effects and thus its application is ideally restricted to the regime of dynamics defined by the TDDFT adiabatic theorem. Conversely, many electronic processes may occur outside this regime, particularly those driven by resonant frequencies and high intensity external electric fields. It is therefore important to understand the limitations and applicability of TDHF theory in comparison to TDCIS, a method similar to TDHF in terms of spatial nonlocality but one that has no artifacts due to memory effects.

Note that within the matrix formulation of TDDFT, solving for eigenvalues and eigenvectors of the TDDFT equations within the Tamm-Dancoff approximation (TDA)[73] leads to a set of matrix equations nearly identical to the CIS equations. Both the TDA and CIS tend to overestimate excitation energies compared to their full matrix equivalents of TDDFT (without TDA) and TDHF.[74–77]

Chapter 2

Size-dependent errors

Real-time (RT) electron density propagation with time-dependent density functional theory (TDDFT) or Hartree-Fock (TDHF) is one of the most popular methods to model the charge transfer in molecules and materials. However, both RT-TDHF and RT-TDDFT within the adiabatic approximation are known to produce inaccurate evolution of the electron density away from the ground state in model systems, leading to large errors in charge transfer and erroneous shifting of peaks in absorption spectra. Given the poor performance of these methods with small model systems and the widespread use of the methods with larger molecular and materials systems, here we bridge the gap in our understanding of these methods and examine the size-dependence of errors in real-time density propagation. We analyze the performance of real-time density propagation for systems of increasing size during the application of a continuous resonant field to induce Rabi-like oscillations, during charge-transfer dynamics, and for peak shifting in simulated absorption spectra. We find that the errors in the electron dynamics are indeed size dependent for these phenomena, with the largest system producing the results most aligned with those expected from linear response theory. The results suggest that although RT-TDHF and RT-TDDFT methods may produce severe errors for model systems, the errors in charge transfer and resonantly driven electron dynamics may be much less significant for more realistic, large-scale molecules and materials.

The work[78] introduced in the following sections (reproduced with permission from the authors) has been published as: Ranka, K., Isborn, C.M. “Size-Dependent Errors in Real-Time Electron Density Propagation,” *The Journal of Chemical Physics* 158(17), 174102 (2023). DOI: 10.1063/5.0142515

2.1 Introduction

Simulating electronic dynamics is essential for developing improved understanding of electronic processes in molecules and materials, including charge transfer and the evolution of excited states. Real-time time-dependent density-functional theory (TDDFT) (and time-dependent Hartree-Fock theory, TDHF) methods can be utilized effectively in such cases, as a means of simulating electronic dynamics at relatively affordable computational costs. Real-time TDDFT has been used to study electron (and nuclear) dynamics in a myriad of cases: multinucleon transfer reactions through molecular and atomic collisions[79, 80], molecules in oscillating electromagnetic fields of varying strengths[27, 81–84], high-harmonic generation[85, 86], resonant excitation dynamics (e.g. charge transfer[64, 87–90], excitation-energy transfer[91], strong-field ionization[92], core excitations[93–95], plasmonic excitations[96]), perturbations in organic,[97] bio-molecules[98], chiral molecules[99, 100], metallic[101–103] systems, periodic[104, 105] systems, semiconductor materials[106], optical cavities[107], electronic stopping[108] etc. Runge and Gross[34] proved that there exists a one-to-one mapping between the time-dependent density of a system and the external potential, justifying the use of TDDFT to simulate time-dependent electronic phenomena. This was further shown by van Leeuwen to be a special case of a more fundamental theorem, which states that the time-dependent density of a many-particle system can be reproduced by a unique external potential in another many-particle system with a differing two-particle interaction.[51]

Although formally exact, an extremely common approximation made when using TDDFT in practice is the adiabatic approximation. One of the primary conditions within the formalism of TDDFT is that the evolving density depends on the initial state of the system and the history of its time-evolution. Within the Kohn-

Sham formalism[30] of non-interacting particles, this dependence is incorporated into the exchange-correlation (XC) potential of the time-dependent Kohn-Sham Hamiltonian. Assuming that this potential only depends on the instantaneous density, and not the density at previous points in time or the initial wave function or initial Kohn-Sham state, is the widely employed adiabatic approximation. This dependence on the initial state and the electron density at previous points in time is termed the “memory” of the potential and in practice incorporation of memory is rarely satisfied.[38, 39, 43, 44, 52, 109]

The adiabatic approximation leads to qualitative errors in electron dynamics[38, 39]: incorrect charge transfer dynamics[46], peak shifting in time-resolved absorption spectra[68, 69] due to violation of the resonance condition,[40] and incorrect electron dynamics when driven at resonant frequencies[110]. The errors associated with the adiabatic approximation are often referred to as memory effects; they arise from the use of only the instantaneous density in the exchange-correlation potential. The TDHF method, which can be considered a special case within the generalized Kohn-Sham formalism of TDDFT,[70] suffers from similar issues when used for real-time electron density propagation due to the dependence of the Fock operator on the electronic density, creating a similar set of nonlinear equations.[72, 111]

It has been shown in one-dimensional model systems (such as the asymmetric Hubbard dimer and electron-Hydrogen atom scattering)[40, 46, 67, 69] as well as three-dimensional systems[68, 112, 113] that adiabatic approximations made to the time-dependent TDKS XC produce qualitative errors when used to simulate coherent electron dynamics, especially in cases involving charge transfer. In violation of one of the exact conditions that the TDKS XC potential must follow, some model systems[69] and small molecules[68] show frequency-shifts in peaks in their absorption spectra upon being resonantly driven from stationary states. The degree and direction of this shift is dependent on the amount of population driven from the ground state and the transition frequencies between the higher-lying states.[68] Because larger systems will have a smaller relative change in the total electron density upon excitation of a single electron, the reference electron density input into the potential will be closer to that of the ground state compared to small model systems. It is unclear how such large systems would behave when driven resonantly starting in stationary states, one of the common applications for real-time TDDFT methods. Given the popularity of TDDFT methods for large-scale chemical applications, understanding and mitigating any associated systemic size-dependence (including errors due to memory effects) is an important undertaking.

In this study we aim to analyze the system size dependence of errors due to the adiabatic approximation. We restrict our analysis to electron dynamics generated with real-time TDHF and time-dependent configuration interaction singles (TDCIS) methods. For both methods, the time-independent, ground-state wave functions are exactly the same – the Hartree-Fock wave function. However, the TDCIS method is a wave function based method that does not suffer from errors due to the dependence of the potential on the density that are found with TDHF and TDDFT within the adiabatic approximation. By comparing TDHF and TDCIS, any consideration of electron correlation effects is removed from our analysis. For three molecules ($(CH_3)_2N$-$(CH{=}CH)_nH$, n=1,2,3) with increasing π-conjugation, we show that size-dependent effects do indeed exist due to the dependence of the potential on the time-dependent density, specifically in the behavior with a resonant field and in the shifting of peaks in the absorption spectrum. We examine the size-dependence of this qualitatively unphysical behavior to determine if TDHF and TDDFT methods could be more confidently applied to larger chemical systems.

2.2 Computational Details

The set of molecules chosen for the study are π-conjugated systems that increase systematically in size, with 40, 54, and 68 electrons. The systems are characterized by a dimethyl amide donor moiety, $(CH_3)_2N$, attached to a series of unsaturated, π-conjugated hydrocarbon chains increasing in length, $(CH = CH)_nH$ (n=1, 2, 3), acting as the electron-accepting moieties (Fig. 2.1). The amide group acts as an electron donor, overall increasing the excited state charge transfer character compared to simple π-conjugated hydrocarbons and leading to a larger change in the dipole moment between the ground state and excited state.

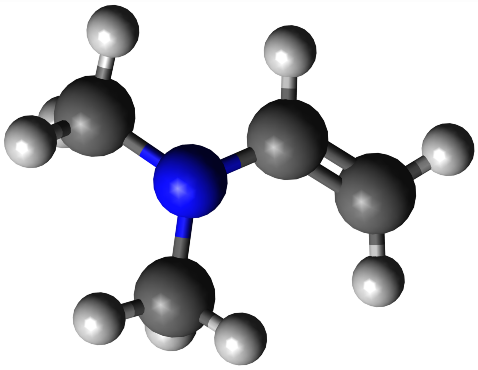

System 1, $(CH_3)_2N(CH{=}CH)H$

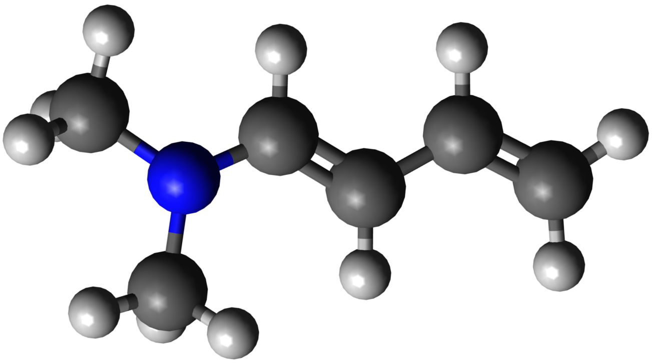

System 2, $(CH_3)_2N(CH{=}CH)_2H$

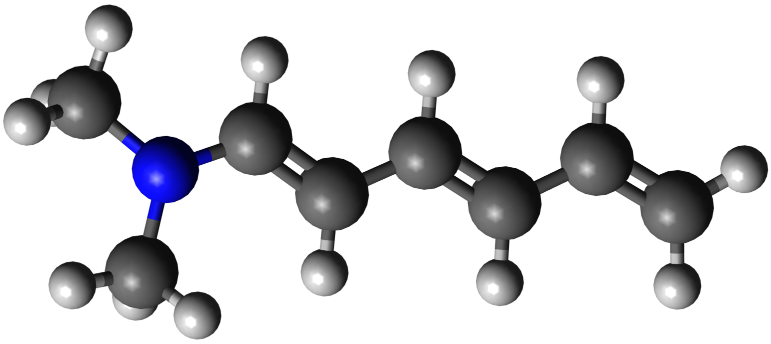

System 3, $(CH_3)_2N(CH{=}CH)_3H$

Figure 2.1: Set of π-conjugated molecules with increasing size.

Molecular geometries were optimized at the B3LYP/6-31+G* level of theory.[114–116] Characterization of the excited states was performed with linear response TDHF/STO-3G and CIS/STO-3G calculations using the GAUSSIAN quantum chemistry program (Development Version i14+)[117]. The STO-3G basis set is chosen for the sake of ease of analysis of the composition of the excited states and electron dynamics, with some results shown for the larger 6-31G basis set in the SI. The main conclusions of this study are not affected by the choice of basis set. We additionally show the results of using an unrestricted wave function for propagation, which we find are identical to the closed-shell results presented here.

To obtain an estimate of the energy of the doubly excited state, the S_0, S_1 and S_2 states were computed using the state-averaged complete active space self-consistent field (SA-CASSCF) method[118], with active spaces of (4,3), (6,5) and (8,7) for Systems 1, 2 and 3, respectively. The active spaces were chosen to include the frontier n- and π-type orbitals involved in the $S_0 \rightarrow S_1$ and $S_1 \rightarrow S_2$ transitions. The state-averaging was carried out by assigning equal weights to the S_0, S_1 and S_2 states. Energies are discussed in the text and given in the SI.

The external perturbation chosen is the light-matter interaction described by a sinusoidal electric field, coupled with the electrons under the dipole approximation as[35, 36]

$$\hat{V}_{\mathrm{ext}}(\mathbf{r}, t) = \mathbf{E}\cdot\mathbf{r} = \mathbf{E}_{\max}\sin(\omega t)\cdot\mathbf{r}, \tag{2.1}$$

where $\mathbf{E}_{\max} = E_{\max,x}\hat{\mathbf{i}} + E_{\max,y}\hat{\mathbf{j}} + E_{\max,z}\hat{\mathbf{k}}$ is the amplitude vector and ω is the frequency of the oscillatory electric field. The molecular axes align best with the x-axis and the $S_0 \rightarrow S_1$ transition possesses a large transition dipole moment along this axis; hence the field is chosen to be linearly polarized along the x-axis. The dipole moment matrices in the STO-3G basis, $(\upmu_x, \upmu_y, \upmu_z)$ corresponding to the dipole moment operators $(\hat{x}, \hat{y}, \hat{z})$, are obtained from the GAUSSIAN program. The time-dependent dipole moment along each axis is

$$\mu_{\zeta\in\{x,y,z\}}(t) = \mathrm{Tr}(\mathbf{P}^{\chi}(t)\upmu_{\zeta}^{\chi}) \tag{2.2}$$

where χ is the basis set used for the linear expansion of the MOs. The contribution of $\hat{V}_{\text{ext}}$ to the Hamiltonian matrix is

$$\mathbf{V}^{\chi}_{\text{ext}}(t) = E_{\max,x} \sin(\omega t) \boldsymbol{\mu}^{\chi}_{x}. \tag{2.3}$$

We use a propagation step size of 0.002 fs (~0.08268 a.u.). Trajectories with an applied sinusoidal external field have been generated by perturbing the molecules from their ground states. Trajectories with a delta-kick perturbation are generated by applying a constant electric field to the ground state self-consistent field calculation before beginning electron propagation. The TDHF trajectories have been generated using the GAUSSIAN program and the TDCIS trajectories have been generated using an in-house Python code that uses the GAUSSIAN generated CIS energies and transition dipoles as input parameters.

The time-dependent MO occupations, $N_i(t)$, plotted for RT-TDHF and TDCIS are obtained by projecting the time-dependent MOs and wave functions onto the initial set of Hartree-Fock MOs and the Hartree-Fock wave function,

$$N_i^{\text{RT-TDHF}}(t) = \mathbf{C}_i^{\dagger}(t)\mathbf{P}(t)\mathbf{C}_i(t); \tag{2.4}$$

$$N_i^{\text{TDCIS}}(t) = |\mathbf{a}_i(t)|^2 \times N_i^{\text{CIS}}(0). \tag{2.5}$$

Here $\mathbf{C}_i(t)$ is the time-dependent MO coefficient vector for orbital i, and $N_i^{\text{CIS}}(0)$ is the occupation number of the ith orbital calculated as a sum of its occupations over all the determinants used for a given static CIS calculation.

Linear absorption spectra are generated using the time-dependent electron density-matrices and Eq. (2.2). The total time-dependent electronic dipole moment, $\mu(t) = \sqrt{\mu_x^2(t) + \mu_y^2(t) + \mu_z^2(t)}$, is used to calculate the dipole moment time-correlation function, which is Fourier-transformed to obtain the absorption cross-section at 0 K in the frequency domain as [119]

$$\alpha(\omega) = \frac{2\pi\omega}{3} \int_{-\infty}^{\infty} dt \langle \mu(0)\mu(t) \rangle e^{-i\omega t}. \tag{2.6}$$

2.3 Results and Discussion

2.3.1 Stationary State Characterization

To determine stationary excited states of the molecules, CIS and LR-TDHF calculations were performed. The resulting excitation energies, and x-axis components of excited state and transition dipole moments are listed in Table 2.1 for state S_1 (total dipole moments are given in the SI). Given the same ground state, the S_0 dipole moments for the three molecules are the same across the two methods. The large difference in ground S_0 and excited S_1 state dipole moments (consistently > 1 debye across the set of molecules) indicates that S_1 is a charge-transfer state. The magnitude of the dipole moment of S_1 increases as the system size increases. This increase is, however, larger for excited state dipole moments calculated using CIS compared to TDHF. The difference in discrepancy between excited state dipole moments decreases as the system size increases. The charge-transfer excitation energies calculated using the linear response methods decrease in value with increasing system size with the corresponding $S_0 \rightarrow S_1$ density-difference plots show an increase in electron density in the π-cloud and a decrease around the N-center in the molecules (Fig. A.1).

Table 2.1: Transition energies, and x-axis components of state and transition dipole moments calculated using linear response TDHF and CIS methods for Systems 1, 2 and 3.

LR-TDHF	ΔE (eV)	μ_x (D)		
	$S_0 \rightarrow S_1$	S_0	S_1	$S_0 \rightarrow S_1$
System 1	8.95	-1.12	-2.84	-4.13
System 2	7.05	-1.94	-4.29	-6.60
System 3	5.99	-2.58	-5.47	-8.65
CIS	ΔE (eV)	μ_x (D)		
	$S_0 \rightarrow S_1$	S_0	S_1	$S_0 \rightarrow S_1$
System 1	9.47	-1.12	-3.82	-4.52
System 2	7.51	-1.94	-5.09	-7.04
System 3	6.38	-2.58	-6.13	-9.33

Table A.3 lists the composition of the $S_0 \rightarrow S_1$ transition for the three molecules calculated in terms of one-electron transitions between orbitals. For System 1, the transition is primarily characterized by a HOMO → LUMO transition, with small contributions from other one-electron transitions. With increasing system size the one-electron transitions involving the frontier orbitals beyond the HOMO and LUMO contribute to slightly higher extents, but the electronic character of the transition across the three molecules is primarily of a one-electron HOMO → LUMO transition for both excited state methods. Corresponding density-difference plots show similar nature of re-distribution of the electron density upon excitation from the ground state S_0 to S_1.

Previous studies by one of the authors showed that higher lying excited states that are not accessible by linear response TDHF can contribute to the electron density evolved using the RT-TDHF method, and that the resonance energy is affected by the superposition of the ground and excited states: the linear response of a superposition state composed of S_0 and S_2 states has been shown to yield a resonant frequency that is an average of $S_0 \rightarrow S_1$ and $S_2 \rightarrow S_1$ transitions when using the real-time TDHF method in H_2 and HeH^+ systems. Thus, the S_2 state is implicitly accounted for in real-time TDHF and the gap between S_1 and S_2 states can determine both the direction and the degree of the peak-shifts.[68, 72] To determine the direction of the peak shifts, the excitation energies of $S_0 \rightarrow S_1$ and $S_1 \rightarrow S_2$ transitions were calculated using the SA-CASSCF method, where the S_2 state corresponds to a doubly excited state with nearly double occupation of the LUMO. The resulting $S_0 \rightarrow S_1$ excitation energies show a similar trend as with CIS and LR-TDHF: decreasing excitation energies with increasing system size ($\Delta E_{\mathrm{S}_0 \rightarrow \mathrm{S}_1} = 9.24, 7.23, 5.92$ eV). The energies for the next transition are smaller: $\Delta E_{\mathrm{S}_1 \rightarrow \mathrm{S}_2} = 3.97, 1.18, 1.29$ eV, respectively. Given the energetically lower-lying $S_1 \rightarrow S_2$ transition compared to the $S_0 \rightarrow S_1$ transition, the resonance peaks are expected to shift towards lower energies as the population of the LUMO increases and the contribution of the doubly excited configuration increases.

2.3.2 Electron Dynamics

Moving to the time-domain, we can use both RT-TDHF and TDCIS methods to propagate the electrons in the presence of an applied field. For RT-TDHF, the linear absorption spectra of the three systems perturbed with a δ-pulse shows peaks at expected positions, corresponding to energies calculated with the linear response methods. To force the evolving TDHF electronic structure away from the regime where the adiabatic approximation holds, the molecules are significantly perturbed from their initial ground states using applied fields with the field-frequencies resonant with the linear response $S_0 \rightarrow S_1$ transitions. We first excite the systems using a continuous field with frequency resonant with the $S_0 \rightarrow S_1$ transition for each molecule to induce Rabi-like oscillations, and then later examine population and peak shifting trends with finite-time applied fields.

2.3.2.1 Continuous resonant field : Rabi oscillation

The external field with resonant frequency can be used to drive the system significantly away from its reference state (the Hartree-Fock state in the current study). With the application of a resonant field to a two-level system, the population of the S_0 and S_1 states should undergo Rabi oscillation, inverting at a frequency directly proportional to the field amplitude and the transition dipole moment between the two states, calculated as $\Omega_{\text{calc.}} = |\mu_{x,S_0 \to S_1}| \times E_{\text{max},x}$. Previous studies on two-level systems have shown that Rabi cycle-like oscillatory behavior of the electron density propagated using RT-TDHF can deviate significantly from the exact electron dynamics.[111, 120] The difference in electron dynamics is attributed to detuning of the resonant frequency due to the dependence of the XC potential on the instantaneous electron density.[120] This effect can be significant depending on the fraction of electron density rearranged with respect to the total electron density.[38] Understanding the potential errors of a given methodology in modeling a system in the presence of a resonant field is important for simulating many varieties of pump-probe and nonlinear spectroscopy.

To examine the differences between the electron dynamics calculated using TD-CIS and RT-TDHF methods for the three systems of interest in the presence of a resonant field, we apply a sinusoidal driving field for the entire duration of propagation with a field-frequency equal to the $S_0 \to S_1$ transition energy at maximum field strengths of 0.001, 0.003, and 0.005 a.u. The molecules are not formally two-level systems, so some deviation from ideal Rabi oscillation behavior is expected. As the populations of electronic states cannot be directly quantified with TDHF, we use the occupation of the virtual orbital space as a quantifier of the deviation of TDHF electron dynamics from ideal behavior. Because the $S_0 \to S_1$ transition is primarily HOMO → LUMO in character, we monitor the occupation of the LUMO as a metric for population of the S_1 state. See Fig. 2.2 for population oscillation with an applied field of $E_{\text{max}} = 0.003$ a.u. Plots with $E_{\text{max}} = 0.001$ and 0.005 a.u. are shown in Figs. A.5.

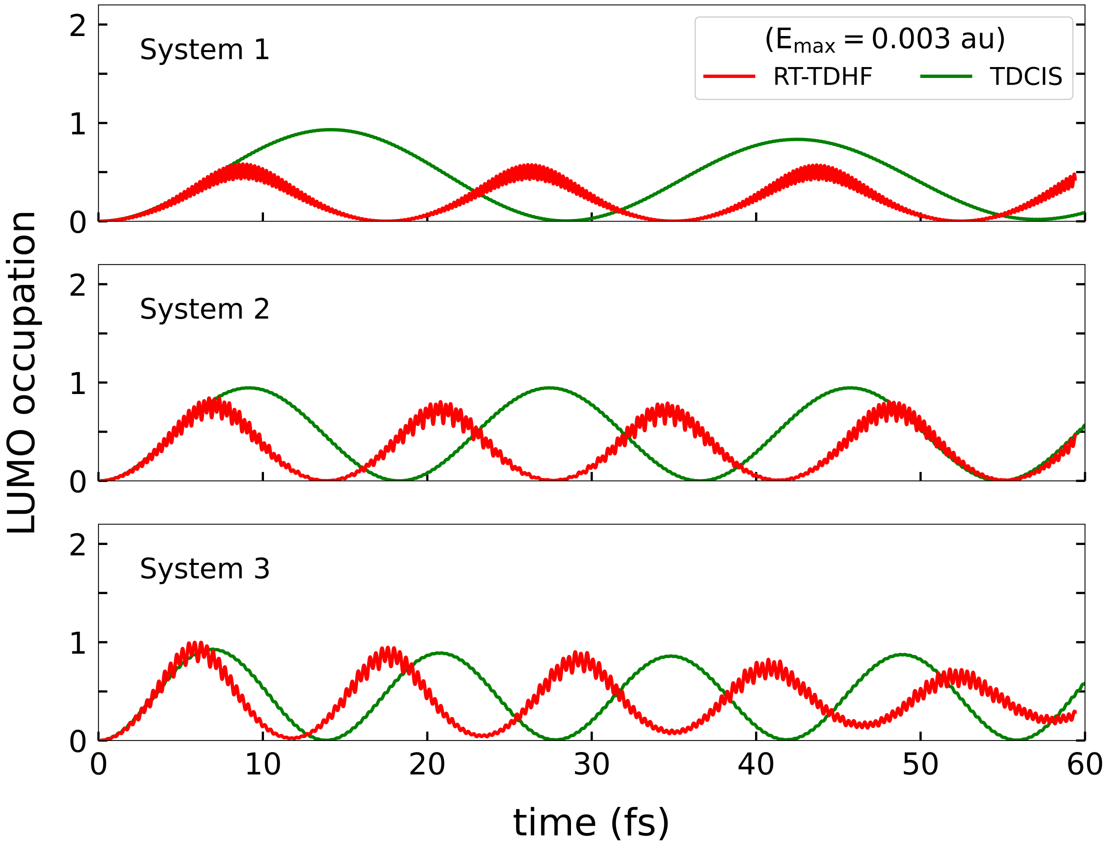

Figure 2.2: Time-dependent LUMO occupations for Systems 1-3 with the field turned on, with applied field frequencies resonant with the $S_0 \rightarrow S_1$ linear response transition energies and field-amplitude of 0.003 a.u. The degree of electron density transferred to the LUMO changes with system size.

The TDCIS behavior is as expected, with population oscillating between the S_0 and S_1 states as seen by near single occupation of the LUMO for each system; the maximum population of the LUMO is 0.95, 0.95 and 0.94 e for Systems 1, 2, and 3, respectively. The maximum value remains consistent throughout the duration of the applied field, over many Rabi cycles. Additionally, the frequency of the population oscillation is well within the numerical error ($O(10^{-5}$ a.u.)) of the expected Rabi frequency for all three systems.

In contrast, deviation from Rabi oscillation behavior is observed for TDHF propagation. The maximum LUMO population is 0.31, 0.58, and 0.76 for System 1, for fields with strengths of 0.001, 0.003, and 0.005 a.u. applied for 100, 60, and 20 fs, respectively. Systems 2 and 3 have closer to full population of the LUMO, with maximum occupation values of 0.84 and 0.99 for field-strength of 0.003 a.u. However, all systems also show an additional high frequency oscillation of the population when the LUMO is maximally occupied, indicative of a mixed state rather than being purely in the S_1 state[72, 110], and System 3 also no longer undergoes full population inversion after three Rabi cycles, which is presumably due to occupation of higher lying states as we see increased occupation of the virtual space, see discussion below.

Table 2.2: Rabi frequencies (in $\times 10^{-3}$ a.u.) for field resonant with the $S_0 \rightarrow S_1$ transition, calculated using linear response values for the transition dipole moment ($\Omega_{\text{calc.}}$) and observed from the real-time electron dynamics ($\Omega_{\text{obs.}}$) for Systems 1, 2 and 3, for field-amplitudes of $E_{\text{max}} = 0.001$, 0.003, and 0.005 a.u.

TDHF	0.001 a.u.		0.003 a.u.		0.005 a.u.	
	$\Omega_{\text{calc.}}$	$\Omega_{\text{obs.}}$	$\Omega_{\text{calc.}}$	$\Omega_{\text{obs.}}$	$\Omega_{\text{calc.}}$	$\Omega_{\text{obs.}}$
System 1	1.6	4.6	4.9	9.9	8.1	14.2
System 2	2.6	5.9	7.8	12.4	13.0	17.6
System 3	3.4	6.8	10.2	14.5	17.0	21.1

Another obvious discrepancy in the TDHF electron dynamics from the ideal Rabi behavior is in the frequency of oscillation and here we find a strong size-dependent trend. We can quantify the trend by computing the Rabi frequencies using linear response transition dipole moments (Table 2.1), and comparing this calculated Rabi oscillation frequency to those deduced from the oscillations of time-dependent LUMO occupations for applied electric fields with differing amplitudes, where we extract the Rabi oscillation time by taking the time for LUMO occupation to reach a minimum within the electron dynamics. Comparison of the LR calculated and RT observed Rabi oscillation frequencies are reported in Table 2.2. For System 1 in the presence of the weakest field applied here, E_{max}=0.001 a.u., the observed population oscillation has a frequency of 4.6×10^{-3}, whereas that calculated is 1.6×10^{-3}, yielding a deviation of ∼180%. The deviation decreases to

$\sim$75% with the stronger field of E_{max}=0.005 a.u. The agreement in the oscillation frequency is improved with increasing system size, going to deviations of $\sim$125% and $\sim$100% for Systems 2 and 3 with E_{max}=0.001 a.u. and $\sim$35% and $\sim$25% for Systems 2 and 3 with E_{max}=0.005 a.u. Overall, the trend suggests that the errors in transfer of electron density between S_0 and S_1 in the presence of a resonant field tend to decrease with increasing system size, implying potentially a similar increase in accuracy in charge-transfer dynamics.

For a two-level system, increasing the intensity of the applied resonant field increases the frequency of population oscillation. With the three systems propagated with the TDCIS method, we indeed see the population driven at a faster rate between S_0 and S_1, with little population of other states. To directly compare TDCIS and TDHF maximum populations, we next scan the time for which the external resonant sinusoidal field is turned on as well as scan the field strength. The range of field-strengths is between 0.005 and 0.075 a.u., and the number of field-cycles is between 1 and 10. In Fig. 2.3 the map of maximum virtual MO occupations during the resonant field application is shown for a range of field strengths and number of field cycles. The TDCIS method produces nearly uniform maximum occupation of one electron as long as the field is on long enough and is intense enough.

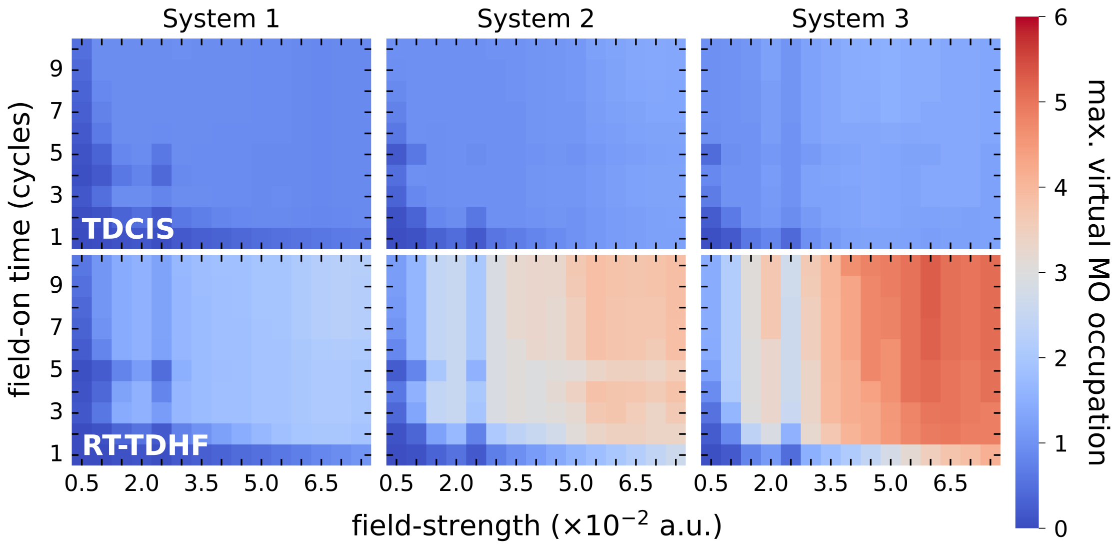

Figure 2.3: Maximum virtual MO occupations (sum of LUMO, LUMO+1 and LUMO+2) within the duration of the applied field obtained from TDCIS (top) and RT-TDHF (bottom) propagation methods, plotted as a function of field-on time and field amplitude for Systems 1-3 perturbed with a sinusoidal electric field using CIS and linear response TDHF $S_0 \rightarrow S_1$ transition-resonant frequencies.

However, this behavior does not hold for the TDHF electron density propagation, where we instead see much different maximum virtual populations and much higher populations of the virtual orbital space. For all three systems, we see that a more intense field leads to higher occupation of the virtual space, well beyond the single electron occupation of the LUMO. With the field parameters explored, System 1 approaches nearly double occupation of the LUMO, System 2 has three electrons in the virtual MOs, and System 3 has five to six electrons in the virtual space for the more intense fields. The greater population of System 3 could be expected, given that there are many more excited states that could be occupied for a larger system. Overall, this population map suggests that for TDHF electron propagation, applying a field resonant with the $S_0 \rightarrow S_1$ transition populates states much higher lying than the S_1 state, and that the resonant field does not lead to well-behaved population oscillation between S_0 and S_1.

2.3.2.2 Single electron occupation of LUMO: Charge transfer

In this and the next section we analyze the behavior of TDHF electron dynamics when the electron occupation is close to that expected for the S_1 state. In order to drive the system away from the initial S_0 reference state the molecules considered were again perturbed with fields using the linear response resonant frequencies. Field-strengths and durations were chosen by picking trajectories from the set used to plot Fig. 2.3 that, when the field was removed, had average HOMO and LUMO occupations close to one for a "clean" $S_0 \rightarrow S_1$ transition (HOMO→LUMO transition being the major contributor to the S_1 state, cf. Table A.3). Then the field-parameters corresponding to the most stationary evolution (constant MO occupation(s) with time) were chosen to induce the transition. In Fig. 2.4 we show the TDHF MO occupations with the chosen field parameters. For the three molecules, the final occupation is close to one electron in the HOMO and one electron in the LUMO, as expected for the S_1 state (see Fig. A.7 for the corresponding TDCIS MO occupation and S_1 state population plot).

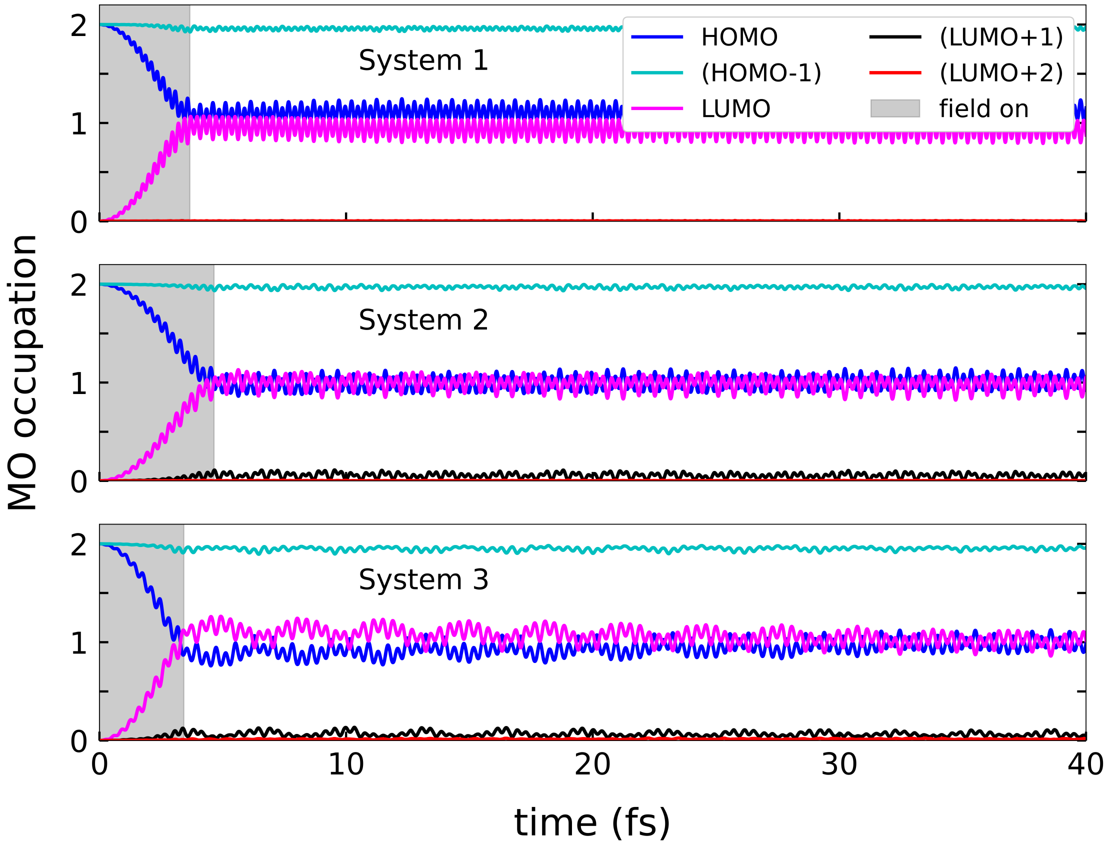

Figure 2.4: Time-dependent occupations obtained by projecting evolving molecular orbitals (MOs) onto the initial set of MOs, plotted for different perturbations with systems initialized in S_0. The amplitudes of the perturbing fields are 0.01, 0.005, 0.005 a.u. and the fields are turned on for 8, 8, 5 cycles (gray area in the plot) for Systems 1, 2 and 3, respectively.

We next analyze the degree of charge transfer during this population change by monitoring the time-dependent dipole moment for each molecule. Based on the stationary state characterization in Table 2.1, we expect the dipole moment to increase as the population is driven from S_0 to S_1, with the change in dipole moment increasing with increasing system size. This is indeed what we see with both TDCIS and TDHF methods, as shown in Fig. 2.5. For all systems, the initial dipole moment is identical for both methods as both TDCIS and RT-TDHF have the same initial HF ground state. The stationary state S_1 dipoles are shown with dashed lines, and we see that the TDCIS time-dependent dipole moment approaches this value and remains centered around the S_1 dipole moment. There is very little oscillation for System 1 and System 2, and a small amount of oscillation for System 3.

Using the dipole moments along the x-axis, we see that the RT-TDHF time-dependent dipole moment for System 1 approaches the LR-TDHF dipole moment of -2.84 D, but does not complete the full charge transfer. We can quantify the extent of charge transferred as $(\mu^{\mathrm{RT}}_{x,\mathrm{avg}} - \mu^{\mathrm{HF}}_{x,\mathrm{S}_0})/(\mu^{\mathrm{LR}}_{x,\mathrm{S}_1} - \mu^{\mathrm{HF}}_{x,\mathrm{S}_0})$, where $\mu^{\mathrm{HF}}_{x,\mathrm{S}_0}$ is the HF ground state dipole moment, $\mu^{\mathrm{LR}}_{x,\mathrm{S}_1}$ is the LR-TDHF S_1 state dipole moment and $\mu^{\mathrm{RT}}_{x,\mathrm{avg}}$ is the average RT-TDHF dipole moment (see Fig. A.6). We find that System 1 completes ∼48% of the charge transfer when starting at -1.12 D and ending at an average value of ∼-1.97 D. The RT-TDHF dipole moment for System 2 also approaches the LR-TDHF S_1 dipole moment, but again falls short, obtaining an average value of ∼-3.44 D and completing only ∼64% of the expected charge transfer. Additionally, System 2 shows significant dipole oscillations that are larger in magnitude than the total change in dipole moment from the ground state. Similarly, System 3 does not quite get to the LR-TDHF S_1 dipole moment, but the average dipole moment of ∼-4.57 D yields ∼69% of the charge transfer, so completes the most of all three molecules. Similar to System 2, the dipole oscillations of System 3 are very large. These large dipole oscillations suggest a mixed state for RT-TDHF, whereas nearly identical MO occupations with TDCIS produce very little dipole oscillations, suggesting a near-stationary state.

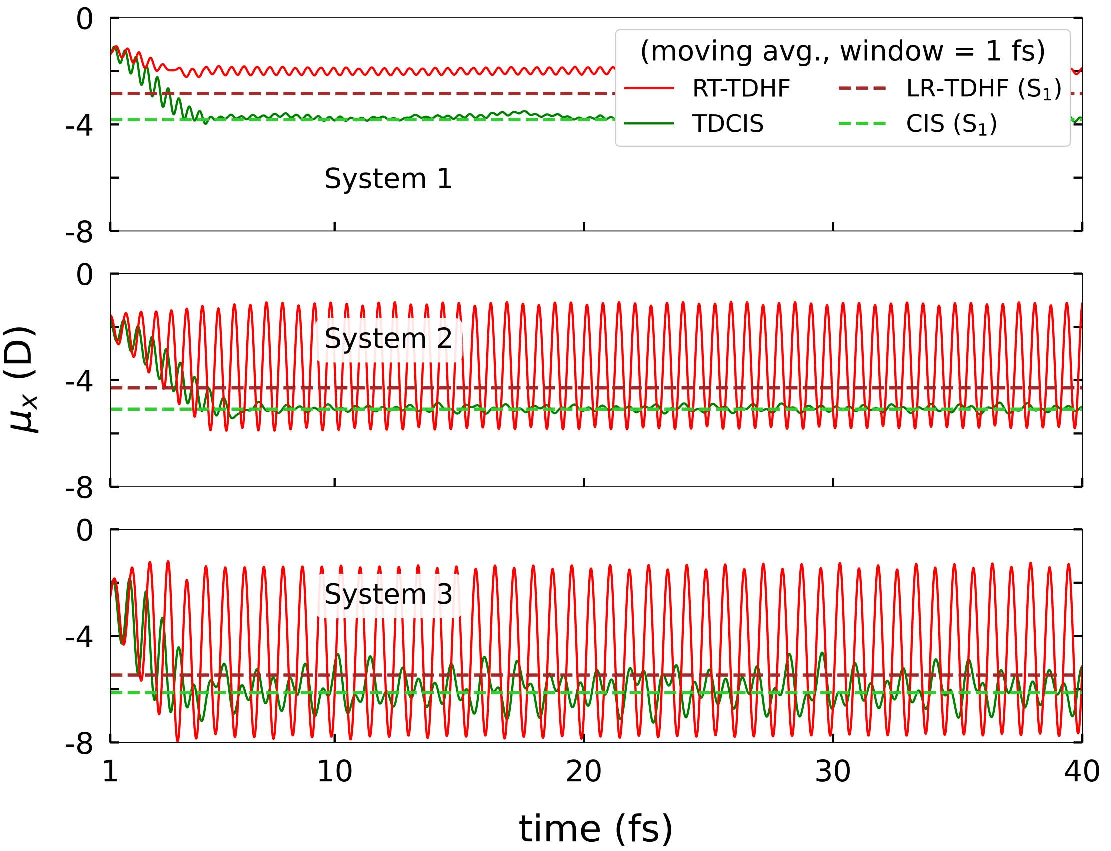

Figure 2.5: Moving-averaged time-dependent dipole moments (along the x-axis) of the three molecules, obtained from the resonant-frequency field perturbed RT-TDHF and TDCIS trajectories. The systems are initialized in the state S_0. The dipole moments plotted are averaged over a window of 1 fs, or 500 timesteps, as a moving average.

Overall, driving the RT-TDHF MO occupation to what would be expected for the S_1 state produces an electron density indicative of some charge transfer, but not as much as would be expected from the LR-TDHF S_1 dipole moments. In all cases, the RT-TDHF average dipole moment is smaller than the corresponding LR-TDHF value, showing that the charge transfer is incomplete. There is a size-dependent trend in the degree of charge transfer, with System 1 showing the largest disagreement in the dipole moment charge compared to linear response theory, with some improvement with increasing system size. However, the improvement in the average dipole moment change for Systems 2 and 3 comes with a large dipole oscillation, supporting that the systems are in a mixed state. A mixed state at equal population of the HOMO and LUMO agrees with the finding in some previous work by one of the authors that suggests that single electron occupation of the HOMO and LUMO with single determinant RT-TDHF may be more representative of a mixed state composed half of the S_0 state and half of the doubly excited S_2 state, rather than the S_1 state.

2.3.2.3 Single electron occupation of LUMO: Peak shifting in absorption spectra

Peak shifting in absorption spectra when simulating time-dependent electron dynamics is a violation of the resonance condition. We physically expect that peaks in the spectrum will have changes in intensity as the population evolves, but that the energy of the peaks will remain constant rather than shifting in energy. The unphysical peak shifting phenomenon has been observed when using real-time TDDFT methods with the adiabatic approximation as the density is perturbed far from the reference ground state.[38, 39, 68, 69] To determine if there are size-dependent trends in peak shifting, the chosen molecules are driven from their initial ground states using frequencies resonant with $S_0 \rightarrow S_1$ transition energies calculated from LR-TDHF as described in the previous section, resulting in single occupation of the HOMO and LUMO. The system is then propagated with the field off for 40 fs, and the resulting field-off dipole moment is Fourier-transformed to produce the absorption spectrum for each system.

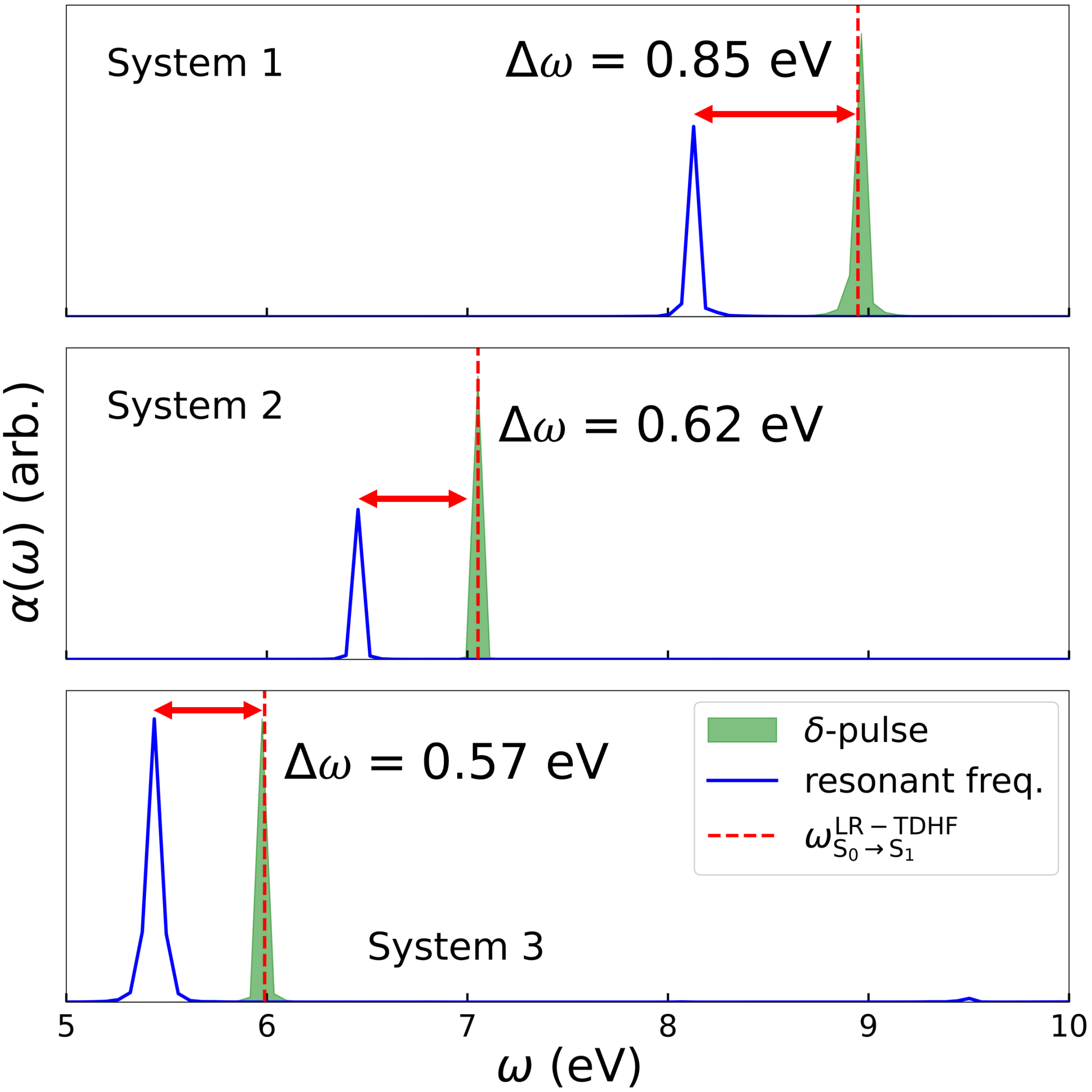

Figure 2.6: Peak shifts observed in the linear absorption spectra, calculated from time-dependent dipole moments obtained using RT-TDHF propagation, obtained from the resonant-frequency-perturbed systems in comparison to those obtained from the weak delta-pulse-perturbed systems. The frequency used for perturbing the molecules is resonant with the LR-TDHF $S_0 \rightarrow S_1$ transition.

The resulting spectra are shown in Fig. 2.6, with comparison given to the spectra computed from a trajectory with the electron density perturbed with a delta-kick electric field. The LR-TDHF $S_0 \rightarrow S_1$ excitation energies are also shown in the spectra for reference, with the LR-TDHF energies being in excellent agreement with the delta-kick absorption spectra peaks. For all three molecules, the spectra generated from the single electron occupation show significant shifts from that obtained with the delta-kick pulse, in violation of the resonance condition. The peak shifts to lower energies by 0.85 eV, 0.62 eV, and 0.57 eV for Systems 1, 2, and 3, respectively, showing a decreasing shift with larger system size. If the amount of the peak shift is determined as a percentage of the linear response excitation energy, then both System 1 and 3 show a shift of 9.5% and System 2 a shift of 8.8%, suggesting no size-dependent trend when examining percentage (See Table S5 in the SI).

In previous studies of TDDFT peak shifting in small model molecular systems, the direction and magnitude of the peak shift was found to be directly related to the $S_1 \rightarrow S_2$ transition energy, where the $S_0 \rightarrow S_2$ transition was dark and the S_2 state was predominantly a doubly occupied LUMO. As the LUMO became populated, the total electron density became a mixture of the S_0 and the S_2 states, with the peak frequency corresponding to the relative mixture of the $S_0 \rightarrow S_1$ transition and the $S_2 \rightarrow S_1$ transition. Thus, the $S_1 \rightarrow S_2$ peak became coupled to the $S_0 \rightarrow S_1$ peak as the LUMO occupation grew. With the relatively larger systems considered here it is difficult to characterize a similar S_2 state, but with an estimate of the energies given by the SA-CASSCF method, we know that the energy of the $S_1 \rightarrow S_2$ transition is likely smaller than the energy of the $S_0 \rightarrow S_1$ transition, causing a shift to lower energies. Additionally, just based on the relative energies of the SA-CASSCF $S_0 \rightarrow S_1$ and $S_1 \rightarrow S_2$ transitions, we would also expect a decrease in the degree of peak shifting with increasing system size. Overall, we find that the magnitude of the peak shift is significant, but it does indeed decrease as the system size increases, which may be due to the relative energies in the chosen molecules or due to larger systems being less subject to errors due to the adiabatic approximation.

2.3.2.4 Basis set size

We also simulated the electron dynamics of the three Systems using the larger 6-31G basis set. The dynamics are generated by keeping the same field-amplitudes from the STO-3G calculations, the resonant $S_0 \rightarrow S_1$ frequencies are obtained from the corresponding linear response TDHF calculations (7.2, 5.8, 4.9 eV for Systems 1, 2, 3, respectively). The field-times are adjusted to be turned off at the point where both HOMO and LUMO populations first reach a value close to 1 (see Fig. 2.7). As can be seen by the MO populations at this point, multiple MOs become occupied, leading to additional complexity in analyzing the composition of the excited state S_1 compared to the STO-3G basis. There is also significantly more MO occupation oscillation, showing that a stationary S_1 state for the three Systems could not be obtained based on tuning just the HOMO and LUMO occupations. The peak-shifting is still observed to loosely follow a similar size-dependent trend of decreasing peak-shifts with increasing system-size (see Fig. 2.8), but it is difficult to directly compare the degree of shift because the MO occupations vary more for each system.

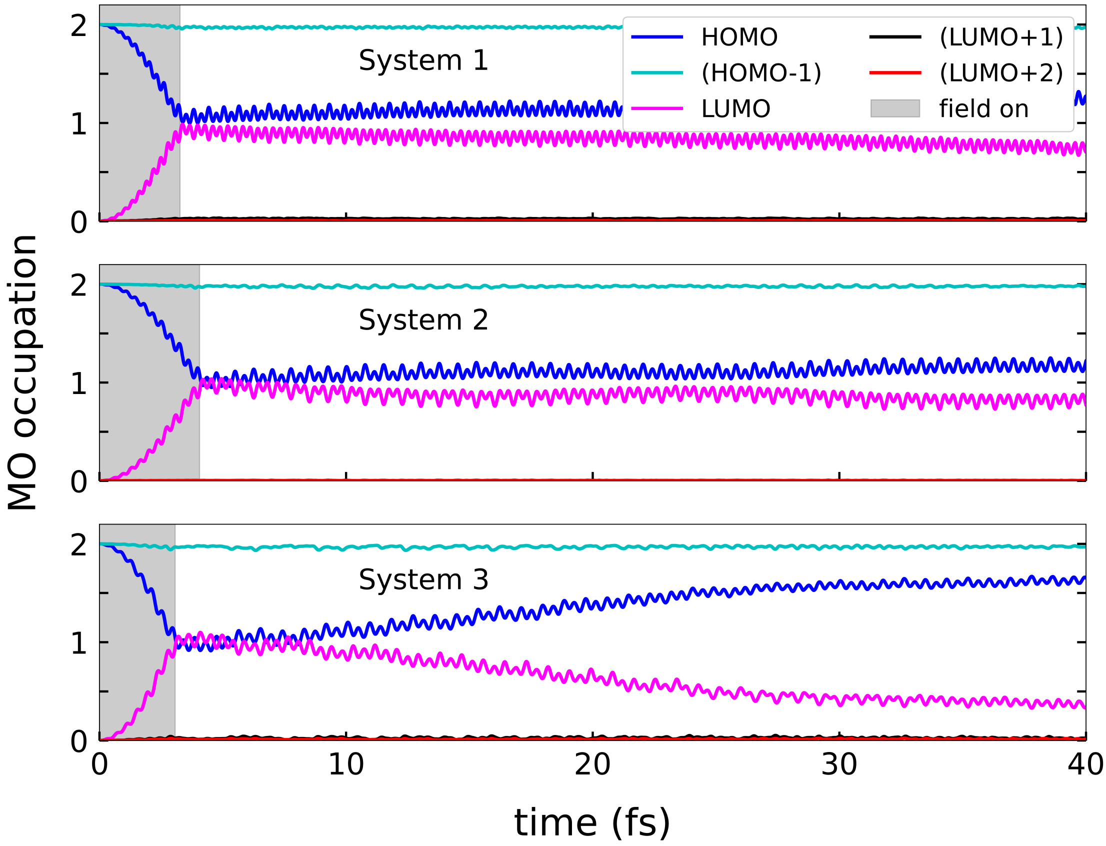

Figure 2.7: TDHF/6-31G time-dependent occupations obtained by projecting evolving molecular orbitals (MOs) onto the initial set of MOs, plotted for different perturbations with systems initialized in S_0. The amplitudes of the perturbing fields are 0.01, 0.005, 0.005 a.u. and the fields are turned on for 3.3, 4.1, 3.1 fs (gray area in the plot) for Systems 1, 2 and 3, respectively.

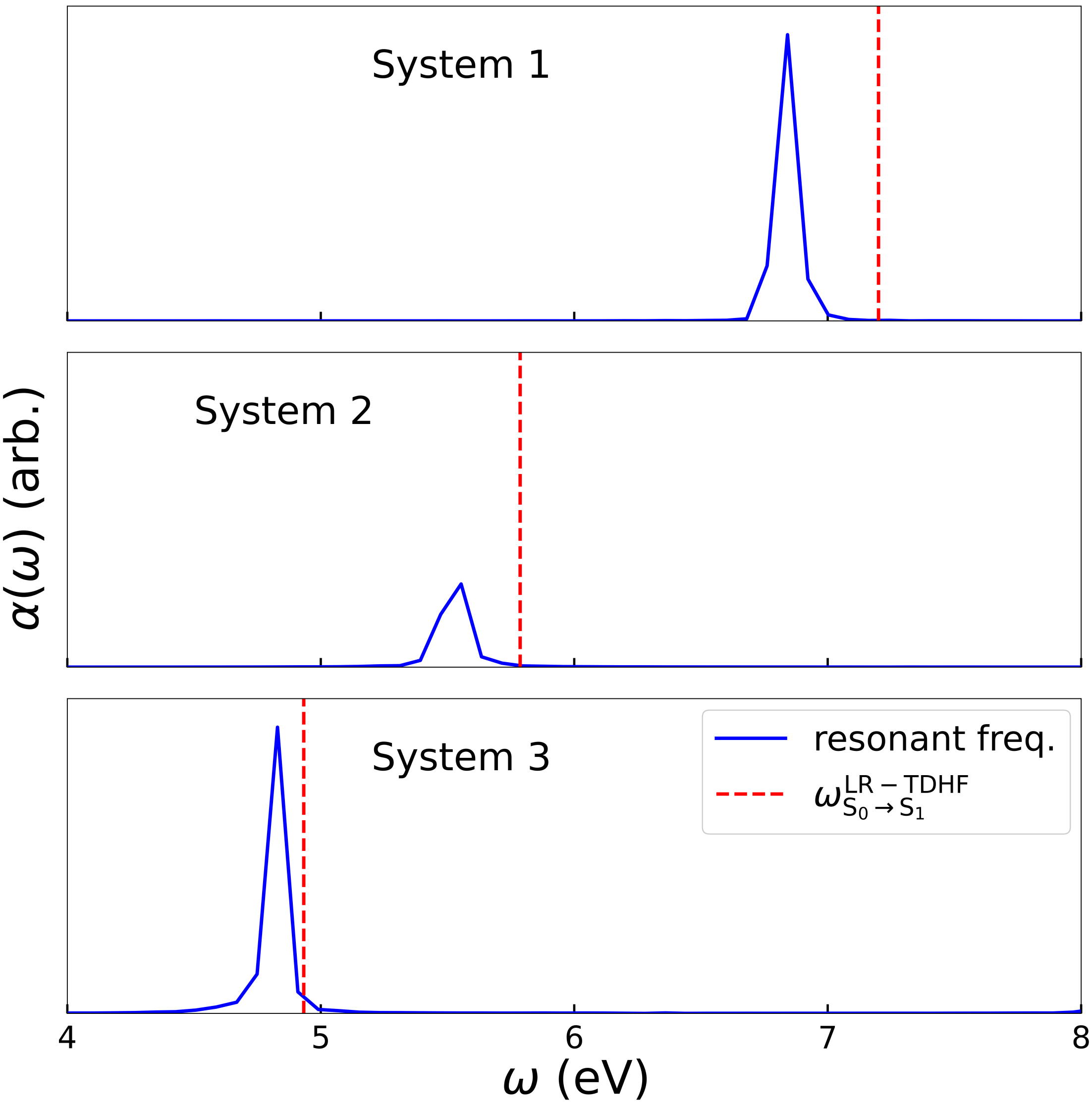

Figure 2.8: Peak shifts observed in the linear absorption spectra, calculated from time-dependent dipole moments obtained using RT-TDHF propagation, obtained from the linear response $S_0 \to S_1$ transition resonant-frequency-perturbed Systems using the 6-31G basis set.

2.3.2.5 Reference wave function

The molecules considered in this study display a strong closed shell character as seen by the same linear response excitation energy values for the unrestricted LR-TDHF calculations. The spectrum as the system is driven from the ground state also matches with the closed-shell results, with the peak-shifts observed in spectra obtained from the unrestricted RT-TDHF electron dynamics are of nearly the same magnitude (within numerical errors) as the restricted case (see Fig. 2.9).

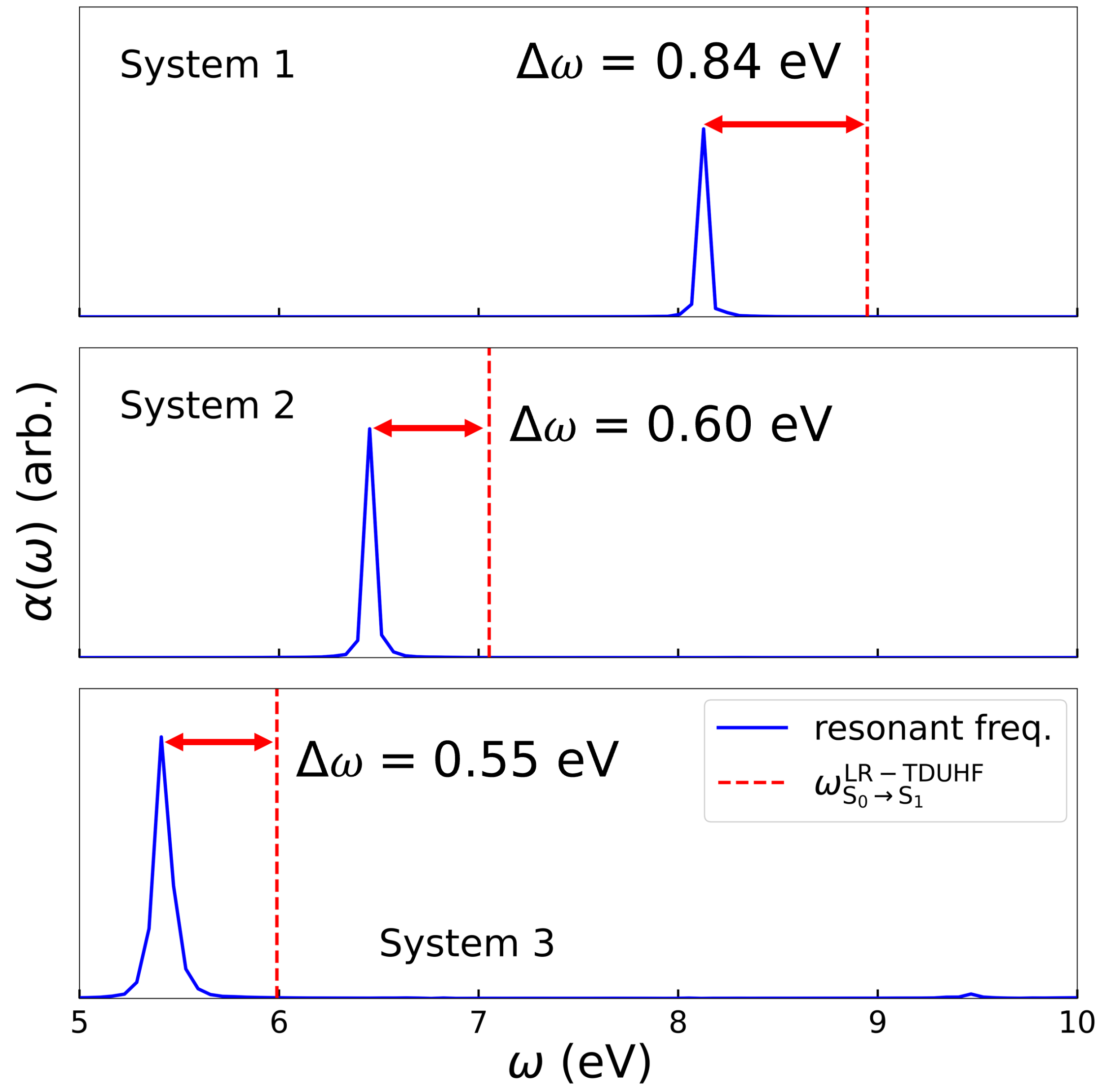

Figure 2.9: Peak shifts observed in the linear absorption spectra, calculated from time-dependent dipole moments obtained using unrestricted RT-TDHF propagation, obtained from the unrestricted linear response $S_0 \rightarrow S_1$ transition resonant-frequency-perturbed Systems using the STO-3G basis set.

2.4 Conclusions

In this study we simulate the electron dynamics for conjugated molecules of increasing size with 40, 54, and 68 electrons, which exhibit charge-transfer nature in the S_1 state, using both TDCIS and RT-TDHF methods. Both methods have the same ground state, with TDCIS having correct physical behavior during field driven processes, whereas the RT-TDHF method has a density-dependent potential, as in RT-TDDFT, and exhibits similar errors as RT-TDDFT within the adiabatic approximation as the electron density is driven from the ground state. We here demonstrate for the first time that if the electron density is driven beyond the ground state using real time electron density propagation, significant size-dependent errors are observed.

We resonantly drive electron dynamics to induce Rabi-like oscillatory behavior in the three molecules, showing that as the system size increases we observe better agreement between the linear response Rabi frequency and the Rabi frequency calculated from real-time TDHF dynamics. For the case of resonant excitation from the S_0 state to a population consistent with the S_1 state, we find that the shifts in peaks of the absorption spectra and the degree of charge transfer obtained from RT-TDHF dynamics show better agreement with the expected LR result with increasing system size.

Overall, the RT-TDHF propagation of the electron density for the largest of the three molecules shows the smallest errors from the expected behavior. However, the errors are still significant for a system with 68 electrons, and it is unclear if the errors will continue to decrease with increasing system size. Although the larger system shows more significant state mixing as seen in the large dipole oscillations and large population of the virtual orbital space, it may be that for charge transfer and resonantly driven electron dynamics that there is indeed smaller errors in real-time electron dynamics for large molecular and materials systems. This finding provides key insight and guidance when performing simulations of the electron transfer pathways in molecules and materials.

2.5 Supplemental Materials

Further details presented in the supplementary material (see Appendix A) include Cartesian coordinates of the three systems studied here, ground and excited state dipole moments, MO transition coefficients, density differences, and time-dependent MO occupations.

Acknowledgments

This work was supported by the U.S. Department of Energy, Office of Science, Office of Basic Energy Sciences under Award Number DE-SC0020203. We acknowledge computational time on the MERCED cluster (funded by NSF ACI-1429783) and on the Pinnacles cluster (funded by NSF ACI-2019144). The authors appreciate helpful discussions with Dr. Hrant P. Hratchian.

Chapter 3

Predicting TDHF dynamics

The failure of the adiabatic approximation in some systems as outlined in Chapters 1, 2 demonstrates that inclusion of memory effects can be important for accurate calculation of time-dependent electronic structure. While complete inclusion of memory effects can be possible in some small systems[46] it is often a computationally intensive task. It is near-impossible to achieve in systems of realistic interest even with rapid expansion of computational capabilities and consequently the scales at which electronic structure theories can be applied. As a result, the more affordable single-reference-based time-dependent methods[27, 64, 81–84, 87–108] and statistical/machine learning models of electronic structure[121–147] have witnessed ever-expanding applications within quantum chemistry. Statistical modeling of time-dependent propagators have proven effective in learning potential energy surfaces[148–159], However, statistical modeling of time-dependent electronic structure remains a relatively unexplored prospect. The Kohn-Sham formalism of time-dependent density-functional theory (TDDFT) and a special case of generalized Kohn-Sham TDDFT, the time-dependent Hartree-Fock theory (TDHF), are commonly used single-reference methods because of their relative affordability for practical applications. This chapter outlines a computational framework developed to learn a statistical model of the TDHF Hamiltonian. The performance of the model in predicting the electron density-matrix dynamics is tested on small molecular systems, with the low propagation test errors highlighting its transferability to arbitrary applied electric-field perturbations of the TDHF Hamiltonian.

The model is shown to propagate the density-matrix well under field-on conditions after learning the field-independent part of the Hamiltonian. The chapter also briefly outlines the extension of this framework to larger molecular systems, demonstrating the feasibility of application of such statistical Hamiltonian models for prediction of electron dynamics in realistic systems.

Author contributions. Sec. 3.1: Karnamohit Ranka was responsible for data-generation (using a custom-developed version of the GAUSSIAN electronic structure code[117]); Dr. Harish S. Bhat was responsible for the development (equations pertaining to the model and model training) and implementation (see Sec. 3.3) of the statistical learning model. Sec. 3.2: Dr. Prachi Gupta and Karnamohit Ranka were responsible for data-generation; Drs. Prachi Gupta and Harish S. Bhat were responsible for the implementation of the statistical learning model.

3.1 Modeling the Hamiltonian

The work[160] introduced in the following sections (reproduced with permission from the authors) has been carried out in collaboration with Dr. Harish S. Bhat (Applied Mathematics, UC Merced) and has been published as: Bhat, H.S., Ranka, K., Isborn, C.M. "Machine Learning a Molecular Hamiltonian for Predicting Electron Dynamics," *International Journal of Dynamics and Control* 8, 1089-1101 (2020). DOI: 10.1007/s40435-020-00699-8.

3.1.1 Introduction

An intriguing new application of machine learning is to predict the dynamical electronic properties of a molecular system [124, 125, 127], which is essential to understanding phenomena such as charge transfer and response to an applied laser field. When discussing such electron dynamics predictions, we must start with the electronic TDSE:

$$i\frac{\partial\Psi(\mathbf{r},t)}{\partial t} = \hat{H}(\mathbf{r},t)\Psi(\mathbf{r},t). \tag{3.1}$$

Here $\hat{H}(\mathbf{r}, t)$ is the electronic Hamiltonian operator that operates on the time-dependent many-body electronic wave function $\Psi(\mathbf{r}, t)$, where $\mathbf{r}$ represents the spatial and spin coordinates of all electrons. One can derive from Eq. (3.1) an evolution equation for the time-dependent density operator. This operator equation can be represented in a finite-dimensional basis, yielding a matrix system of ordinary differential equations:

$$i\frac{\partial \mathbf{P}'(t)}{\partial t} = \Big[\mathbf{H}'(t), \mathbf{P}'(t)\Big]. \tag{3.2}$$

We call this the quantum Liouville-von Neumann equation. Boldface capital letters denote matrices, representations of operators in particular bases. Primes denote representations of operators in an orthonormal basis. Here $\mathbf{P}'(t)$ and $\mathbf{H}'(t)$ are time-dependent density and Hamiltonian matrices, respectively. The square brackets on the right-hand side denote a commutator; for matrices $\mathbf{A}$ and $\mathbf{B}$, the commutator is $[\mathbf{A}, \mathbf{B}] = \mathbf{AB} - \mathbf{BA}$.

Inspecting a particular molecular system, one determines and writes the system's Hamiltonian, a sum of kinetic and potential energy operators. As the Hamiltonian includes spatial derivatives within the kinetic energy operator, Eq. (3.1) will be a partial differential equation (PDE). For an N-electron system, ignoring spin, the PDE Eq. (3.1) will feature $3N$ spatial degrees of freedom. As N increases beyond $N = 1$, it becomes intractable to solve Eq. (3.1) directly for the time-dependent many-body wave function $\Psi(\mathbf{r}, t)$, even with modern numerical analysis and high-performance computing. For this reason, molecular electronic structure and dynamics calculations typically use simplified, mean-field approaches. One such approach is time-dependent Hartree-Fock (TDHF)[161, 162] theory, which solves Eq. (3.2) based on a simplified form of the wave function. In HF theory, we approximate the many-body wave function using a Slater determinant, an antisymmetrized product of single-particle orbitals $\phi_i(\mathbf{r}, t)$, where $\mathbf{r}$ now represents the spatial and spin coordinates of one electron. This approximation leads to a modified form of the Hamiltonian $\hat{H}$ that appears in Eq. (3.1). Within HF theory, we then call Eq. (3.2) the TDHF equation.

Eq. (3.2), used within TDHF theory or an alternative, similar approach called time-dependent density functional theory, is used in atomic, molecular, and materials calculations to simulate the dynamic electronic response to a perturbation, including predicting charge transfer and spectroscopic properties [23, 37, 64, 163–166]. In these physical science settings, one starts with a system of interest, e.g., a molecule in an applied electric field. The system's atomic configuration completely determines the Hamiltonian $\mathbf{H}'$ and therefore the right-hand side of Eq. (3.2). Starting from an initial condition, the typical workflow is then to numerically solve Eq. (3.2) forward in time to generate simulations of interest, i.e., to generate $\mathbf{P}'(\mathbf{t})$ for $t > 0$ for a given perturbation.

Note that we write $\mathbf{H}'(t)$ to encapsulate two types of dependence on time t. First, $\mathbf{H}'$ can depend explicitly on time, through $\mathbf{V}_{\text{ext}}$, an external, time-dependent potential detailed below. Second, within HF theory, even if $\mathbf{H}'$ does not depend explicitly on time, it is in general a function of the density $\mathbf{P}'(t)$. In summary, $\mathbf{H}'(t)$ is shorthand for $\mathbf{H}'(t, \mathbf{P}'(t))$. This implies that Eq. (3.2) is in fact a nonlinear system.

In this work, we address a system identification problem for Eq. (3.2). Our main contribution is a computational method to estimate the molecular field-free matrix Hamiltonian $\mathbf{H}'(t)$ from time series observations of density-matrices $\mathbf{P}'(t)$. By building a data-driven model of $\mathbf{H}'$, we identify the right-hand side of Eq. (3.2). We use a linear model for $\mathbf{H}'$, formulate a quadratic loss function that stems from discretizing Eq. (3.2) in time, and eliminate unnecessary degrees of freedom. Thus we reduce model training to a least-squares problem. We demonstrate this method using training data consisting of density-matrices $\mathbf{P}(t)$ for three small molecules.

Among other tests, we use the machine-learned (ML) Hamiltonian to propagate, i.e., to solve Eq. (3.2) forward in time. We find that using the ML Hamiltonian instead of the exact Hamiltonian results in a small, acceptable level of propagation error, even on a time interval that is twice the length of the time interval used for training. We then add a time-dependent external potential to our machine-learned, field-free Hamiltonian; we propagate forward in time using this augmented Hamiltonian. For each of the three molecules we consider, the resulting solutions are in close quantitative agreement with simulations that use the exact Hamiltonian. In short, our machine-learned Hamiltonian extrapolates well to a dynamical setting that differs from that of the training data.

To our knowledge, despite the surge of interest in applying machine learning to molecular simulation [121–123, 126, 129–144], there are no other procedures in the literature to estimate molecular Hamiltonians from density-matrix time series. Our work shares goals with other efforts to learn Hamiltonians, or energy functions and functionals that are ingredients in Hamiltonians. In this space, we primarily see efforts to learn classical Hamiltonians from time series [167–175] as well as efforts to learn quantum Hamiltonians or potentials for time-independent problems [128, 149, 176–178]. Recently, a neural network method to learn the exchange-correlation functional in time-dependent density functional theory has been developed [179]; solutions of the corresponding TDSE are used to train the networks.

We consider small molecular systems modeled with a small basis set in order to focus on methodological development and careful analysis of errors. The present work forms a foundation on which we can build towards studying systems and theories (such as time-dependent density functional theory) in which the underlying potentials and functionals have yet to be completely determined. This is the overarching motivation for pursuing the present work.

We view the task of (i) training with field-off data and (ii) predicting for field-on systems as an extrapolation task, and we aim to learn the molecular potential of the TDHF Hamiltonian in Eq. (3.2), and use the learned potential to accurately predict the dynamics with the field on.

3.1.2 Physical Considerations

3.1.2.1 Time-Dependent Hartree-Fock

In Sec. 3.1.1, we provided a highly summarized conceptual overview of deriving the TDHF equation from the TDSE. Here we expand on this overview and give more mathematical details. All equations use atomic units, with $e^2 = \hbar = m_e = 1$. An external perturbation, such as an applied electric field, within the Hamiltonian will give rise to the time-evolution of the wave function that dictates all properties of a quantum electronic system.

The details of the TDHF method, including the time-dependent Fock operator, are provided in Chapter 1, in Sec. 1.3.2. In this work, the external perturbation to the TDHF Hamiltonian (denoted as **H** here instead of **F**) is an electric field treated classically within the dipole approximation $\hat{V}_{\text{ext}}(\mathbf{r}, t) = \mathbf{E}(t) \cdot \hat{\mu}(\mathbf{r})$.

Using the HF orbitals, $\{\phi_i\}$ introduced in Chapter 1 we next define a (reduced one-body) density operator, $\hat{\rho}$, that allows us to represent the total density of electrons[180]:

$$\hat{\rho}(\mathbf{r}, t) = \sum_p f_p \phi_p(\mathbf{r}, t)\phi_p^*(\mathbf{r}, t) = \sum_p f_p |\phi_p\rangle\langle\phi_p|, \tag{3.3}$$

where f_p is the occupation of orbital ϕ_p: in a restricted, closed-shell system, $f_p = 2$ (if ϕ_p is occupied) or 0 (if ϕ_p is unoccupied). The corresponding density-matrix (**P**) is represented in the basis of $\{\phi_i\}$ as:

$$P_{ij}(t) = \int d\mathbf{r} \phi_i^*(\mathbf{r}, t)\hat{\rho}(\mathbf{r}, t)\phi_j(\mathbf{r}, t) = \langle\phi_i|\hat{\rho}|\phi_j\rangle. \tag{3.4}$$

We can now write down the Liouville-von Neumann equation in operator form:

$$i\frac{\partial\hat{\rho}(\mathbf{r}, t)}{\partial t} = [\hat{H}(\mathbf{r}, t), \hat{\rho}(\mathbf{r}, t)]. \tag{3.5}$$

This is an operator equation for the evolution of $\hat{\rho}$. The time-dependent molecular orbitals ϕ_i are often created from a linear combination of basis functions $\{\chi_\mu\}$, as $\phi_i = \sum_\mu c_{\mu,i}(t)\chi_\mu$, where $c_{\mu,i}(t)$ are the time-dependent coefficients. The elements of the density-matrix **P** are given in this basis by (see Eq. (1.18))

$$P_{\mu\nu}(t) = \sum_p f_p c_{\mu,p}(t) c_{\nu,p}^*(t). \tag{3.6}$$

We transform **P** to an orthonormal basis, yielding $\mathbf{P}'$ (see Appendix B). We then use the Liouville equation for the density operator to write the TDHF equation in matrix form

$$i\frac{\partial\mathbf{P}'(t)}{\partial t} = \Big[\mathbf{H}'(t), \mathbf{P}'(t)\Big], \tag{3.7}$$

where $\mathbf{H}'(t)$ is the Hamiltonian (or Fock) matrix (cf. Eq. (1.19)). In this work, primed notations (e.g., $\mathbf{H}', \mathbf{P}'$) are used for matrices in the orthonormal basis and unprimed notations for matrices (e.g., $\mathbf{H}, \mathbf{P}$) in the atomic orbital (AO) basis.

Although it is straightforward to write down the molecular Hamiltonian if the atomic positions are known, integration of the Hamiltonian within a given basis is more challenging and encodes ground and excited state information about the molecule within that basis. Learning the integrated form of the molecular matrix Hamiltonian is thus key to determining the electron dynamics.

3.1.2.2 Molecules and Exact Hamiltonian

Here we study three diatomic molecules: H_2, HeH^+, and LiH. The atoms in each of these diatomic systems are placed along the z-axis, equidistant from the origin. The interatomic separations for H_2, HeH^+ and LiH are 0.74 Å, 0.772 Å, and 1.53 Å, respectively. These simple molecular systems increase in complexity, going from a symmetric two-electron homonuclear diatomic, to a two-electron heteronuclear diatomic, to a four-electron heteronuclear diatomic. The basis set used for these calculations is STO-3G, a minimal basis set made of s and p AOs. For H_2 and HeH^+, this results in two basis functions (a 2×2 matrix for $\mathbf{P}$ and $\mathbf{H}$), and for LiH this results in six basis functions (a 6×6 matrix for $\mathbf{P}$ and $\mathbf{H}$, although some elements of the matrices are zero due to the linear symmetry of the molecule, as discussed later).

For each molecule, the electronic structure code (GAUSSIAN[117] in the present case) provides the integrals that are the components of the exact Hamiltonian matrix $\mathbf{H}$, expressed in the same AO basis set as the density-matrices. Specifically, we obtain real, symmetric, constant-in-time matrices for the kinetic energy and electron-nuclear potential energy. We also obtain a 4-index tensor of evaluated integrals, which we use together with the time-dependent density-matrices $\mathbf{P}(t)$ to compute the electron-electron potential energy term. These ingredients allow us to compute, for each molecule, the exact Hamiltonian. Electron density propagation with this exact Hamiltonian, both within the electronic structure code and within our propagation code, is compared to that from our ML model Hamiltonian.

3.1.3 Electron density-matrix Data

There are two steps involved in generating the training and test sets of the time series of density-matrix data:

1. Generating an initial condition (the initial density-matrix).
2. Generating a trajectory using the initial condition and the differential equation Eq. (3.2) for propagation.

For the first step, the HF stationary state solution is determined self-consistently within the electronic structure code. The density-matrix corresponding to the α spin part of the solution, represented in the AO basis, is used as the initial condition. The second step involves propagating the initial density-matrix using the TDHF equation.

We performed each of these steps with the GAUSSIAN electronic structure program[117], using a locally modified development version.

3.1.3.1 Initial Conditions

We have calculated initial density-matrices for field-free and static field conditions. For the field-free calculations, we set the $\mathbf{V}_{\text{ext}}$ term to 0. For the static field, $E_z = 0.05$ a.u. (atomic units). Applying a static field creates an initial electron density that is not a stationary state of the field-free Hamiltonian and is often referred to as a delta-kick perturbation.

3.1.3.2 Trajectory Data

The density-matrix from the initial condition calculation is used as the starting point for generating the real-time TDHF electron dynamics trajectory, i.e. $\mathbf{P}(t)$.

For the field-free trajectories, we set $\mathbf{V}_{\text{ext}}$ to zero during propagation; we use the density-matrix with the delta-kick perturbation as the initial condition. These trajectories serve as the training data for the ML Hamiltonian. A perturbation that is localized at one point in time is, via Fourier transform, maximally spread out in frequency space. Hence such a perturbation necessarily excites all modes of the system. Therefore, by choosing a delta-kick trajectory that excites all modes, we ensure that it is at least possible in principle to learn the full potential/Hamiltonian.

For the field-on trajectories, the field-free initial density-matrix is used and $\mathbf{V}_{\text{ext}}$ takes the following form during propagation:

$$\mathbf{V}_{\text{ext}}(t) = \sum_{i \in \{x,y,z\}} E_i \sin{(\omega t)} \boldsymbol{\mu}_i = 0.05 \sin{(0.0428t)} \boldsymbol{\mu}_z, \tag{3.8}$$

where the time t, the field-intensity E_i along axis i, and the field-frequency ω are expressed in a.u. Here the field is applied only along the z-direction and $\boldsymbol{\mu_z}$ is the z-component of the dipole moment matrix in the AO basis. The sinusoidal field is switched on for one full cycle (around 3.55 fs) starting at $t = 0$. These field-on trajectories test the ML Hamiltonian in a regime quite outside the field-free training regime.

Using a propagation step-size of 0.002 fs, the total length of each trajectory is 20000 timesteps (thus, each trajectory is 40 fs long). The real-time TDHF implementation in GAUSSIAN uses as its propagation scheme the modified midpoint unitary transformation (MMUT) algorithm[23] (see Sec. 1.3.2).

3.1.4 Learning the Molecular Hamiltonian

For a particular molecule, suppose we are given time series $\{\mathbf{P}'(t_j)\}_{j=0}^{N}$ sampled on an equispaced temporal grid $t_j = j\Delta t$. We assume that $\mathbf{P}'(t)$, the continuous-time trajectory corresponding to our time series, satisfies Eq. (3.2). Our goal is to learn the Hamiltonian $\mathbf{H}'$. Assume that the Hamiltonian contains no explicit time-dependence - this can be ensured by generating training data with no external applied field. Then $\mathbf{H}'$ is a Hermitian matrix of functions of $\mathbf{P}'$, the density-matrix. Our strategy therefore consists of three steps: (i) develop a model of $\mathbf{H}'$ with a finite-dimensional set of parameters β, (ii) derive from Eq. (3.2) a statistical model, and (iii) use the model with available data to estimate β.

Note that in order to obtain $\mathbf{P}', \mathbf{H}'$ from $\mathbf{P}, \mathbf{H}$, we transform from the AO basis to its canonical orthogonalization [7]. We do this because the TDHF equation

Eq. (3.2) holds in an orthonormal basis; the AO basis by itself is not orthonormal (see Appendix B for details).

Let us split $\mathbf{H}'$ into its real and imaginary parts: $\mathbf{H}' = \mathbf{H}'_R + i\mathbf{H}'_I$. By Hermitian symmetry, $\mathbf{H}'$ is determined completely by the upper-triangular component of $\mathbf{H}'_R$ (including the diagonal) and by the upper-triangular component of $\mathbf{H}'_I$ (not including the diagonal). If $\mathbf{H}'$ has size $M \times M$, there are $M(M+1)/2$ elements of $\mathbf{H}'_R$ and $M(M-1)/2$ elements of $\mathbf{H}'_I$ that we must model. Hence there are a total of M^2 real degrees of freedom, which we can represent as an $M^2 \times 1$ vector $\mathbf{h}'$. Note that we can apply this same real and imaginary splitting to $\mathbf{P}'$; since it is also Hermitian, it can also be determined completely by a real vector $\mathbf{p}'$ of dimension $M^2 \times 1$. Then we formulate the following linear model for $\mathbf{h}'(\mathbf{p}')$ - in what follows, we use $\widetilde{}$ to denote either statistical models or their parameters:

$$\widetilde{\mathbf{h}}' = \widetilde{\beta}_0 + \widetilde{\beta}_1 \mathbf{p}' \tag{3.9}$$

Here $\widetilde{\beta}_0$ has size $M^2 \times 1$, while $\widetilde{\beta}_1$ has maximal size $M^2 \times M^2$. For the smaller molecules in our study (H_2 and HeH^+), where the STO-3G basis set leads to a dimension of $M = 2$, we use Eq. (3.9) with no modifications. For LiH, a larger molecule, we recognize entries of $\mathbf{p}'$ that are identically zero and, to help reduce the computational effort required for training, modify the basic model Eq. (3.9).

Note: we have explored higher-order polynomial models that, while remaining linear in the parameters $\widetilde{\beta}$, allow $\widetilde{\mathbf{h}}'$ to depend nonlinearly on $\mathbf{p}'$. We have also explored models in which $\widetilde{\mathbf{h}}'$ is allowed to depend explicitly on time t, including through Fourier terms such as $\sin(\omega t)$ and $\cos(\omega t)$. None of these choices led to any improvement in validation or test error, so we focus on the linear model Eq. (3.9).

Now that we have Eq. (3.9), we turn our attention to Eq. (3.2). Then we use a centered-difference approximation to derive from Eq. (3.2) the statistical model

$$i\frac{\mathbf{P}'(t_{j+1}) - \mathbf{P}'(t_{j-1})}{2\Delta t} = \left[\widetilde{\mathbf{H}}'(\mathbf{P}'(t_j)), \mathbf{P}'(t_j)\right] + \epsilon_j, \tag{3.10}$$

with ϵ_j denoting error. With $\|\mathbf{A}\|_F^2 = \sum_{i,j} A_{ij}^2$, the squared Frobenius norm, we form the sum of squared errors loss function

$$\mathcal{L}(\widetilde{\beta}) = \sum_{j=1}^{N-1} \left\| i\frac{\mathbf{P}'(t_{j+1}) - \mathbf{P}'(t_{j-1})}{2\Delta t} - \left[\widetilde{\mathbf{H}}'(\mathbf{P}'(t_j)), \mathbf{P}'(t_j)\right] \right\|_F^2 . \tag{3.11}$$

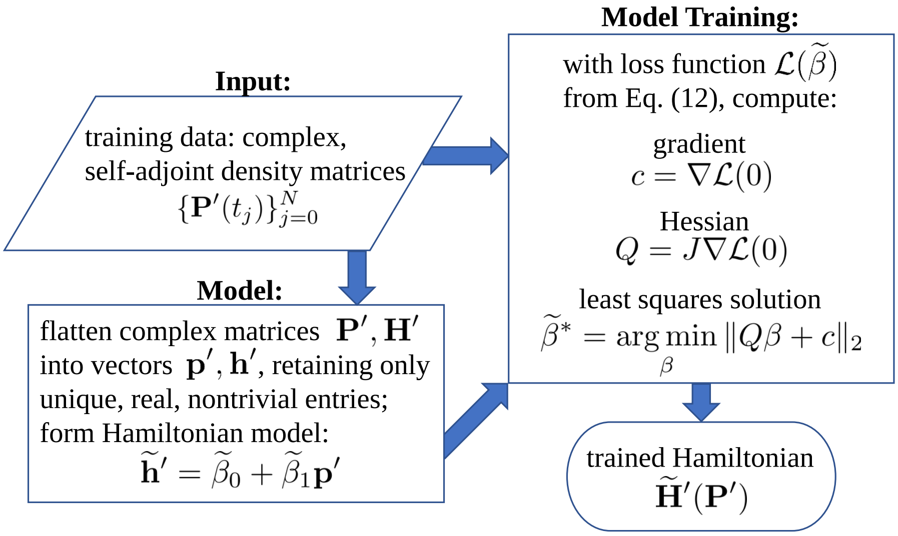

Figure 3.1: Overall training procedure for learning the molecular, field-free Hamiltonian. In this paper, for each molecule, we train using time series with $N = 1000$. We use this field-free Hamiltonian to propagate for $2N = 2000$ steps; see Figs. 3.2 and 3.3. We augment the learned Hamiltonian with an external potential (an electric field), yielding a field-on Hamiltonian that we use to propagate for $2N = 2000$ steps; see Figs. 3.5 and 3.6. Figure courtesy of H.S. Bhat.

3.1.4.1 Reduction to Least Squares

The dependence of $\mathcal{L}$ on $\widetilde{\beta} = (\widetilde{\beta}_0, \widetilde{\beta}_1)$ is entirely through $\widetilde{\mathbf{H}}'$. We estimate $\widetilde{\beta}$ by solving the optimization problem $\widetilde{\beta}^* = \arg\min_\beta \mathcal{L}(\widetilde{\beta})$. Because Eq. (3.9) is linear in the parameters $\widetilde{\beta}$, we observe that Eq. (3.11) must be quadratic in $\widetilde{\beta}$. So, there exist constants Q (matrix), c (vector), and L_0 (scalar) such that

$$\mathcal{L}(\widetilde{\beta}) = \frac{1}{2}\widetilde{\beta}^T Q \widetilde{\beta} + c^T \widetilde{\beta} + \frac{L_0}{2}. \tag{3.12}$$

Here we can identify c as the gradient of $\mathcal{L}$ with respect to $\widetilde{\beta}$ evaluated at $\widetilde{\beta} \equiv 0$, and Q as the Hessian of $\mathcal{L}$ with respect to $\widetilde{\beta}$. We compute this gradient and Hessian via automatic differentiation of $\mathcal{L}$. When Q is full rank, we have an exact minimizer $-Q^{-1}c$. As Q is typically rank deficient, we replace Q^{-1} with the Moore-Penrose pseudoinverse Q^+:

$$\widetilde{\beta}^* = -Q^+ c = \arg\min_{\beta} \|Q\beta + c\|_2. \tag{3.13}$$

When $(I - QQ^+)c = 0$, the loss $\mathcal{L}$ achieves its global minimum at $\widetilde{\beta}^*$. For each of our molecules, we find that $\|(I - QQ^+)c\|$ is small but non-zero. Still, we find empirically that Eq. (3.13) yields a nearly zero-norm gradient of $\mathcal{L}$, as good as what can be achieved via other numerical optimization methods.

We have summarized the overall procedure in Fig. 3.1. Eq. (3.13) constitutes the end of the training procedure. In particular, we use a method in NumPy, `linalg.lstsq`, to compute Eq. (3.13), and so we avoid the full computation of Q^+.

3.1.4.2 Error Metrics

Inserting Eq. (3.13) into Eq. (3.12) and using properties of the pseudoinverse, $(Q^+)^T = (Q^T)^+ = Q^+$ together with $Q^+ Q Q^+ = Q^+$, we obtain the training error

$$\mathcal{L}(\widetilde{\beta}^*) = -\frac{1}{2}\left[c^T Q^+ c + L_0\right],$$

the value of the loss function at the optimal set of parameters. The training error measures a local-in-time error, essentially equivalent to starting at the training data point $\mathbf{P}'(t_j)$, propagating one step forward in time with our learned Hamiltonian Eq. (3.9) and comparing with the very next training data point $\mathbf{P}'(t_{j+1})$. Aggregating these one-step errors - squaring and summing their magnitudes - yields the training error $\mathcal{L}(\widetilde{\beta}^*)$.

We contrast the training error with the propagation error. Once we have solved for the optimal parameter values $\widetilde{\beta}^*$, the model Hamiltonian Eq. (3.9) is completely determined. Using this estimated Hamiltonian with the initial condition $\mathbf{P}'(0)$ from our training time series, we solve Eq. (3.2) forward in time using a Runge-Kutta scheme, generating our statistical estimates of $\widetilde{\mathbf{P}}'(t_j)$ from $j = 1$ up to $j = 2N = 2000$, twice the length of the training data. For the Runge-Kutta integration, we set absolute and relative tolerances to 10^{-12}. We then define the propagation error to be

$$\mathcal{E} = \frac{1}{2N} \sum_{j=1}^{2N} \left\| \mathbf{P}(t_j) - \widetilde{\mathbf{P}}(t_j) \right\|_F . \tag{3.14}$$

In contrast to the training error, Eq. (3.14) measures the divergence between two trajectories - $\mathbf{P}$ (training) and $\widetilde{\mathbf{P}}$ (propagation of ML Hamiltonian) - over many timesteps. Both trajectories have exactly the same initial condition, and hence $j = 0$ is excluded from the sum. For $j > 0$, the two trajectories are computed using different numerical schemes (modified midpoint for the training data and Runge-Kutta for the ML Hamiltonian propagation) and different Hamiltonians. To control for scheme-related error, we compute

$$\mathcal{E}_{\text{Sch}} = \frac{1}{2N} \sum_{j=1}^{2N} \left\| \mathbf{P}(t_j) - \overline{\mathbf{P}}(t_j) \right\|_F , \tag{3.15}$$

where $\overline{\mathbf{P}}(t_j)$ is the result of propagating forward in time using the same Runge-Kutta scheme with the exact Hamiltonian $\mathbf{H}'$. This exact Hamiltonian is built by (i) extracting the Hamiltonian $\mathbf{H}$ in the AO basis from the electronic structure output and then (ii) transforming $\mathbf{H}$ to $\mathbf{H}'$ using the procedure described in Appendix B. In Eq. (3.15), the two trajectories being compared have the same Hamiltonian and differ only in the numerical propagation schemes used to generate them. As a final error metric, we compute

$$\mathcal{E}_{\text{Ham}} = \frac{1}{2N} \sum_{j=1}^{2N} \left\| \widetilde{\mathbf{P}}(t_j) - \overline{\mathbf{P}}(t_j) \right\|_F . \tag{3.16}$$

The two trajectories compared here are computed using the same Runge-Kutta scheme, but with different Hamiltonians. By the triangle inequality, we have $\mathcal{E} \leq \mathcal{E}_{\text{Sch}} + \mathcal{E}_{\text{Ham}}$. We may conceptualize this as breaking down the total error into the error due to different schemes ($\mathcal{E}_{\text{Sch}}$) and the error due to different Hamiltonians ($\mathcal{E}_{\text{Ham}}$).

3.1.5 Results

Table 3.1: After training, we report the training loss and the norm of its gradient, along with three forms of propagation error. All results are for the field-free case. Note that the training error is a sum of squared errors; for each molecule, if we divide by the training data length $N = 10^3$, we obtain mean-squared training errors that are all on the order of 10^{-9}, indicating approximately 4 decimal places of accuracy. The propagation errors show a roughly even breakdown into error due to different schemes versus error due to different Hamiltonians. Data courtesy of H.S. Bhat.

	HeH^+	H_2	LiH
$\mathcal{L}(\widetilde{\beta}^*)$	4.75×10^{-6}	5.77×10^{-6}	2.30×10^{-6}
$\lVert\nabla\mathcal{L}(\widetilde{\beta}^*)\rVert$	4.17×10^{-11}	3.44×10^{-11}	6.47×10^{-11}
$\mathcal{E}$	4.37×10^{-3}	4.89×10^{-3}	6.51×10^{-3}
$\mathcal{E}_{\text{Sch}}$	2.57×10^{-3}	2.50×10^{-3}	2.15×10^{-3}
$\mathcal{E}_{\text{Ham}}$	1.81×10^{-3}	2.40×10^{-3}	5.41×10^{-3}

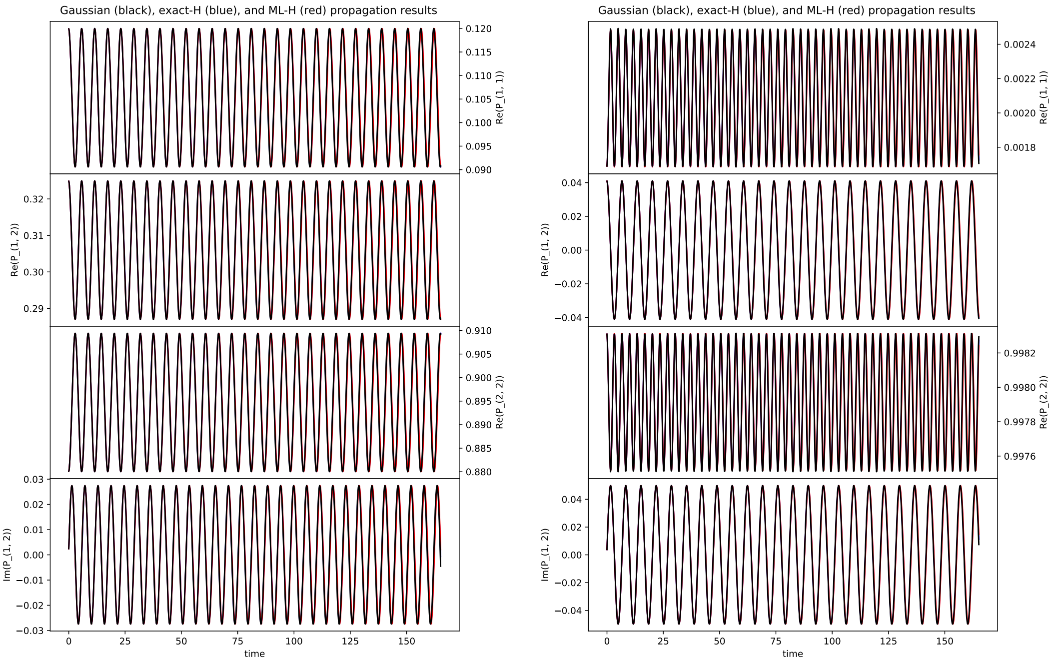

Figure 3.2: HeH^+ , (left) and H_2 (right) propagation with no field. For both molecules, we have plotted all unique real and imaginary parts of the time-dependent density-matrices: actual training data (black), exact Hamiltonian propagation (blue), and ML Hamiltonian propagation (red). Note the close agreement of all three curves, on a time interval that is twice the length used for training. Figure courtesy of H.S. Bhat.

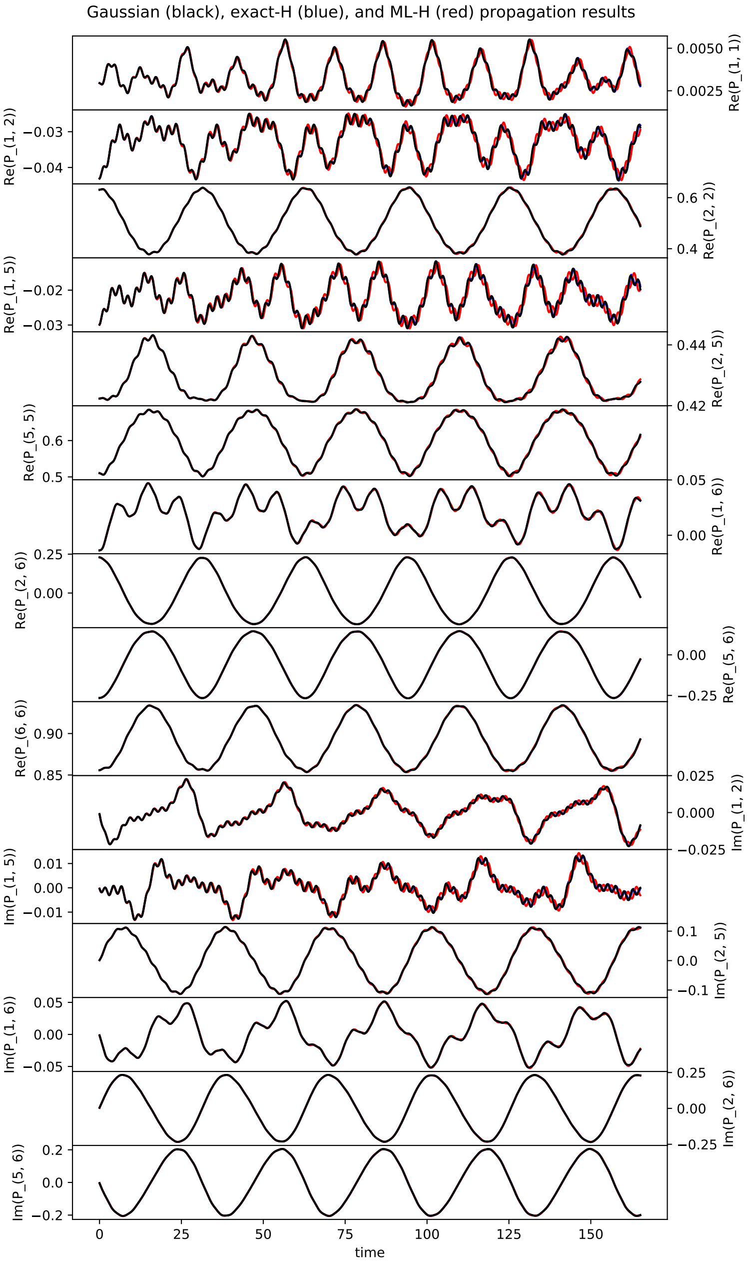

Figure 3.3: LiH propagation with no field. We have plotted all unique real and imaginary parts of the time-dependent density-matrices: actual training data (black), exact Hamiltonian propagation (blue), and ML Hamiltonian propagation (red). For density-matrix elements with small variance, we discern slight disagreement especially at large times. For large-variance density-matrix elements, the curves are in close agreement. Figure courtesy of H.S. Bhat.

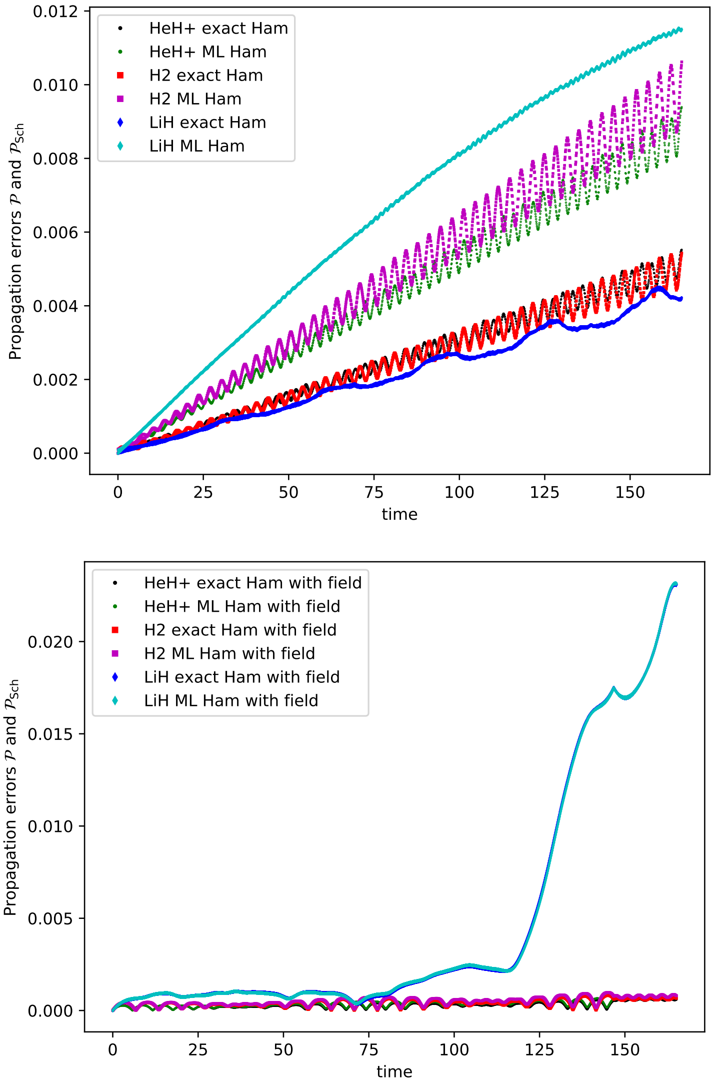

Figure 3.4: Time-dependent propagation errors in which we compare the training data against either $\widetilde{\mathbf{P}}$, the result of propagating the ML Hamiltonian, or $\overline{\mathbf{P}}$, the result of propagating the exact Hamiltonian. All calculations on the top (respectively, bottom) are for the field-free (respectively, field-on) problem. For each molecule, the error incurred by propagating with the ML Hamiltonian is within a constant factor of the error incurred by propagating with the exact Hamiltonian. At the final time, all errors are on the order of 10^{-3}, except for the field-on calculations with LiH. The average values of these curves over all time correspond precisely to $\mathcal{E}$ and $\mathcal{E}_{\mathrm{Sch}}$ - see Eqs. (3.14), (3.15), and Table 3.1 for further details. Figure courtesy of H.S. Bhat.

3.1.5.1 Training and Propagation Tests

We apply the procedure described in Sec. 3.1.4 to training time series of length $N = 1000$ for each of the three molecules HeH^+, H_2, and LiH. See Sec. 3.1.3 for details on the generation of training data. The only additional pre-processing step here was to omit the first two timesteps, for each molecule, and to take the subsequent 1000 timesteps as training data. This was carried out purely to avoid large numerical time-derivatives $\partial \mathbf{P}'/\partial t$ associated with the delta-kick perturbation at $t = 0$; these time-derivatives form a critical part of our loss function Eq. (3.11). We emphasize that these training trajectories were generated with no external potential/field, using delta-kick initial conditions described in Sec. 3.1.3.1.

We report the value of the loss and the norm of its gradient, after training, in the first two rows of Table 3.1. For each molecule, the training loss is of the order of 10^{-6}, which corresponds to an accuracy of roughly 4 decimal places. In order to visualize this accuracy, see Figs. 3.2 and 3.3. For each molecule, we have plotted each of the non-zero real and imaginary components (note the y-axis labels) that fully determine the Hermitian density-matrices $\mathbf{P}'(t_j)$ at each time step $t_j = j\Delta t$. In fact, in each panel, there are three curves: in black, we have plotted the actual training data produced by the electronic structure code; in blue, we have plotted $\overline{\mathbf{P}}(t_j)$, the result of propagating the exact Hamiltonian; and in red, we have plotted $\widetilde{\mathbf{P}}(t_j)$, the result of propagating the ML Hamiltonian.

For HeH^+ and H_2, (Fig. 3.2), the curves agree to a degree where they can hardly be distinguished. As we described above, due to the fact that in HF theory $\mathbf{H}'$ depends on $\mathbf{P}'$, the TDHF equation Eq. (3.2) is nonlinear, and hence all of these oscillations are nonlinear oscillations. For LiH , (Fig. 3.3), we can discern some divergence between the result of ML Hamiltonian propagation (red) and the other two curves, but only for those density-matrix elements with relatively small variance. The sum of squares loss function Eq. (3.11) is biased in favor of fitting large-variance components; to avoid this, one could modify Eq. (3.11) to include weights that are inversely proportional to density element variances. The errors in Fig. 3.3 consist primarily of oscillations about the black curve; the magnitudes of these oscillations are small and do not increase dramatically over time. The machine-learned Hamiltonian performs well when used to propagate for $2N = 2000$ steps, twice the length of the training data used. This hints at being able to use the machine-learned Hamiltonian to extrapolate beyond the field-free system used for training.

To understand the different sources of error, we refer to the final three rows of Table 3.1 together with the left panel of Fig. 3.4. We think of $\mathcal{E}$ as the overall RMS error between the training data $\mathbf{P}'$ and our predicted trajectory $\widetilde{\mathbf{P}}$, broken down into two components $\mathcal{E}_{\text{sch}}$ and $\mathcal{E}_{\text{Ham}}$ as explained above. If our goal is to track the training data, we incur errors of the same order of magnitude when we use either the ML Hamiltonian or the exact Hamiltonian. Consistent with Fig. 3.3, we find the largest gap between exact and ML Hamiltonian propagation for LiH.

Table 3.2: For the field-on problem, we report three forms of propagation error corresponding to field-on versions of Eqs. (3.14), (3.15), and (3.16). Here $\mathcal{E}$ measures the difference between (i) propagation of the ML Hamiltonian plus $\mathbf{V}_{\text{ext}}$ and (ii) the output of an electronic structure code for the field-on problem; $\mathcal{E}_{\text{Sch}}$ measures the difference between (ii) and (iii) propagation of the exact Hamiltonian plus $\mathbf{V}_{\text{ext}}$. Finally, $\mathcal{E}_{\text{Ham}}$ measures the difference between (i) and (iii). Overall, we find that the errors are lower than in Table 3.1, indicating that the ML Hamiltonian succeeds in solving the field-on problem. Data courtesy of H.S. Bhat.

	HeH^+	H_2	LiH
$\mathcal{E}$	3.59×10^{-4}	4.97×10^{-4}	4.86×10^{-3}
$\mathcal{E}_{\text{Sch}}$	2.94×10^{-4}	4.10×10^{-4}	4.87×10^{-3}
$\mathcal{E}_{\text{Ham}}$	7.22×10^{-5}	1.01×10^{-4}	1.33×10^{-4}

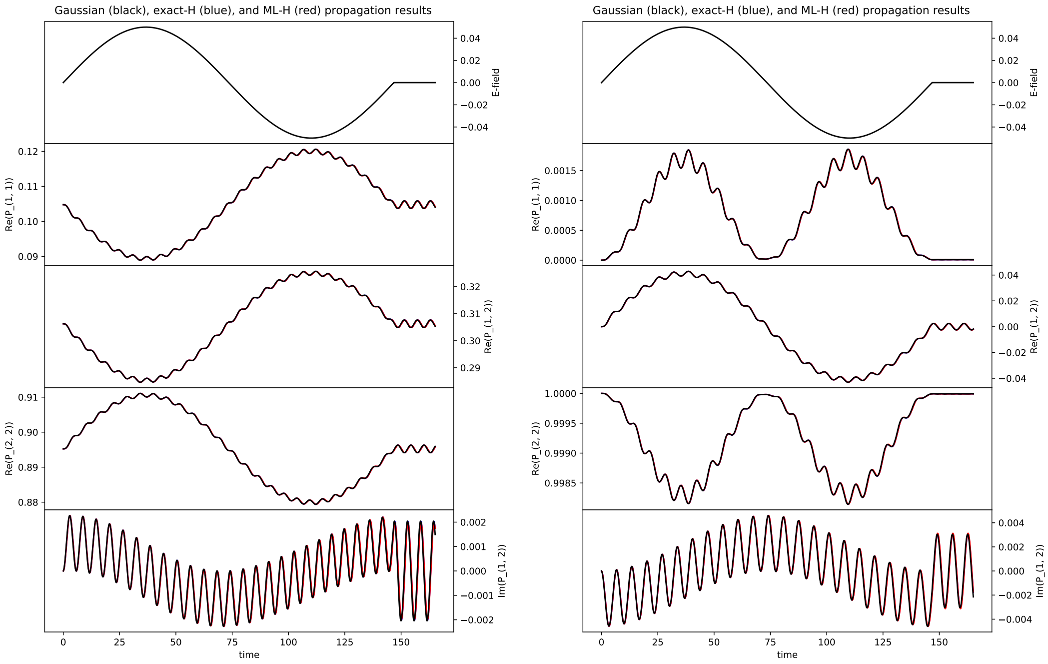

Figure 3.5: HeH^+ (left) and H_2 (right) propagation with field. The top panel of each plot gives the applied electric field Eq. (3.8). In subsequent panels, for both molecules, we plot all unique real and imaginary parts of the time-dependent density-matrices: actual training data (black), exact Hamiltonian propagation (blue), and ML Hamiltonian propagation (red). By ML Hamiltonian, we mean the Hamiltonian trained on the field-free data plus $\mathbf{V}_{\text{ext}}$ given by Eq. (3.8). Note the close agreement of all three curves, on a time interval that is twice the length used for training. This is a true test of whether the learned Hamiltonian can extrapolate to problem settings beyond the one used for training. Figure courtesy of H.S. Bhat.

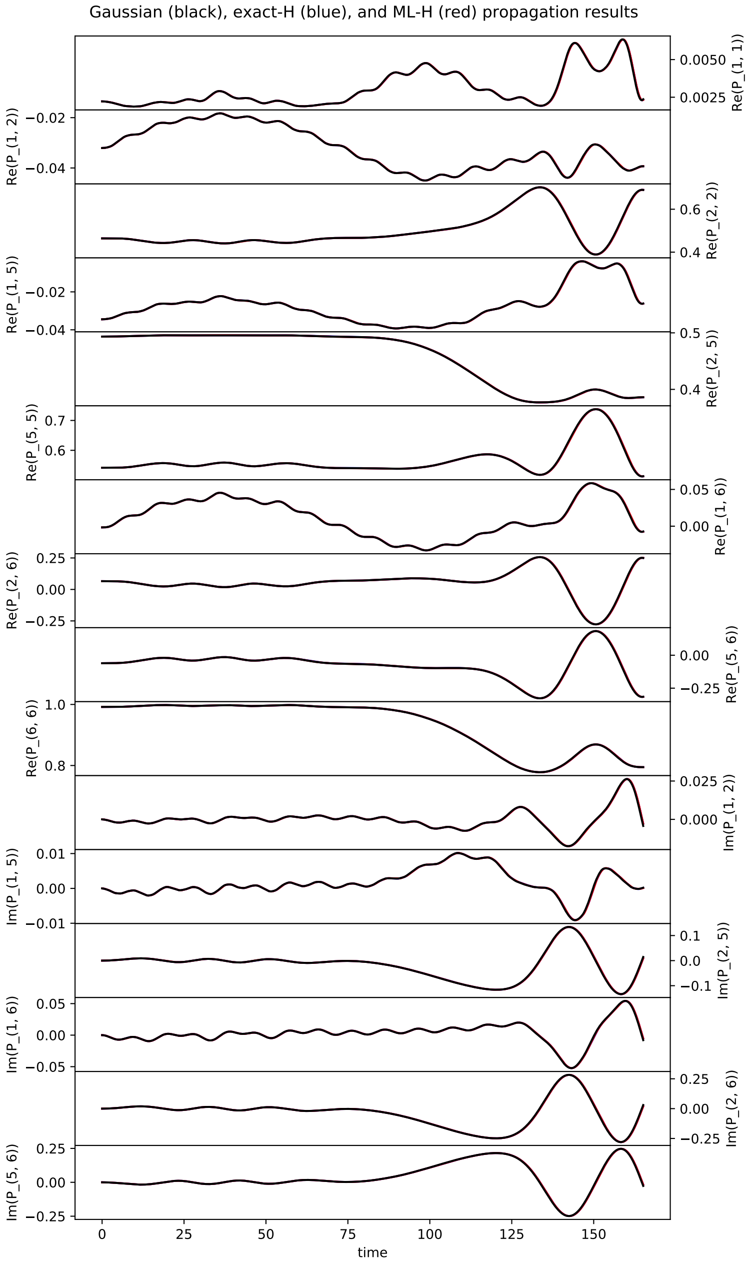

Figure 3.6: LiH propagation with field. We plot all unique real and imaginary parts of the time-dependent density-matrices: actual training data (black), exact Hamiltonian propagation (blue), and ML Hamiltonian propagation (red). By ML Hamiltonian, we mean the Hamiltonian trained on the field-free LiH data plus $\mathbf{V}_{\text{ext}}$ given by Eq. (3.8). Note the close agreement of all curves, on a time interval that is twice the length used for training. This is a true test of whether the learned Hamiltonian can extrapolate to problem settings beyond the one used for training. Figure courtesy of H.S. Bhat.

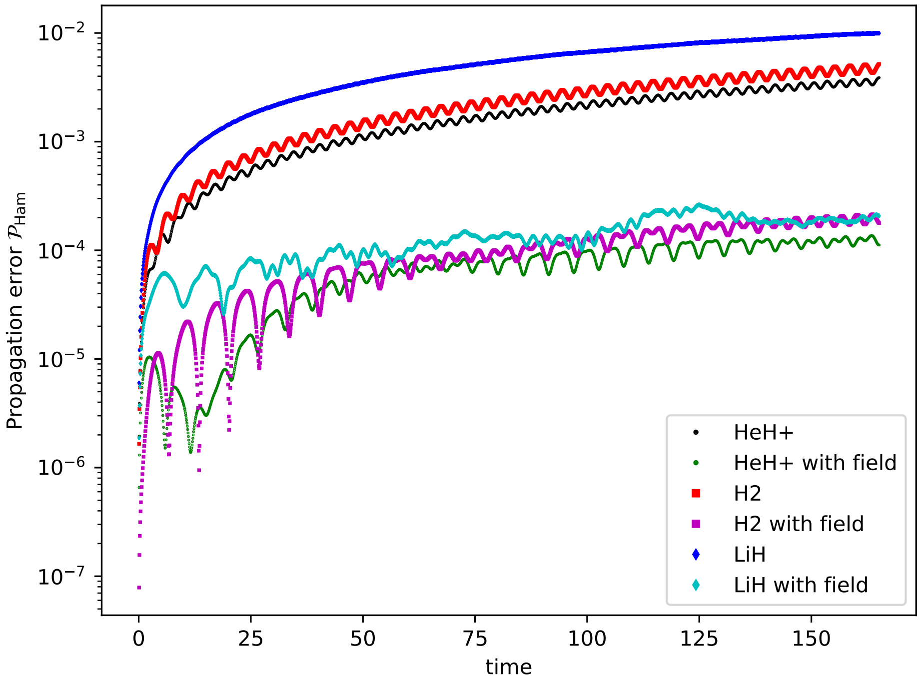

Figure 3.7: Time-dependent propagation errors in which we compare $\widetilde{\mathbf{P}}$, the result of propagating the ML Hamiltonian, with $\overline{\mathbf{P}}$, the result of propagating the exact Hamiltonian. All results were computed using the same Runge-Kutta scheme, isolating the error due to the different Hamiltonians. We include both field-free and field-on calculations. Note that all results are plotted on a log scale. The results show that when we propagate both the ML and exact Hamiltonians using the same scheme, the errors between the two resulting trajectories remain small even as we take hundreds of timesteps. The average values of these curves over all time correspond precisely to $\mathcal{E}_{\mathrm{Ham}}$ - see Eq. (3.16) and Table 3.1 for further details. Figure courtesy of H.S. Bhat.

3.1.5.2 Electric Field Tests

Upon comparing the values of $\mathbf{H}'(t)$ and $\widetilde{\mathbf{H}}'(t)$ along the training trajectories, we find that the ML Hamiltonian does not equal the exact Hamiltonian. To test whether the ML Hamiltonian can predict dynamics outside the training regime we augment the ML Hamiltonian with an applied electric field, i.e., the time-dependent external potential $\mathbf{V}_{\mathrm{ext}}$ given in Eq. (3.8). Using the same Runge-Kutta scheme and tolerances described earlier, we propagate for $2N = 2000$ steps and compare these results with test data produced by an electronic structure code, and also the results of propagating the exact Hamiltonian, augmented with $\mathbf{V}_{\text{ext}}$, via our Runge-Kutta method.

For a first view of the field-on results, see Table 3.2 and Figs. 3.5 and 3.6. In particular, the top panels of Fig. 3.5 show the applied electric field; note that it is switched off after one period. We can immediately discern that the applied field substantially alters the electron density from the field-off case. Still, in each panel, we see excellent agreement between all three curves in each plot: the ground truth solution produced by an electronic structure code (black), the result of propagating the exact Hamiltonian plus $\mathbf{V}_{\text{ext}}$ (blue), and the result of propagating the ML Hamiltonian plus $\mathbf{V}_{\text{ext}}$ (red). Table 3.2, in which we find errors that are roughly an order of magnitude lower than those in Table 3.1, confirms that all computed densities are in close quantitative agreement. All the field-on results are for a time interval that is twice the length used for training, and training has been conducted using field-off data only. Overall, we take these results to indicate that the ML Hamiltonian can indeed extrapolate to conditions beyond the one used for training.

For a deeper understanding of the field-on results, we focus on the right panel of Fig. 3.4 and Fig. 3.7. In the right panel of Fig. 3.4, we compare (i) the result of propagating the ML Hamiltonian plus $\mathbf{V}_{\text{ext}}$ against (ii) the ground truth solution, the output of the electronic structure code for the field-on problem. We also compare (ii) with (iii) the result of propagating the exact Hamiltonian plus $\mathbf{V}_{\text{ext}}$. The plots indicate that, for all three molecules and especially for LiH, the error between (i) and (ii) is almost identical to that between (ii) and (iii). This indicates that the bulk of the error is due to our use of a Runge-Kutta scheme instead of the MMUT scheme used in the electronic structure code. To confirm this, we consult Fig. 3.7, in which we compare (i) and (iii) directly. All solutions here are computed using the same Runge-Kutta scheme. For each molecule, we see that the errors for the field-on problems are consistently smaller than those for the field-off problems. We conclude from these results that the ML Hamiltonian can be used to compute the electronic response to an applied electric field.

A short derivation will show that it is not automatic to expect the augmented ML Hamiltonian to propagate correctly. Let us work in continuous time, to eliminate error due to discrete-time propagation; in this idealized setting, we start with the statement that both of our field-free Hamiltonians, $\mathbf{H}'(t)$ (exact) and $\widetilde{\mathbf{H}}'(t)$ (ML), satisfy the TDHF equation:

$$\begin{aligned} i\frac{\partial \mathbf{P}'(t)}{\partial t} &= [\mathbf{H}'(t), \mathbf{P}'(t)] \\ i\frac{\partial \mathbf{P}'(t)}{\partial t} &= [\widetilde{\mathbf{H}}'(t), \mathbf{P}'(t)]. \end{aligned}$$

Subtracting these equations, and defining the error $\boldsymbol{\epsilon}(t) = \mathbf{H}'(t) - \widetilde{\mathbf{H}}'(t)$, we obtain

$$[\boldsymbol{\epsilon}(t), \mathbf{P}'(t)] = 0. \tag{3.17}$$

Now we augment both Hamiltonians with an external field $\mathbf{V}_{\text{ext}}(t)$. Let $\mathbf{P}''(t)$ denote the true density for the problem with the external field. It must satisfy

$$i\frac{\partial \mathbf{P}''(t)}{\partial t} = [\mathbf{H}'(t) + \mathbf{V}_{\text{ext}}(t), \mathbf{P}''(t)].$$

Via $\mathbf{H}'(t) = \boldsymbol{\epsilon}(t) + \widetilde{\mathbf{H}}'(t)$, we obtain

$$i\frac{\partial \mathbf{P}''(t)}{\partial t} = [\widetilde{\mathbf{H}}'(t) + \mathbf{V}_{\text{ext}}(t), \mathbf{P}''(t)] + \underbrace{[\boldsymbol{\epsilon}(t), \mathbf{P}''(t)]}_{*}.$$

As Eq. (3.17) does not in general imply that the starred term vanishes, we cannot conclude that the true density $\mathbf{P}''(t)$ satisfies the TDHF equation with the augmented ML Hamiltonian $\widetilde{\mathbf{H}}'(t) + \mathbf{V}_{\text{ext}}(t)$. Based on the above derivation, if we solve the TDHF equation using the augmented ML Hamiltonian, we expect to obtain a time-dependent density that differs from $\mathbf{P}''(t)$. As we are able to use the ML Hamiltonian successfully on the problem with an applied electric field, we hypothesize that the error $\boldsymbol{\epsilon}(t)$ is structured in a way that enables us to extrapolate to new external field conditions.

3.1.6 Discussion

Our current work demonstrates that, from a single time series consisting of time-dependent density-matrices, we can effectively learn an integrated Hamiltonian matrix. This ML Hamiltonian can be used for propagation in both the field-off and field-on settings. Importantly, training with a single field-free trajectory, our ML Hamiltonian has the potential to predict the electronic response to a large variety of field pulse perturbations, opening the door to laser-field controlled chemistry. The present work leads to two main areas of future work. The first area concerns technical improvements to the procedure itself, including (i) to replace Eq. (3.11) with a weighted loss function, to account for density elements that oscillate on different vertical scales, (ii) to propagate our ML Hamiltonian using the MMUT scheme, thus eliminating the kind of error quantified by $\mathcal{E}_{\mathrm{Sch}}$, and (iii) to further explore reducing the number of degrees of freedom in the ML Hamiltonian. The second area concerns improving our overall understanding of the procedure, and applying it to systems of greater chemical and physical interest. In this area, further work is needed to understand the difference between the exact and ML Hamiltonians, whether this difference can be decreased by training on multiple trajectories, and how far outside the training regime we can push the ML Hamiltonian. We can also seek to learn the $\hat{H}$ operator rather than the $\mathbf{H}$ matrix representation, which is of interest for determining the unknown exchange-correlation potential within time-dependent density functional theory. In this way, we can push this procedure beyond known physics (as explored here) to systems where the underlying potential energy terms are not known with sufficient accuracy or precision.

Acknowledgements

This work was supported by the U.S. Department of Energy, Office of Science, Office of Basic Energy Sciences under Award Number DE-SC0020203. We acknowledge computational time on the MERCED cluster (funded by NSF ACI-1429783), and on the Nautilus cluster, which is supported by the Pacific Research Platform (NSF ACI-1541349), CHASE-CI (NSF CNS-1730158), and Towards a National Research Platform (NSF OAC-1826967). Additional funding for Nautilus has been supplied by the University of California Office of the President.

3.2 Larger Hamiltonians

The statistical model and methodology developed in the previous work in Sec. 3.1 has been extended to larger systems, employing regularization and dimensionality reduction techniques to efficiently find the optimal solution, $\widetilde{\beta}$. Summarized details and results of the extended work[181] are described in the proceeding sections (reproduced with permission from the authors), carried out in collaboration with Drs. Prachi Gupta and Harish S. Bhat (Applied Mathematics, UC Merced) and published as: Gupta, P., Bhat, H.S., Ranka, K., Isborn, C.M. "Statistical Learning for Predicting Density-Matrix Based Electron Dynamics," *Stat* 11, e439 (2021). DOI: 10.1002/sta4.439

3.2.1 Scaling up the model

Our previous work[160] demonstrated that a statistical model (Eq. (3.9)) could be optimized using second-order optimization methods, yielding very low propagation errors for molecular systems with up to $N = 6$ degrees of freedom (DOFs). However, with increasing number of DOFs (up to $N = 29$ in the present case), using second-order methods can become infeasible. The molecules used for scaled up application of the previous model are H_2 (6-31G basis set; 2 electrons with $N = 4$ basis functions), HeH^+ (6-31G and 6-311++G** basis sets; 2 electrons with 4 and 14 basis functions, respectively), LiH (6-31G and 6-311++G** basis sets; 4 electrons with 11 and 29 basis functions, respectively), and C_2H_4 (STO-3G basis set; 16 electrons with 14 basis functions).

Using automatic differentiation as in Sec. 3.1 to calculate the Hessian matrices of larger systems results in large computational times for obtaining optimized models, and the propagation errors are observed to be unacceptably high. These problems have been overcome by efficient calculation of the gradients and Hessians of the loss function Eq. (3.11), and using the techniques of ridge regression and dimensionality reduction (see Appendix B).

3.2.1.1 Generating Data

For each molecular system, we apply standard electronic structure methods to compute the ground truth field-free Hamiltonian/Fock matrix $\mathbf{H}(\mathbf{P})$ and variationally determine the ground state electron density-matrix $\mathbf{P}(t = 0) = \mathbf{P}_0$. Using $\mathbf{H}(\mathbf{P})$ and an initial condition $\mathbf{P}(0)$, we compute the system's trajectory by numerically solving Eq. (3.7). To numerically solve Eq. (3.7), we use the MMUT method[11, 23] (see Sec. 1.3.2) and record the data at temporal resolution $\Delta t = 0.08268$ a.u. To determine the Hamiltonian, compute the ground state, and propagate with the MMUT method, we used a modified version of the GAUSSIAN electronic structure code [117].

A trajectory is defined as the time series $\mathbf{P}(t)$ obtained under a specific set of conditions; aside from the initial condition, it is determined primarily by the system's field-free Hamiltonian $\mathbf{H}(\mathbf{P})$, and the an external applied electric field.

1. **Field-free trajectory**: For the field-free trajectory, we use as an initial condition a density-matrix for the system perturbed by a Dirac delta at $t = 0$. This delta-kick perturbation, perfectly localized in time, is delocalized in Fourier space; it is designed to excite all oscillatory modes of the system that couple to the z-direction. With this initial condition, we use an ordinary differential equation (ODE) solver to numerically integrate Eq. (3.7) forward in time for M' timesteps with fixed time step Δt. This yields a trajectory on the time interval $[0, M'\Delta t]$. We refer to this trajectory as field-free because there is no external forcing for $t > 0$. We use the first $M < M'$ steps of the trajectory for training, and the subsequent $M' - M$ steps for validation.

2. **Field-on trajectory**: For the field-on trajectory, we set the initial condition equal to the ground state density-matrix with no perturbations, $\mathbf{P}(0) = \mathbf{P}_0$. Now when we numerically solve Eq. (3.7), we use a time-dependent Hamiltonian $\mathbf{H}(\mathbf{P}, t) = \mathbf{H}(\mathbf{P}) + \mathbf{V}_{\text{ext}}(t)$; this consists of a sum of the true field-free Hamiltonian and an external, time-dependent potential. This external forcing term is $\mathbf{V}_{\text{ext}}(t) = E_z sin(\omega t)\mu_z$, where E_z is the applied electric field in the z direction (along the main molecular bond axis), ω is the electric field

frequency, and μ_z is the z component of the molecular dipole moment. For this study, the electric field is turned on for one cycle (3.55fs = 147a.u.) at $t = 0$, with $\omega = 0.0428$ a.u (an off-resonant frequency corresponding to the neodymium-YAG laser) and $E_z = 0.05$ a.u. We use field-on trajectories to test our learned Hamiltonian.

3.2.2 Results

For the molecular systems listed in Table 3.3, we learn β and determine $\widetilde{\mathbf{H}}$: for smaller molecular systems, we train using time series with 2000 points. For larger systems, we increase the training set size; we determine the number of points by computing a learning curve, plotting test set propagation error against the number of training points.[181]

For propagation, we use RK45 ([182]) to solve Eq. (3.7) numerically with the learned Hamiltonian $\widetilde{\mathbf{H}}$ for 2000 steps. We do this both for the case of a delta-kick perturbation (the same as the training data, a field-off perturbation) and for the case of a sinusoidal electric field perturbation (a field-on perturbation). The field-on perturbation tests the learned Hamiltonian in a regime that is outside that of the training set.

Table 3.3: Molecule, number of elements in the density-matrix, training loss, field-free and field-on propagation error. The systems (and basis sets) studied are H_2 (with STO-3G), HeH^+ (with STO-3G, 6-311++G**), LiH (with 6-31G and 6-311++G**) and C_2H_4 (with STO-3G). **N** indicates the dimension of the basis set. Data courtesy of P. Gupta.

System	Training	λ	**Training**	**Error**	
($\mathbf{N^2}$)	set size		**Loss**	**field-free**	**field-on**
H_2 (16)	1000	0	7.15×10^{-6}	3.09×10^{-3}	6.31×10^{-4}
HeH^+ (16)	2000	0	8.99×10^{-5}	6.50×10^{-3}	2.53×10^{-4}
LiH (121)	2000	1.0×10^{-8}	1.39×10^{-5}	6.82×10^{-3}	6.01×10^{-3}
C_2H_4 (196)	2000	1.1×10^{-6}	2.72×10^{-2}	5.22×10^{-2}	1.38×10^{-3}
HeH^+ (196)	4000	5.2×10^{-12}	4.68×10^{-5}	8.84×10^{-3}	3.02×10^{-4}
LiH (841)	9000	5.0×10^{-6}	4.79×10^{-5}	1.52×10^{-2}	1.71×10^{-1}

The training loss, field-free, and field-on propagation error for six molecular systems are presented in Table 3.3. The training loss reported here is calculated as $\mathcal{L}(\beta^*)$ using Eq. (3.11). This training loss measures the squared Frobenius norm of one-step errors, i.e., the error in propagating to the next time step using the learned Hamiltonian (via Eq. (B.4) in Appendix B). The small values of the field-free error, for all molecules, indicate that the Hamiltonian learned by minimizing Eq. (3.11) can be used for long-term propagation. Even with an applied field, which is outside the training regime, we obtain propagation errors comparable to if not less than those in the field-free case, implying that the learned Hamiltonian generalizes well beyond the training regime.

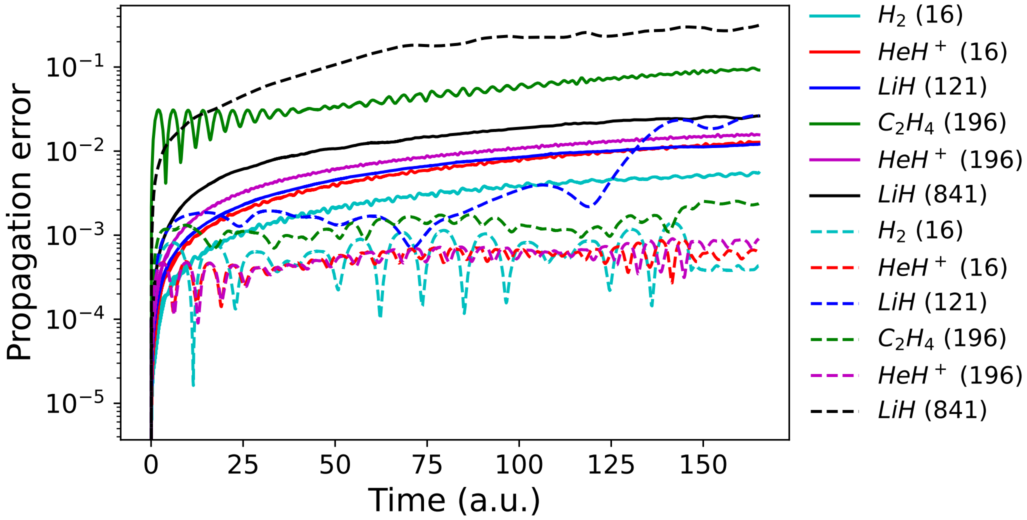

Figure 3.8: Propagation error compares ground truth density-matrices against those computed by numerically solving Eq. (3.7) using the learned Hamiltonian $\widetilde{\mathbf{H}}$. The solid lines are for field-off propagation and the dashed lines are with the field on. Molecules are listed with corresponding size of N^2. Figure courtesy of P. Gupta.

In what follows, we use the phrase propagating the electron density with a Hamiltonian $\mathbf{H}$ to mean solving Eq. (3.7) numerically with that particular $\mathbf{H}$. Let $\mathbf{P}'$ denote the density-matrices obtained by propagating the electron density with the learned Hamiltonian - we think of $\mathbf{P}'$ as the prediction that follows from the learned model. We define the time-dependent propagation error as

$$\mathcal{E}(t_j) = \|\mathbf{P}'(t_j) - \mathbf{P}(t_j)\|_F, \tag{3.18}$$

where $\mathcal{E}(t_j)$ measures the error (at time t_j) between $\mathbf{P}'$, the predicted trajectory obtained by propagating the electron density with the learned Hamiltonian, and $\mathbf{P}$, the ground truth trajectory. We calculate the mean propagation error for the propagation interval as

$$\mathcal{E} = \frac{1}{M_{\text{prop}}} \sum_{j=1}^{M_{\text{prop}}} \mathcal{E}(t_j), \tag{3.19}$$

where M_{prop} is the number of timesteps for which we propagate with the learned Hamiltonian. For this study, $M_{\text{prop}} = 2000$. In Fig. 3.8 we plot the time-dependent propagation errors $\mathcal{E}(t_j)$ for all molecular systems in both the field-free and field-on cases. We see that that errors for both cases remain reasonably small for all molecular systems even after propagating for 150 a.u., which is equivalent to 2000 timesteps.

In Fig. 3.9, we plot, as a function of time, selected nonzero elements of the density-matrix obtained by propagating the electron density with the learned Hamiltonian (red), and the ground truth (blue) obtained from a widely-used electronic structure code[117]. We observe good agreement between predicted and ground truth trajectories.

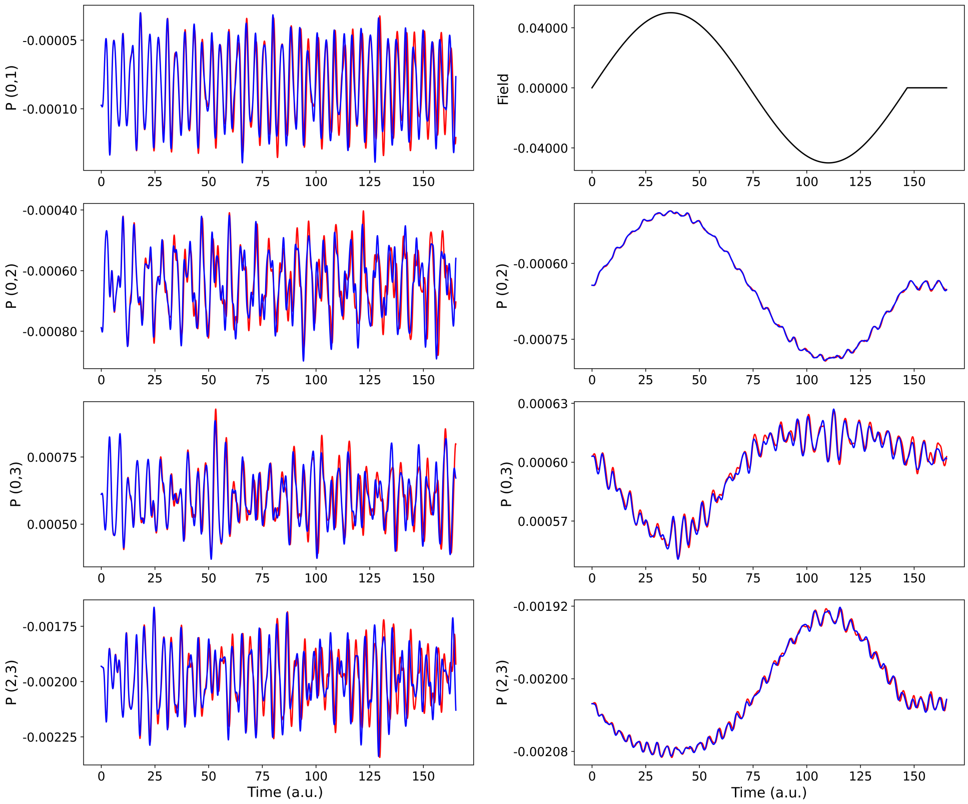

Figure 3.9: Real parts of selected elements of ground truth density-matrices (blue) and density-matrices computed using the learned Hamiltonian $\widetilde{\mathbf{H}}$ (red) for HeH$^+$ in the 6-311++G** basis for the field-free (left) and field-on (right) cases. Note the close agreement between all curves. Figures courtesy of P. Gupta.

3.2.3 Outlook

This work achieves the goal of learning a known, approximate, density-dependent TDHF Hamiltonian[36–38, 183] for more realistic molecular systems than we studied previously[160]. It provides the methodological development for a framework that seeks to model the Hamiltonian and use it to predict the electron dynamics. It makes conceptual and practical progress towards developing novel statistical/machine learning methods for more complex and more realistic theories for predicting electron dynamics, with a future goal of going beyond the HF theory to learn new, more accurate density-dependent Hamiltonians.

Acknowledgments

This work was supported by the U.S. Department of Energy, Office of Science, Office of Basic Energy Sciences under Award Number DE-SC0020203. We acknowledge computational time on the MERCED cluster (funded by NSF ACI-1429783), and on the Nautilus cluster, which is supported by the Pacific Research Platform (NSF ACI-1541349), CHASE-CI (NSF CNS-1730158), and Towards a National Research Platform (NSF OAC-1826967). Additional funding for Nautilus has been supplied by the University of California Office of the President.

3.3 Reproducibility

All code required to reproduce all training and test results is available on GitHub[184] at `https://github.com/hbhat4000/electrondynamics`. Training data is available from the authors upon request.

Chapter 4

Memory in TDCI methods

From Chapter 1 we know that the time-dependent Kohn-Sham formalism can produce a single-reference one-electron density corresponding to the exact one-electron density of an interacting system using an exact XC potential. We also know that the XC potential depends on not only the history of the system's evolution but also its initial state. Therefore, to build a Hamiltonian model capable of propagating a single-reference one-electron density correctly it is necessary to incorporate history of the density (or density-matrix) evolution. As we use more accurate TDCI methods to generate time-dependent densities to train the time-dependent Hamiltonian model it is necessary to understand the amount of history required under certain conditions of external perturbation and the differences between different TDCI approximations in terms of history. In this chapter, we aim to quantify the history required for the TDCIS and TDCASSCF methods to accurately reproduce one-electron density-matrix propagation. This work has been carried out in collaboration with Dr. Harish S. Bhat (Applied Math, UC Merced) and Hardeep Bassi (Applied Math, UC Merced; worked on TDCASSCF results).

4.1 Introduction

Time-dependent configuration interaction (TDCI), a set of methods that use the configuration interaction (CI) ansatz for the wave function in the time-dependent Schrodinger equation (TDSE) (see Chapter 1), can be used to calculate accurate excited state as well as time-dependent dynamical properties of multielectronic systems, which may be induced externally (e.g. through interaction with an applied electric field). In particular, TDCI methods have been previously used to calculate molecular response in intense laser fields[11, 16, 17], to drive electronic dynamics by applying laser pulses[15, 18], to simulate intramolecular charge-transfer dynamics[19], etc. One of the desirable properties of this set of methods is that they can be systematically improved to converge to the exact answer within a finite basis set of one-body electronic wave functions. The accuracy of TDCI methods depends on the number of electronic configurations (substituted, spin-adapted determinants, built from a set of one-body electronic spin-orbitals) used in the wave function ansatz, which scales exponentially as the number of electrons and the corresponding set of one-body orbitals increases. Truncated TDCI methods can be used to save computational costs, but often *a priori* information about the molecular system to be simulated must be used to make such truncations. The caveats involved in application of truncated TDCI methods, and the prohibitive cost of generally accurate TDCI methods, eliminate the possibility of studying electronic systems that might be relevant to large-scale chemical applications.

TDDFT and TDHF methods can be utilized effectively in such cost-prohibitive cases, as a means of simulating electronic dynamics at reduced computational costs[64, 87–89]. Because of the popularity of using these methods for large-scale chemical applications, mitigating any errors associated with these methods (including memory effects) is an important undertaking. Although TDDFT is formally exact, one very common approximation within TDDFT is the adiabatic approximation. Errors associated with the adiabatic approximation are often termed memory effects (see section 1.3.3.1); these effects arise from nonlinearity of the Hamiltonian/Kohn-Sham matrix (with respect to either the propagated density or, equivalently, the one-body electronic spin-orbitals) used in time-dependent density-functional theory (TDDFT) methods, and can affect the accuracy of the computed electronic dynamics[38, 68, 110].

Runge and Gross[34] proved that there exists a one-to-one mapping between the time-dependent density of a system and the external potential, justifying the use of TDDFT to simulate time-dependent electronic phenomena. One of the primary conditions implied within the formalism of TDDFT is that the evolving density depends on the initial state of the system and the evolution of the density. Within the Kohn-Sham formalism[30] of non-interacting particles, this dependence is incorporated into the exchange-correlation (XC) potential of the time-dependent Kohn-Sham Hamiltonian. This dependence on the initial state and the electron density at previous points in time is termed the "memory" of the potential and in practice this condition is rarely satisfied. Most TDDFT calculations instead use ground-state XC functionals, which only depend on the instantaneous time-dependent density (this is known as the adiabatic approximation). The adiabatic approximation leads to qualitative errors in the behavior of electron dynamics: incorrect charge transfer dynamics[46], peak-shifting in time-resolved absorption spectra[68], and incorrect electron dynamics when driven at resonant frequencies[110]. Time-dependent Hartree-Fock (TDHF) theory, which can be considered a special case within the generalized Kohn-Sham formalism of TDDFT[70], suffers from similar issues related to memory effects. It is worth noting, however, that TDHF theory in principle does not account for memory, and thus its application is restricted to the regime of the adiabatic approximation. On the other hand, many electronic processes may occur outside this regime, particularly those driven by resonant frequencies and high intensity external electric fields. It is therefore important to account for memory effects to yield qualitatively and quantitatively accurate electron dynamics.

4.2 Density-matrix and memory

In our previous work[160, 181] (see Chapter 3), we used statistical learning methods to learn a molecular Hamiltonian/Fock matrix as a linear function of the density-matrix using a time-dependent density-matrix generated from a TDHF trajectory. This Hamiltonian model accurately predicts electron dynamics for molecules of varying sizes compared to the ground-truth TDHF trajectories. The model is expected to do well for electron dynamics in systems where the electron density does not change significantly from the reference initial density (e.g. off-resonant and weak-strength perturbations[38]). However, owing to the drawbacks of TDHF, used for generating the training data itself, the Hamiltonian trained using TDHF propagation is prone to similar errors in the regime of resonantly driven processes. It is thus highly desirable to use propagation data from accurate many-body methods to train Hamiltonian models to predict *accurate* electron density-matrices.

However, it is known that different CI ansatzes and different CI methods of propagation can give quantitatively and qualitatively different dynamics depending on the level of truncation.[11, 17, 185] Thus, while TDCI methods may not suffer from the artifacts of memory effects, the accuracy of electron dynamics itself is still dependent on the extent of electronic correlation recovered by the method of choice. The memory effects are thus implicitly present in TDCI propagation methods, but the accuracy of reproducing the *exact* memory effects depends on the level of truncation. One must incorporate memory effects into the exchange-correlation (XC) potential in the time-dependent Kohn-Sham formalism. The memory effects comprise initial-state dependence and history dependence.[53] The initial-state comprises the initial non-interacting Kohn-Sham (KS) wave function and the initial many-body interacting wave function. The many-body wave functions, while necessary for memory effects, can be computationally expensive to calculate. It is thus desirable to model memory effects from just the history of the evolution of electron density (or density-matrix) evolution, but the dependence of the Hamiltonian on previous time-steps is not known. However, in the present case of density-matrix evolution, one can use the fact that the quantity of interest, the one-electron density-matrix (1-RDM), can be constructed from a many-body density-matrix, represented in the basis of stationary states of the chosen method's time-independent Hamiltonian, using the superposition principle. We propose a method that takes advantage of this loss of information to measure the "history" of a TDCI method, which will help inform the construction of the Hamiltonian model that will learn to predict one-electron density-matrices accurately. In the next section we look at how an accurate 1-RDM is calculated, and then introduce the method to model propagation of TDCI using history of 1-RDM evolution.

4.3 The time-dependent 1-RDM

In order to understand how a 1-RDM accurately evolves in a TDCI method, it is important to understand the relation between the full many-body density-matrix as represented in a stationary state basis and the 1-RDM represented in a basis of one-body functions (atomic orbitals, or AOs, in our case). This relationship is explained using an example of a 2-electron, 2-orbital system, such as that found in the hydrogen molecule using a minimal basis set, STO-3G.

4.3.1 The Hartree-Fock (HF) one-electron density-matrix: 2-electron, 2-orbital case

For a 2-electron, 2-orbital system, the restricted HF wave function (formed using the eigenfunctions of the Fock operator, also called molecular orbitals or MOs, $\{\phi_1, \phi_2\}$, see section 1.2.1) is given by a Slater determinant built from *doubly occupied* MOs:

$$\begin{aligned} |\psi^{\mathrm{RHF}}\rangle (\equiv |\psi^{\mathrm{HF}}\rangle) &= \hat{A}(\phi_1(\vec{r}_1)\alpha(\sigma_1)\phi_1(\vec{r}_2)\beta(\sigma_2)) \\ &= \frac{1}{\sqrt{2!}} \cdot (\phi_1(\vec{r}_1)\alpha(\sigma_1)\phi_1(\vec{r}_2)\beta(\sigma_2) \\ &\quad - \phi_1(\vec{r}_1)\beta(\sigma_1)\phi_1(\vec{r}_2)\alpha(\sigma_2)). \end{aligned} \tag{4.1}$$

The one-electron reduced density (1-RD) for the Hartree-Fock wave function is defined as:[1]

$$\rho^{\mathrm{HF}} = 2 \cdot \int_V d\sigma_1 \cdot d\vec{r}_2 \cdot d\sigma_2 \cdot |\psi^{\mathrm{HF}}\rangle\langle\psi^{\mathrm{HF}}| = 2 \cdot |\psi^{\mathrm{HF}}\rangle\langle\psi^{\mathrm{HF}}|_1. \tag{4.2}$$

The MOs, $\{\phi_i\}$, are given by a linear expansion of AOs (centered on the nuclei of respective “atoms” which form the molecule):

$$|\phi_i\rangle = C_1^i \cdot \chi_1 + C_2^i \cdot \chi_2. \tag{4.3}$$

---

[1] the subscript 1 implies that the integral is performed over all non-spatial variables, and all the spatial variables but one, thus yielding a one-particle quantity.

Here $\{\chi_\gamma\}$ is a set of AO functions which acts as the basis for matrix representations of the target 1-RD (HF 1-RD in the current case), and $\{C^i_\gamma\}$ is the set of corresponding linear expansion coefficients of MOs in terms of $\{\chi_\gamma\}$ (more commonly known as MO coefficients). In a vector representation using the AO basis, the MO in Eq. (4.3) may be represented as a (row-)vector:

$$|\phi_i\rangle = \begin{bmatrix} C^i_1 & C^i_2 \end{bmatrix}. \tag{4.4}$$

To get the total one-particle density, $\rho^{\mathrm{HF}}_{\mathrm{total}}(\vec{r})$, corresponding to 2 electrons, we simply multiply the one-particle reduced density in Eq. (4.2) by the number of electrons, 2. Upon substituting and integrating (and expanding MOs as linear combinations of AO basis functions, $\{\chi_\gamma\}$), we get

$$\begin{aligned}\rho^{\mathrm{HF}} &= 2\cdot\phi_1(\vec{r}_1)\cdot\phi_1^*(\vec{r}_1)\\ &= 2\cdot\phi_1\cdot\phi_1^*\\ &= 2\cdot(C^1_1\cdot\chi_1 + C^1_2\cdot\chi_2)\cdot(C^{1*}_1\cdot\chi_1^* + C^{1*}_2\cdot\chi_2^*).\end{aligned}$$

The **Hartree-Fock 1-RDM** is defined as follows:

$$[\mathrm{P}^{\mathrm{HF}}_{\mathrm{AO}}]_{\gamma\eta} = \sum_i^{\text{occ. MOs}} n^i_{\mathrm{occ}}\cdot C^i_\gamma\cdot C^{i*}_\eta, \tag{4.5}$$

where, n^i_{occ} is the occupancy of the i^{th} occupied MO. For solutions of the restricted HF equations for a closed-shell system, n^i_{occ} is equal to 2 (and either 2 or 1 for configurations formed using these solutions, cf. Fig. 4.1).

Thus, assuming the MO coefficients are real, we have

$$\begin{aligned}\rho^{\mathrm{HF}} &= [\mathrm{P}^{\mathrm{HF}}_{\mathrm{AO}}]_{11}\cdot|\chi_1|^2 + [\mathrm{P}^{\mathrm{HF}}_{\mathrm{AO}}]_{22}\cdot|\chi_2|^2\\ &\quad + [\mathrm{P}^{\mathrm{HF}}_{\mathrm{AO}}]_{12}\cdot\chi_1\chi_2^* + [\mathrm{P}^{\mathrm{HF}}_{\mathrm{AO}}]_{21}\cdot\chi_2\chi_1^*\\ &= \sum_{\gamma\eta}^{\mathrm{AOs}}[\mathrm{P}^{\mathrm{HF}}_{\mathrm{AO}}]_{\gamma\eta}\cdot\chi_\gamma\chi_\eta^*.\end{aligned}$$

The one-electron density-matrix formed from the *restricted* HF wave function satisfies the following properties:

- Idempotence:

$$\mathrm{P}^{\mathrm{HF}}\mathrm{S}\mathrm{P}^{\mathrm{HF}} = 2\cdot\mathrm{P}^{\mathrm{HF}}. \tag{4.6}$$

where, S^2 is the overlap matrix of the basis in which P^{HF} is represented (usually this is an overlap matrix of the AO basis, S_{AO}).

- The trace of the density-matrix is equal to the number of electrons in the system, N:

$$\mathrm{Tr}[P^{HF}S] = N. \tag{4.7}$$

The properties above are also satisfied by the one-electron density-matrices of the configurations built by substituting occupied MOs with the unoccupied MOs (both obtained together as a set of solutions to the HF equations).

4.3.1.1 Example: HeH$^+$/STO-3G

The two nuclei are separated by a distance of 0.772 Å. There are two AO basis functions, both spherically symmetric $1s$ orbitals with an associated electronic angular momentum of $l = 0$. The function $\chi_1(\vec{r})$ is centered on the hydrogen nucleus, whereas $\chi_2(\vec{r})$ is centered on the helium nucleus.

The MO-coefficient (row-)vectors are

$$\begin{aligned}\mathcal{C}_1 &= \begin{bmatrix}0.000365(= C_1^1) & 0.999803(= C_2^1)\end{bmatrix}\\ \mathcal{C}_2 &= \begin{bmatrix}1.186690(= C_1^2) & -0.639239(= C_2^2)\end{bmatrix}.\end{aligned} \tag{4.8}$$

The corresponding one-particle reduced HF density-matrix for 2 electrons in the AO basis, P^{HF}_{AO}, is

$$\begin{aligned}P^{HF}_{AO} = 2\cdot\mathcal{C}_1^\dagger\mathcal{C}_1 &= 2\cdot\begin{bmatrix}0.000365\\ 0.999803\end{bmatrix}\cdot\begin{bmatrix}0.000365 & 0.999803\end{bmatrix}\\ &= \begin{bmatrix}0.000 & 0.0008\\ 0.0008 & 1.9992\end{bmatrix}.\end{aligned}$$

The overlap matrix for the AO basis functions used in this case is

$$S_{AO} = \begin{bmatrix}1.000000 & 0.538415\\ 0.538415 & 1.000000\end{bmatrix}. \tag{4.9}$$

---

[2] the elements of the overlap matrix, S_χ, for a basis set $\{\chi_i\}$ are given by $[S_\chi]_{ab} = \int_V d\vec{r}\cdot\chi_a^*(\vec{r})\chi_b(\vec{r}) = \langle\chi_a|\chi_b\rangle$.

This implies that

$$\mathrm{Tr}[\mathrm{P}^{\mathrm{HF}}_{\mathrm{AO}}\mathrm{S}_{\mathrm{AO}}] = 1.999998 \approx 2,$$

and

$$\begin{aligned}\mathrm{P}^{\mathrm{HF}}_{\mathrm{AO}}\mathrm{S}_{\mathrm{AO}}\mathrm{P}^{\mathrm{HF}}_{\mathrm{AO}} &= \begin{bmatrix} 0.000 & 0.0008 \\ 0.0008 & 1.9992 \end{bmatrix} \cdot \begin{bmatrix} 1.000000 & 0.538415 \\ 0.538415 & 1.000000 \end{bmatrix} \cdot \begin{bmatrix} 0.000 & 0.0008 \\ 0.0008 & 1.9992 \end{bmatrix} \\ &= \begin{bmatrix} 5.32899540 \times 10^{-07} & 1.45971112 \times 10^{-3} \\ 1.45971112 \times 10^{-3} & 3.99842071 \end{bmatrix} \approx 2 \cdot \mathrm{P}^{\mathrm{HF}}_{\mathrm{AO}}.\end{aligned}$$

4.3.2 The CI one-electron density-matrices: 2-electron, 2-orbital case

4.3.2.1 CI wave functions

One can, using a reference calculation of a set of occupied and unoccupied MOs (the set of solutions to Eq. (1.7)), build different configurations, like those presented in Figs. 4.1.

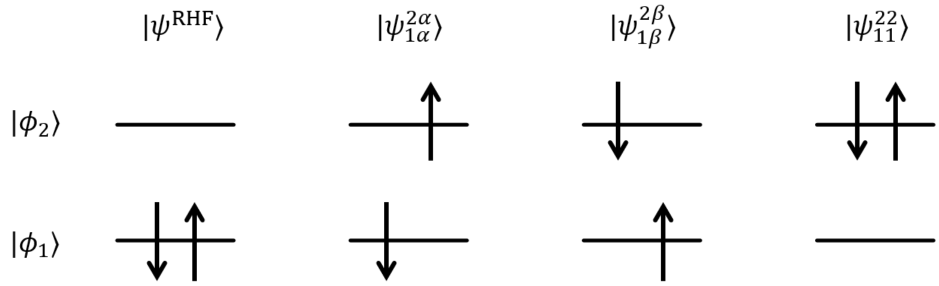

Figure 4.1: Configurations obtained from the restricted Hartree-Fock solution of a 2-electron, 2-orbital system.

The set of configurations thus obtained can be used as an orthonormal and complete basis for building the wave function of a stationary state of the system's electronic Hamiltonian in the following way:

$$\Psi^{\mathrm{CI}}_n = c^{\mathrm{ref}}_n \cdot |\mathrm{ref}\rangle + \sum_{\xi}^{\mathrm{dets.}} c^{\xi}_n \cdot |\xi\rangle \tag{4.10}$$

where, $|\mathrm{ref}\rangle$ is a reference determinant (the Hartree-Fock Slater determinant from Eq. (4.1) in the current case), and $\{|\xi\rangle\}$ is the set of obtained configurations (which are substituted determinants built from the reference determinant). If all such possible substituted determinants are used in the linear expansion given in Eq. (4.10), the corresponding wave function is referred to as the *full* CI solution for state n, given a particular finite basis set of AOs.

Some points need to be considered:

- We consider a set of normalized CI wave functions. Thus, $\sum_{\xi}^{\mathrm{dets.}} |c_A^{\xi}|^2 = 1$
- If we consider the singly-substituted/excited determinants $|\psi_{1\beta}^{2\beta}\rangle$ and $|\psi_{1\alpha}^{2\alpha}\rangle$, they are energetically degenerate in absence of a magnetic field. However, they do not represent a physical wave function as they are not eigenfunctions of the spin multiplicity operator, $\hat{S}^2$, which shares a set of eigenfunctions with the system's Hamiltonian. To make them so, one can take a positive linear combination of them, and a negative linear combination. Upon normalizing these linear combinations, we get the following expression:

$$\psi_{\pm} = \frac{1}{\sqrt{2!}} \cdot (|\psi_{1\beta}^{2\beta}\rangle \pm |\psi_{1\alpha}^{2\alpha}\rangle) \tag{4.11}$$

  The wave functions above are said to be *spin-adapted*, as, being acted upon by the pure spin-operator $\hat{S}^2$, we find that ψ_- is a triplet spin eigenfunction (eigenvalue of 3), and ψ_+ is a singlet spin eigenfunction (eigenvalue of 1). Since we are interested in wave functions of the same multiplicity as our ground state (singlet), we have no contribution from the negative, spin-adapted linear combination, ψ_-. This also means that the individual coefficients of $|\psi_{1\beta}^{2\beta}\rangle$ and $|\psi_{1\alpha}^{2\alpha}\rangle$ are the same (in accordance with the expression for ψ_+, the spin-adapted wave function of singlet multiplicity).

If we have two MOs in a restricted Hartree-Fock (RHF) reference state (both of which can be doubly occupied), $\{\phi_1, \phi_2\}$, the CI wave functions are

$$|\Psi_n^{\mathrm{CI}}\rangle = c_n^{\mathrm{HF}}|\psi^{\mathrm{HF}}\rangle + c_n^{2\beta 1\beta}|\psi_{1\beta}^{2\beta}\rangle + c_n^{2\alpha 1\alpha}|\psi_{1\alpha}^{2\alpha}\rangle + c_n^{2211}|\psi_{11}^{22}\rangle \tag{4.12}$$

4.3.2.2 CI one-electron density-matrices

Using the ansatz in Eq. (4.10) for a 2-electron system (and representing spin and spatial variables $\{(\vec{r_i}, \sigma_i)\}$ collectively as $\{\mathbf{x}_i\}$), the 1-RD for, say, CI state n, is given by

$$\begin{aligned}\rho_{nn}^{\mathrm{CI}} &= 2 \cdot |\Psi_n^{\mathrm{CI}}\rangle\langle\Psi_n^{\mathrm{CI}}|_1 \\ &= 2 \cdot \int_V d\sigma_1 \cdot d\mathbf{x}_2 \cdot \Psi_n^{\mathrm{CI}}(\mathbf{x}_1, \mathbf{x}_2)(\Psi_n^{\mathrm{CI}}(\mathbf{x}_1, \mathbf{x}_2))^*.\end{aligned} \tag{4.13}$$

Similarly, for the transition 1-RD between two CI states, say m and n, we can write down

$$\begin{aligned}\rho_{mn}^{\mathrm{CI}} &= 2 \cdot |\Psi_m^{\mathrm{CI}}\rangle\langle\Psi_n^{\mathrm{CI}}|_1 \\ &= 2 \cdot \int_V d\sigma_1 \cdot d\mathbf{x}_2 \cdot \Psi_m^{\mathrm{CI}}(\mathbf{x}_1, \mathbf{x}_2)(\Psi_n^{\mathrm{CI}}(\mathbf{x}_1, \mathbf{x}_2))^*.\end{aligned} \tag{4.14}$$

In terms of the one-electron density-matrices and transition density-matrices, the 1-RD (transition or otherwise) can be expressed as

$$\rho_{nn}^{\mathrm{CI}} = \sum_{\gamma\eta}^{\mathrm{AOs}} [\mathrm{P}_{\mathrm{AO}}^{nn,\mathrm{CI}}]_{\gamma\eta} \cdot \chi_\gamma \chi_\eta^*; \tag{4.15a}$$

$$\rho_{mn}^{\mathrm{CI}} = \sum_{\gamma\eta}^{\mathrm{AOs}} [\mathrm{P}_{\mathrm{AO}}^{mn,\mathrm{CI}}]_{\gamma\eta} \cdot \chi_\gamma \chi_\eta^*. \tag{4.15b}$$

We can get the one-electron density-matrices (calculated for given CI states or the transition ones calculated between pairs of CI states) as outlined in the next section.

4.3.2.3 Calculating 1-RDM for a CI state, $\mathbf{P}_{\mathbf{AO}}^{nn,\mathbf{CI}}$, using CI expansion coefficients and MO-coefficient vectors

From Eq. (4.13), using the fact that the wave functions of any CI state consist of a linear combination of Slater determinants, we obtain the following expression in terms of MO functions (recall notation from Eq. (4.2)):

$$\begin{aligned}\rho^{\mathrm{CI}}_{nn} = 2\cdot(&|c_n^{\mathrm{HF}}|^2|\psi^{\mathrm{HF}}\rangle\langle\psi^{\mathrm{HF}}|_1 + |c_n^{2\alpha 1\alpha}|^2|\psi^{2\alpha}_{1\alpha}\rangle\langle\psi^{2\alpha}_{1\alpha}|_1\\
&+ |c_n^{2\beta 1\beta}|^2|\psi^{2\beta}_{1\beta}\rangle\langle\psi^{2\beta}_{1\beta}\rangle|_1 + |c_n^{2211}|^2|\psi^{22}_{11}\rangle\langle\psi^{22}_{11}|_1\\
&+ [c_n^{\mathrm{HF}}(c_n^{2\alpha 1\alpha})^*|\psi^{\mathrm{HF}}\rangle\langle\psi^{2\alpha}_{1\alpha}|_1 + \text{c.c.}]\\
&+ [c_n^{\mathrm{HF}}(c_n^{2\beta 1\beta})^*|\psi^{\mathrm{HF}}\rangle\langle\psi^{2\beta}_{1\beta}|_1 + \text{c.c.}]\\
&+ [c_n^{\mathrm{HF}}(c_n^{2211})^*|\psi^{\mathrm{HF}}\rangle\langle\psi^{22}_{11}|_1 + \text{c.c.}]\\
&+ [c_n^{2\alpha 1\alpha}(c_n^{2\beta 1\beta})^*|\psi^{2\alpha}_{1\alpha}\rangle\langle\psi^{2\beta}_{1\beta}|_1 + \text{c.c.}]\\
&+ [c_n^{2\alpha 1\alpha}(c_n^{2211})^*|\psi^{2\alpha}_{1\alpha}\rangle\langle\psi^{22}_{11}|_1 + \text{c.c.}]\\
&+ [c_n^{2\beta 1\beta}(c_n^{2211})^*|\psi^{2\beta}_{1\beta}\rangle\langle\psi^{22}_{11}|_1 + \text{c.c.}]).\end{aligned} \tag{4.16}$$

An example of evaluation of one of the terms in Eq. (4.16) follows:

$$\begin{aligned}|\psi^{\mathrm{HF}}\rangle\langle\psi^{2\alpha}_{1\alpha}|_1 &= \int_V d\sigma_1\cdot d\mathbf{x}_2\cdot(\psi^{\mathrm{HF}}(\mathbf{x}_1,\mathbf{x}_2))(\psi^{2\alpha}_{1\alpha}(\mathbf{x}_1,\mathbf{x}_2))^*\\
&= \frac{1}{\sqrt{2!}}\cdot\frac{1}{\sqrt{2!}}\cdot\int_V d\sigma_1\cdot d\vec{r}_2\cdot d\sigma_2\cdot[(\phi_1(\vec{r}_1)\alpha(\sigma_1)\phi_1(\vec{r}_2)\beta(\sigma_2)\\
&\quad-(\phi_1(\vec{r}_1)\beta(\sigma_1)\phi_1(\vec{r}_2)\alpha(\sigma_2)]\cdot[\phi_1^*(\vec{r}_1)\beta^*(\sigma_1)\phi_2^*(\vec{r}_2)\alpha^*(\sigma_2)\\
&\quad-\phi_2^*(\vec{r}_1)\alpha^*(\sigma_1)\phi_1^*(\vec{r}_2)\beta^*(\sigma_2)]\\
&= \frac{1}{2}\cdot\int_V d\sigma_1\cdot d\vec{r}_2\cdot d\sigma_2\cdot[\phi_1(\vec{r}_1)\alpha(\sigma_1)\phi_1^*(\vec{r}_1)\beta^*(\sigma_1)\\
&\qquad\phi_1(\vec{r}_2)\beta(\sigma_2)\phi_2^*(\vec{r}_2)\alpha^*(\sigma_2)\\
&\quad-\phi_1(\vec{r}_1)\alpha(\sigma_1)\phi_2^*(\vec{r}_1)\alpha^*(\sigma_1)\phi_1(\vec{r}_2)\beta(\sigma_2)\phi_1^*(\vec{r}_2)\beta^*(\sigma_2)\\
&\quad-\phi_1(\vec{r}_1)\beta(\sigma_1)\phi_1^*(\vec{r}_1)\beta^*(\sigma_1)\phi_1(\vec{r}_2)\alpha(\sigma_2)\phi_2^*(\vec{r}_2)\alpha^*(\sigma_2)\\
&\quad+\phi_1(\vec{r}_1)\beta(\sigma_1)\phi_2^*(\vec{r}_1)\alpha^*(\sigma_1)\phi_1(\vec{r}_2)\alpha(\sigma_2)\phi_1^*(\vec{r}_2)\beta^*(\sigma_2)].\end{aligned} \tag{4.17}$$

Due to the orthonormality of the MOs and that of the spin functions, $\alpha(\sigma)$ and $\beta(\sigma)$, the following identities hold (with V denoting spatial and spin phase-spaces below):

$$\int_V d\vec{r} \cdot \phi_i(\vec{r})\phi_j^*(\vec{r}) = \delta_{ij} \tag{4.18a}$$

$$\int_V d\sigma \cdot \alpha(\sigma)\beta^*(\sigma) = 0$$

$$\int_V d\sigma \cdot \alpha(\sigma)\alpha^*(\sigma) = 1 \tag{4.18b}$$

$$\int_V d\sigma \cdot \beta(\sigma)\beta^*(\sigma) = 1.$$

Using Eqs. (4.17), (4.18a) and (4.18b) and integrating the spin-coordinates first, we find

$$\begin{aligned} |\psi^{\mathrm{HF}}\rangle\langle\psi_{1\alpha}^{2\alpha}|_1 = \frac{1}{2} \cdot \int_V d\vec{r}_2 \cdot [&-\phi_1(\vec{r}_1)\phi_2^*(\vec{r}_1)\phi_1(\vec{r}_2)\phi_1^*(\vec{r}_2) \\ &- \phi_1(\vec{r}_1)\phi_1^*(\vec{r}_1)\phi_1(\vec{r}_2)\phi_2^*(\vec{r}_2)]. \end{aligned}$$

Upon integrating further over $\vec{r}_2$, we get the following expression:

$$\begin{aligned} |\psi^{\mathrm{HF}}\rangle\langle\psi_{1\alpha}^{2\alpha}|_1 &= -\frac{1}{2} \cdot |\phi_1\rangle\langle\phi_2| \\ &= -\frac{1}{2} \cdot |\phi_2\rangle\langle\phi_1|^\dagger = |\psi_{1\alpha}^{2\alpha}\rangle\langle\psi^{\mathrm{HF}}|_1^\dagger. \end{aligned} \tag{4.19}$$

Similarly, one can arrive at the following identities:

$$|\psi^{\mathrm{HF}}\rangle\langle\psi^{\mathrm{HF}}|_1 = \frac{1}{2} \cdot (|\phi_1\rangle\langle\phi_1| + |\phi_1\rangle\langle\phi_1|) = |\phi_1\rangle\langle\phi_1| \tag{4.20a}$$

$$|\psi_{1\alpha}^{2\alpha}\rangle\langle\psi_{1\alpha}^{2\alpha}|_1 = \frac{1}{2} \cdot (|\phi_1\rangle\langle\phi_1| + |\phi_2\rangle\langle\phi_2|) \tag{4.20b}$$

$$|\psi_{1\beta}^{2\beta}\rangle\langle\psi_{1\beta}^{2\beta}|_1 = \frac{1}{2} \cdot (|\phi_1\rangle\langle\phi_1| + |\phi_2\rangle\langle\phi_2|) \tag{4.20c}$$

$$|\psi_{11}^{22}\rangle\langle\psi_{11}^{22}|_1 = |\phi_2\rangle\langle\phi_2| \tag{4.20d}$$

$$|\psi^{\mathrm{HF}}\rangle\langle\psi_{1\beta}^{2\beta}|_1 = \frac{1}{2} \cdot |\phi_1\rangle\langle\phi_2| \tag{4.20e}$$

$$|\psi_{1\alpha}^{2\alpha}\rangle\langle\psi_{11}^{22}|_1 = -\frac{1}{2} \cdot |\phi_1\rangle\langle\phi_2| \tag{4.20f}$$

$$|\psi_{1\beta}^{2\beta}\rangle\langle\psi_{11}^{22}|_1 = \frac{1}{2} \cdot |\phi_1\rangle\langle\phi_2| \tag{4.20g}$$

$$|\psi^{\mathrm{HF}}\rangle\langle\psi_{11}^{22}|_1 = |\psi_{11}^{22}\rangle\langle\psi^{\mathrm{HF}}|_1 = 0 \tag{4.20h}$$

$$|\psi_{1\alpha}^{2\alpha}\rangle\langle\psi_{1\beta}^{2\beta}|_1 = |\psi_{1\beta}^{2\beta}\rangle\langle\psi_{1\alpha}^{2\alpha}|_1 = 0. \tag{4.20i}$$

Substituting using Eqs. (4.19), (4.20), expanding Eq. (4.16), and assuming $\{c_i^\xi\} \in \mathbb{R}$, we get

$$\begin{aligned}
\rho_{nn}^{\mathrm{CI}} = 2 \cdot (|c_n^{\mathrm{HF}}|^2 |\phi_1\rangle\langle\phi_1| &+ \frac{1}{2} \cdot |c_n^{2\alpha1\alpha}|^2 (|\phi_1\rangle\langle\phi_1| + |\phi_2\rangle\langle\phi_2|) \\
&+ \frac{1}{2} \cdot |c_n^{2\beta1\beta}|^2 (|\phi_1\rangle\langle\phi_1| + |\phi_2\rangle\langle\phi_2|) + |c_n^{2211}|^2 |\phi_2\rangle\langle\phi_2| \\
&+ \frac{1}{2} \cdot c_n^{\mathrm{HF}} c_n^{2\alpha1\alpha} [|\phi_1\rangle\langle\phi_2| + \mathrm{c.c.}] \\
&- \frac{1}{2} \cdot c_n^{\mathrm{HF}} c_n^{2\beta1\beta} [|\phi_1\rangle\langle\phi_2| + \mathrm{c.c.}] \\
&- \frac{1}{2} \cdot c_n^{2\alpha1\alpha} c_n^{2211} [|\phi_1\rangle\langle\phi_2| + \mathrm{c.c.}] \\
&+ \frac{1}{2} \cdot c_n^{2\beta1\beta} c_n^{2211} [|\phi_1\rangle\langle\phi_2| + \mathrm{c.c.}]).
\end{aligned} \tag{4.21}$$

Using Eqs. (4.3) and (4.15a), we can write down the following expression for $\mathrm{P}_{\mathrm{AO}}^{nn,\mathrm{CI}}$ in terms of MO-coefficient vectors:

$$\begin{aligned}
\mathrm{P}_{\mathrm{AO}}^{nn,\mathrm{CI}} = 2 \cdot (|c_n^{\mathrm{HF}}|^2 (\mathcal{C}_1^\dagger \mathcal{C}_1) &+ \frac{1}{2} \cdot |c_n^{2\alpha1\alpha}|^2 (\mathcal{C}_1^\dagger \mathcal{C}_1 + \mathcal{C}_2^\dagger \mathcal{C}_2) \\
&+ \frac{1}{2} \cdot |c_n^{2\beta1\beta}|^2 (\mathcal{C}_1^\dagger \mathcal{C}_1 + \mathcal{C}_2^\dagger \mathcal{C}_2) + |c_n^{2211}|^2 (\mathcal{C}_2^\dagger \mathcal{C}_2) \\
&+ \frac{1}{2} \cdot c_n^{\mathrm{HF}} c_n^{2\alpha1\alpha} [\mathcal{C}_1^\dagger \mathcal{C}_2 + \mathcal{C}_2^\dagger \mathcal{C}_1] \\
&- \frac{1}{2} \cdot c_n^{\mathrm{HF}} c_n^{2\beta1\beta} [\mathcal{C}_1^\dagger \mathcal{C}_2 + \mathcal{C}_2^\dagger \mathcal{C}_1] \\
&- \frac{1}{2} \cdot c_n^{2\alpha1\alpha} c_n^{2211} [\mathcal{C}_1^\dagger \mathcal{C}_2 + \mathcal{C}_2^\dagger \mathcal{C}_1] \\
&+ \frac{1}{2} \cdot c_n^{2\beta1\beta} c_n^{2211} [\mathcal{C}_1^\dagger \mathcal{C}_2 + \mathcal{C}_2^\dagger \mathcal{C}_1]).
\end{aligned} \tag{4.22}$$

We obtain the transition density-matrices in a similar manner:

$$\begin{aligned}
\mathrm{P}_{\mathrm{AO}}^{mn,\mathrm{CI}} = c_m^{\mathrm{HF}} c_n^{\mathrm{HF}} (\mathcal{C}_1^\dagger \mathcal{C}_1) &+ \frac{1}{2} \cdot c_m^{2\alpha1\alpha} c_n^{2\alpha1\alpha} (\mathcal{C}_1^\dagger \mathcal{C}_1 + \mathcal{C}_2^\dagger \mathcal{C}_2) \\
&+ \frac{1}{2} \cdot c_m^{2\beta1\beta} c_n^{2\beta1\beta} (\mathcal{C}_1^\dagger \mathcal{C}_1 + \mathcal{C}_2^\dagger \mathcal{C}_2) + c_m^{2211} c_n^{2211} (\mathcal{C}_2^\dagger \mathcal{C}_2) \\
&+ \frac{1}{2} \cdot [c_m^{\mathrm{HF}} c_n^{2\alpha1\alpha} \mathcal{C}_1^\dagger \mathcal{C}_2 + c_m^{2\alpha1\alpha} c_n^{\mathrm{HF}} \mathcal{C}_2^\dagger \mathcal{C}_1] \\
&- \frac{1}{2} \cdot [c_m^{\mathrm{HF}} c_n^{2\beta1\beta} \mathcal{C}_1^\dagger \mathcal{C}_2 + c_m^{2\beta1\beta} c_n^{\mathrm{HF}} \mathcal{C}_2^\dagger \mathcal{C}_1] \\
&- \frac{1}{2} \cdot [c_m^{2\alpha1\alpha} c_n^{2211} \mathcal{C}_1^\dagger \mathcal{C}_2 + c_m^{2211} c_n^{2\alpha1\alpha} \mathcal{C}_2^\dagger \mathcal{C}_1] \\
&+ \frac{1}{2} \cdot [c_m^{2\beta1\beta} c_n^{2211} \mathcal{C}_1^\dagger \mathcal{C}_2 + c_m^{2211} c_n^{2\beta1\beta} \mathcal{C}_2^\dagger \mathcal{C}_1].
\end{aligned} \tag{4.23}$$

4.3.3 TDCI: 1-RDM of an evolving system, $\Psi(t)$

The time-dependent 1-RD of the system is obtained from the total wave function propagated using the time-dependent configuration-interaction (TDCI) method. For a 2-electron system it is given by:

$$\begin{aligned}\rho(\vec{r}_1,t) &= 2\cdot\int_\tau d\sigma_1\cdot d\mathbf{x}_2\cdot|\Psi\rangle\langle\Psi|(\mathbf{x}_1,\mathbf{x}_2,t)\\ &= 2\cdot|\Psi\rangle\langle\Psi|_1(t).\end{aligned} \tag{4.24}$$

$|\Psi\rangle(\mathbf{x}_1,\mathbf{x}_2,t)$ is expressed in terms of the CI wave functions, $\{|\Psi_n^{\mathrm{CI}}\rangle\}$, as a linear superposition:

$$|\Psi\rangle(\mathbf{x}_1,\mathbf{x}_2,t) = \sum_n^{\text{CI states}} a_n(t)\cdot|\Psi_n^{\mathrm{CI}}\rangle(\mathbf{x}_1,\mathbf{x}_2,t). \tag{4.25}$$

Here, $\{a_n(t)\}$ is a set of time-dependent coefficients, and $|\Psi_n^{\mathrm{CI}}\rangle$ is the wave function for the stationary CI state n. The equation of motion for $\{a_n(t)\}$ is given by[11]:

$$i\cdot\frac{\partial a_n(t)}{\partial t} = \sum_m\langle\Psi_n^{\mathrm{CI}}|\hat{\mathcal{H}}|\Psi_m^{\mathrm{CI}}\rangle a_m(t). \tag{4.26}$$

Upon expansion of the expression for $\rho(\vec{r}_1,t)$ in terms of the CI densities, two kinds of terms are obtained:

$$\rho(\vec{r}_1,t) = \rho^{\mathrm{diag}}(\vec{r}_1,t) + \rho^{\mathrm{off}}(\vec{r}_1,t) + \rho^{\mathrm{off}}(\vec{r}_1,t)^\dagger. \tag{4.27}$$

where

$$\begin{aligned}\rho^{\mathrm{diag}}(\vec{r}_1,t) &= 2\cdot\sum_n^{\text{CI states}}|a_n(t)|^2\cdot|\Psi_n^{\mathrm{CI}}\rangle\langle\Psi_n^{\mathrm{CI}}|_1\\ &= \sum_n|a_n(t)|^2\cdot\rho_{nn}^{\mathrm{CI}}.\end{aligned} \tag{4.28a}$$

$$\begin{aligned}\rho^{\mathrm{off}}(\vec{r}_1,t) &= 2\cdot\sum_{m<n}^{\text{CI states}}(a_m(t)\cdot a_n^*(t))\cdot|\Psi_m^{\mathrm{CI}}\rangle\langle\Psi_n^{\mathrm{CI}}|_1\\ &= \sum_{m<n}^{\text{CI states}}(a_m(t)\cdot a_n^*(t))\cdot\rho_{mn}^{\mathrm{CI}}.\end{aligned} \tag{4.28b}$$

Thus, we obtain our one-electron density-matrix for the evolving system using the above expressions, and Eqs. (4.15a), (4.15b):

$$\begin{aligned}\mathrm{P}_{\mathrm{AO},\alpha}^{\mathrm{TDCI}}(t) = \sum_{n} |a_n(t)|^2 \cdot \mathrm{P}_{\mathrm{AO},\alpha}^{nn,\mathrm{CI}} + \sum_{m<n} (a_m(t) \cdot a_n^*(t)) \cdot \mathrm{P}_{\mathrm{AO},\alpha}^{mn,\mathrm{CI}} \\ + \sum_{m<n} (a_n(t) \cdot a_m^*(t)) \cdot \mathrm{P}_{\mathrm{AO},\alpha}^{mn,\mathrm{CI}\dagger}.\end{aligned} \tag{4.29}$$

In Eq. (4.29), we have used the direct integration of the TDCI wave function over all but one of the electronic spatial variables to obtain the 1-RD and the corresponding density-matrix.

4.4 Measuring memory

The TDCI wave function satisfies the TDSE (see Eq. (1.16), Appendix C). It can be shown that the matrix form of this equation satisfies the Liouville-von Neumann equation in the CI basis. Defining the TDCI matrix as $\mathrm{P}(t) = \vec{a}(t)\vec{a}^\dagger(t)$ (see Appendix C), taking the time derivative of the density-matrix in the CI basis, and using Eq. (1.15) gives:

$$\begin{aligned} i\frac{\partial}{\partial t}\mathrm{P}(t) &= \frac{\partial}{\partial t}(\vec{a}(t)\vec{a}^\dagger(t)) \\ &= i\frac{\partial \vec{a}(t)}{\partial t}\vec{a}^\dagger(t) + \vec{a}(t) i \frac{\partial \vec{a}^\dagger(t)}{\partial t} \\ &= \mathrm{H}_e(t)\vec{a}(t)\vec{a}^\dagger(t) - \vec{a}(t)\vec{a}^\dagger(t)\mathrm{H}_e(t) \\ &= \left[\mathrm{H}_e(t), \mathrm{P}(t)\right]. \end{aligned}$$

Thus, provided we know the CI basis Hamiltonian, $\mathrm{H}_e(t)$, we can employ a unitary propagation method on the *full*, CI basis density-matrix, $\mathrm{P}(t)$, to get the TDCI-propagated trajectory.

It has been shown in the preceding section that the time-dependent 1-RDM can be evaluated in terms of the 1-RDMs between stationary CI states, and $\mathrm{P}(t)$:

$$\mathrm{P}_{ab,\mathrm{AO}}^{\mathrm{CI}}(t) = \sum_{m,n} \mathrm{P}_{mn}(t)\mathrm{B}_{mnab,\mathrm{AO}}. \tag{4.30}$$

Here B is a 4-tensor comprised of AO basis density-matrix elements for the density-matrix between CI states m and n. We can represent quantities in Eq. (4.30) as a matrix equation by vectorizing $\mathrm{P}_{\mathrm{AO}}^{\mathrm{CI}}(t)$ as $\mathrm{vec}(\mathrm{P}_{\mathrm{AO}})(t)$ ($N^2 \times 1$, N being the number of AO basis functions) and $\mathrm{P}(t)$ as $\mathrm{vec}(\mathrm{P})(t)$ ($M^2 \times 1$, M being the number of CI states), and representing B as a matrix $\tilde{B}$ ($N^2 \times M^2$). Then Eq. (4.30) becomes:

$$\tilde{\mathrm{B}}^T \mathrm{vec}(\mathrm{P})(t) = \mathrm{vec}(\mathrm{P}_{\mathrm{AO}})(t). \tag{4.31}$$

The goal here is to solve for $\mathrm{vec}(\mathrm{P})(t)$ given $\mathrm{vec}(\mathrm{P}_{\mathrm{AO}})(t)$. However, Eq. (4.31) is an underdetermined linear equation as $\tilde{\mathrm{B}}$ has more columns than rows, owing to the general case where a reasonably accurate CI method has many more stationary states than one-body basis functions (alternatively, linear dependencies between the rows or columns of $\tilde{\mathrm{B}}$ may also yield it rank deficient). One way to solve this linear system of equations is to add rows to $\tilde{\mathrm{B}}$ and use past 1-RDMs:

$$\begin{bmatrix} \tilde{\mathrm{B}}^T \\ \mathcal{B}_1 \\ \vdots \\ \mathcal{B}_l \end{bmatrix} \mathrm{vec}(\mathrm{P})(t) = \begin{bmatrix} \mathrm{vec}(\mathrm{P}_{\mathrm{AO}})(t) \\ \mathrm{vec}(\mathrm{P}_{\mathrm{AO}})(t-\Delta t) \\ \vdots \\ \mathrm{vec}(\mathrm{P}_{\mathrm{AO}})(t-l\Delta t) \end{bmatrix}. \tag{4.32}$$

If we call the block matrix on the left-most side M, then for sufficiently large l, M will have more rows than columns. We can form the Moore-Penrose pseudoinverse matrix of M:

$$\mathrm{M}^+ = (\mathrm{M}^\dagger \mathrm{M})^{-1} \mathrm{M}^\dagger. \tag{4.33}$$

M^+ is the left inverse of M. Multiplying both sides by M^+ transforms Eq. (4.32) to

$$\mathrm{vec}(\mathrm{P})(t) = \mathrm{M}^+ \begin{bmatrix} \mathrm{vec}(\mathrm{P}_{\mathrm{AO}})(t) \\ \mathrm{vec}(\mathrm{P}_{\mathrm{AO}})(t-\Delta t) \\ \vdots \\ \mathrm{vec}(\mathrm{P}_{\mathrm{AO}})(t-l\Delta t) \end{bmatrix}. \tag{4.34}$$

Thus, given the current and past 1-RDMs and the TDCI Hamiltonian (comprised of a diagonal matrix containing eigenvalues of the stationary CI states and a CI basis dipole moment matrix-dependent field term), there is a way to form $\mathrm{P}(t)$, propagate it forward, and then calculate the next 1-RDM in the AO basis.

To form M, we first evaluate Eq. (4.34) at time $(t - \Delta t)$:

$$\tilde{\mathrm{B}}^T \mathrm{vec}(\mathrm{P})(t - \Delta t) = \mathrm{vec}(\mathrm{P}_{\mathrm{AO}})(t - \Delta t). \tag{4.35}$$

We know that $\mathrm{vec}(\mathrm{P})(t-\Delta t)$ is related to $\mathrm{vec}(\mathrm{P})(t)$ via the solution of the Liouville-von Neumann equation:

$$\begin{aligned} \mathrm{P}(t) &= \exp\left(-i\mathrm{H}_e(t - \Delta t)\Delta t\right)\mathrm{P}(t - \Delta t)\exp\left(i\mathrm{H}_e(t - \Delta t)\Delta t\right); \\ \mathrm{P}(t - \Delta t) &= \exp\left(i\mathrm{H}_e(t - \Delta t)\Delta t\right)\mathrm{P}(t)\exp\left(-i\mathrm{H}_e(t - \Delta t)\Delta t\right). \end{aligned} \tag{4.36}$$

Vectorizing Eq. (4.36) gives

$$\mathrm{vec}(\mathrm{P})(t - \Delta t) = (\exp\left(-i\mathrm{H}_e(t - \Delta t)\Delta t\right)^T \otimes \exp\left(i\mathrm{H}_e(t - \Delta t)\Delta t\right))\mathrm{vec}(\mathrm{P})(t).$$

where $\otimes$ denotes the Kronecker product of matrices. In conjunction with Eq. (4.35), we get

$$\tilde{\mathrm{B}}^T(\exp\left(-i\mathrm{H}_e(t - \Delta t)\Delta t\right)^T \otimes \exp\left(i\mathrm{H}_e(t - \Delta t)\Delta t\right))\mathrm{vec}(\mathrm{P})(t) = \mathrm{vec}(\mathrm{P}_{\mathrm{AO}})(t - \Delta t).$$

We can define $\mathcal{B}_1$ as

$$\mathcal{B}_1 = \tilde{\mathrm{B}}^T(\exp\left(-i\mathrm{H}_e(t - \Delta t)\Delta t\right)^T \otimes \exp\left(i\mathrm{H}_e(t - \Delta t)\Delta t\right)).$$

Going back j timesteps gives us:

$$\mathcal{B}_j = \tilde{\mathrm{B}}^T(\mathrm{C}_j^T \otimes \mathrm{A}_j)$$

where

$$\begin{aligned} \mathrm{C}_j &= \exp\left(-i\mathrm{H}_e(t - \Delta t)\Delta t\right)\exp\left(-i\mathrm{H}_e(t - 2\Delta t)\Delta t\right)\ldots\exp\left(-i\mathrm{H}_e(t - j\Delta t)\Delta t\right), \\ \mathrm{A}_j &= \exp\left(i\mathrm{H}_e(t - j\Delta t)\Delta t\right)\exp\left(i\mathrm{H}_e(t - (j-1)\Delta t)\Delta t\right)\ldots\exp\left(i\mathrm{H}_e(t - \Delta t)\Delta t\right). \end{aligned}$$

Thus, matrix M can be built as

$$\mathrm{M} = \begin{bmatrix} \tilde{\mathrm{B}}^T \\ \tilde{\mathrm{B}}^T(\mathrm{C}_1^T \otimes \mathrm{A}_1) \\ \vdots \\ \tilde{\mathrm{B}}^T(\mathrm{C}_l^T \otimes \mathrm{A}_l)) \end{bmatrix}. \tag{4.37}$$

Once the TDCI density-matrix is built it can be propagated one step ahead in time using Eq. (4.36), from t to $(t + \Delta t)$. The TDCI Hamiltonian, $\mathrm{H}_e(t)$, is the sum of a diagonal matrix with the eigenvalues of the stationary CI states, and a field-term, consisting of the electric-field vector dotted with the respective CI dipole moment matrix (see Appendix C).

The minimum value of l that achieves accurate propagation compared to the TDCI density-matrix trajectory is considered to be a metric for the amount of history dependence in the system. This value is expected to change for different CI ansatzes, and possibly for cases where the adiabatic approximation in RT-TDDFT is expected to fail (i.e. resonantly driven electron dynamics).

4.5 Preliminary results

Using the method to reconstruct the full TDCI density-matrix in the CI basis described in the preceding section, the memory content of TDCIS propagation is measured in terms of the number of previous time-steps needed to propagate the systems accurately with respect to the TDCIS propagation, termed "memory-steps". Molecules examined in the present study include HeH^+, H_2 (using two basis sets each, STO-3G and 6-31G), and LiH using the STO-3G basis set. The dependence on field-frequency of the memory-steps is tested, while fixing other field-parameters: field-strength, fixed at 0.5 a.u., and duration of applied sinusoidal field, fixed at 5 cycles. The frequencies chosen for this analysis are 0.1, 0.3, 0.5, 0.7, 0.9, 1.1, 1.3, 1.5, 1.7 1.9 and 2.1 a.u.. For LiH, as only 0.1 a.u. is reasonably close to being near-resonant, we additionally perform calculations for resonant (0.17 a.u.), half of the resonant ("offresonant_low", 0.085 a.u. a.u.) and double the resonant ("offresonant_high", 0.34 a.u.) frequencies.

4.5.1 H_2, HeH^+

For H_2 and HeH^+ in the case of a restricted reference, the dimensions of the 1-RDM are equal to the dimensions of the CIS basis (which consists of the Hartree-Fock ground-state wave function and excited states formed from singly substituted

Slater determinants). Therefore the number of memory-steps, l, is not expected to be high.[3] This is seen for both the STO-3G (which has one singlet excited state each) and the 6-31G (which has three singlet excited states each) basis sets, for all the frequency regimes. This is seen for the STO-3G basis set in Figs. 4.2 and 4.3 where the results for near-resonant perturbations are plotted, and the results are identical for TDCIS/6-31G.

---

[3] for $l = 0$, even when the dimensions of the density-matrices in the two different bases, CIS and AO, agree, the propagation error is observed to be multiple orders of magnitude higher in error. This implies that the matrix M is rank deficient and l needs to be at least equal to 1.

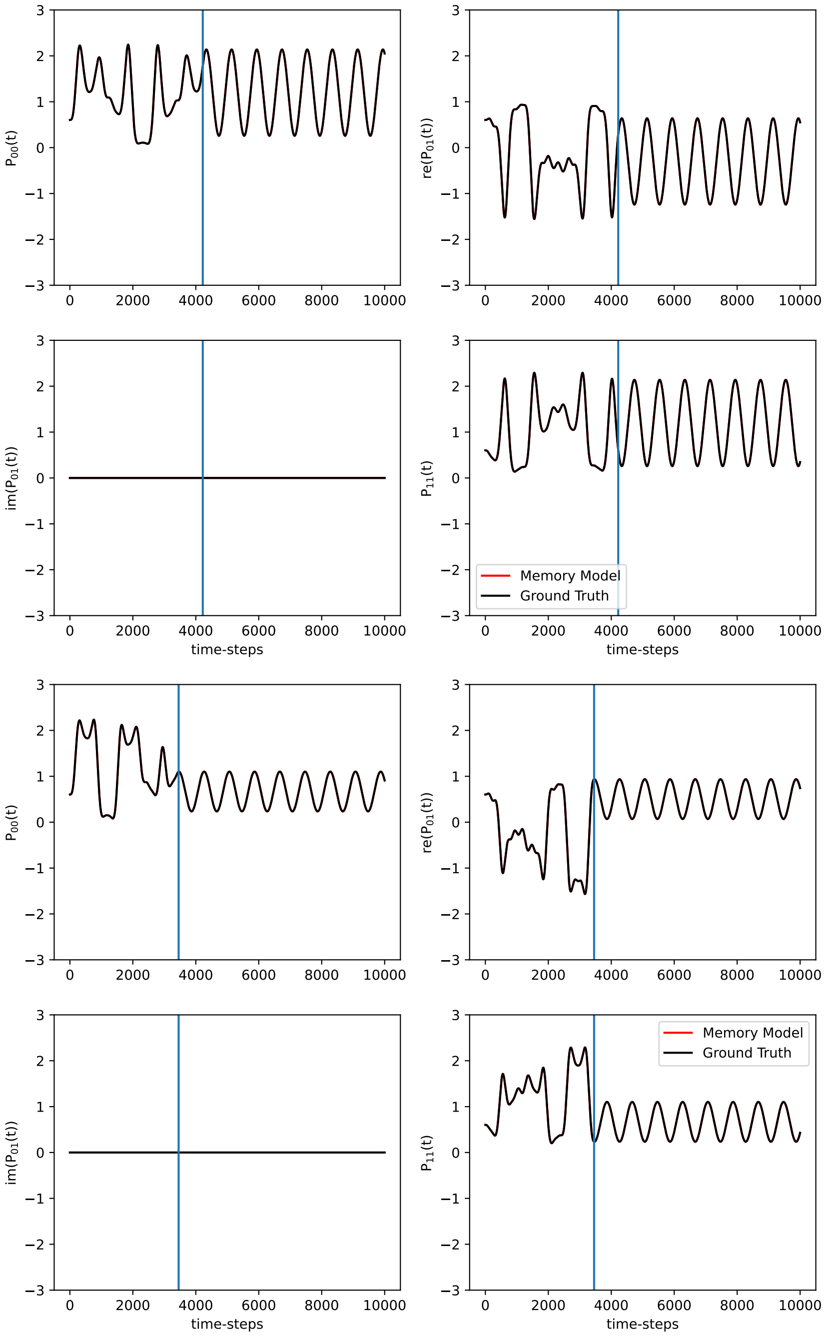

Figure 4.2: Time-dependent density-matrix elements plotted for H_2 (with the STO-3G basis set), perturbed from a Hartree-Fock ground state with field-frequencies of 0.9 a.u. (top four panels) and 1.1 a.u. (bottom four panels), field-strength of 0.5 a.u. and a duration of 5 sinusoidal cycles. The amount of previous AO basis 1-RDMs used to build the TDCIS density-matrices is 1 yet yields highly accurate TDCIS propagation.

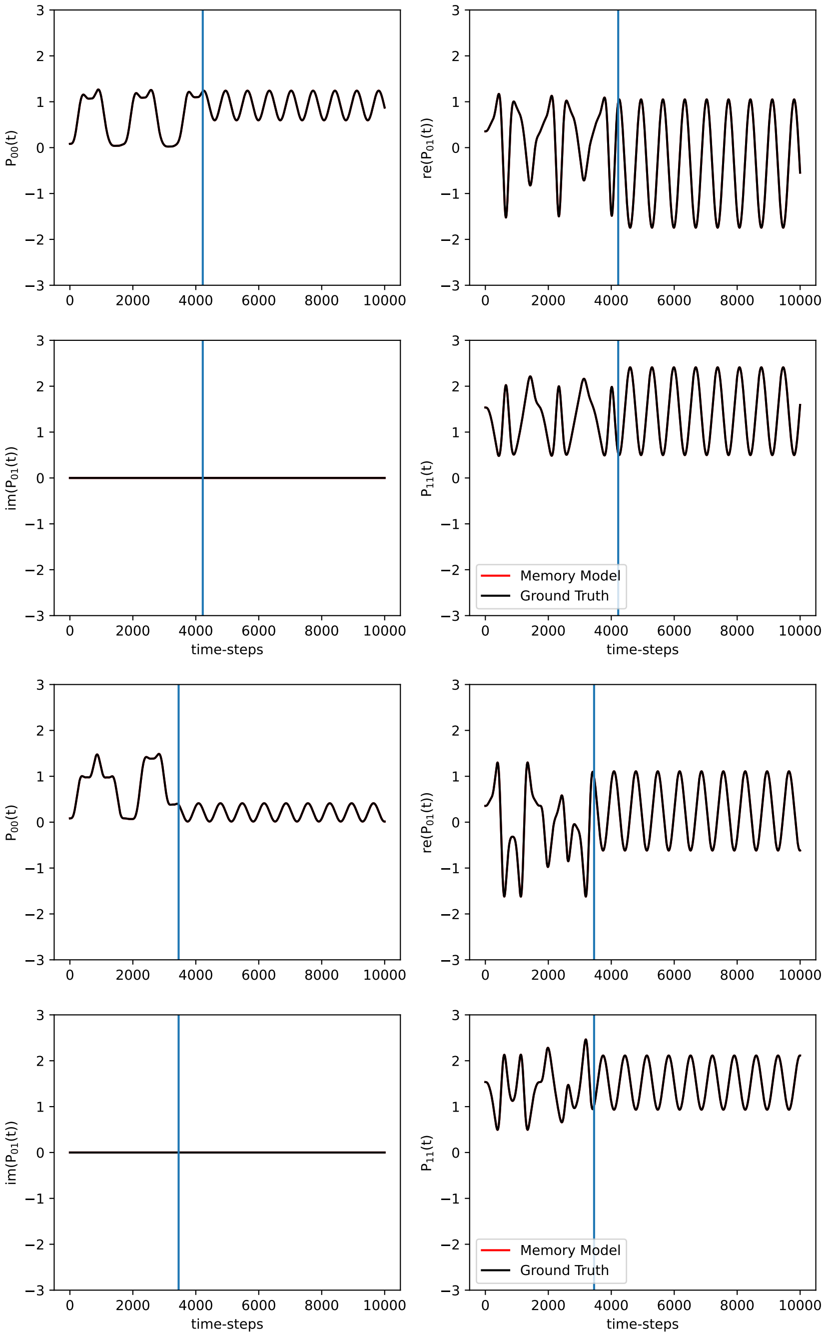

Figure 4.3: Time-dependent density-matrix elements plotted for HeH^+ (with the STO-3G basis set), perturbed from a Hartree-Fock ground state with field-frequencies of 0.9 a.u. (top four panels) and 1.1 a.u. (bottom four panels), field-strength of 0.5 a.u. and a duration of 5 sinusoidal cycles. The amount of previous AO basis 1-RDMs used to build the TDCIS density-matrices is 1 yet yields highly accurate TDCIS propagation like in the H_2 case.

In contrast, for TDCASSCF(2,2), the history-dependence of propagation error increases dramatically in comparison to TDCIS for H_2 and HeH^+ molecules with the STO-3G basis set. CASSCF contains more than singly-substituted Slater determinants (in this case, one spin-adapted singly- and one doubly-substituted determinant) and thus allows for determination of more stationary states (two singlet excited states in total in addition to the ground state), making the dimensions of the density-matrix in the CASSCF basis bigger than those of the density-matrix in the CIS basis.

To demonstrate and contrast the history-dependence of TDCASSCF vs TDCIS, a plot of mean-squared propagation error between ground-truth and predicted density-matrices, averaged over the matrix elements, vs memory-steps is presented in Fig. 4.4 for H_2 and Fig. 4.5 for HeH^+. The CASSCF method includes electronic correlation in the ground state compared to the CIS method, which has no correlation in the ground state. This is due to the inclusion of the doubly-substituted Slater determinant in the manifold of determinants used in linear combinations to describe the wave functions of the stationary states of the system.[7] Thus, when a interacting system whose dynamics are governed by the TDCASSCF method is mapped onto a single-reference system of non-interacting electrons (as is done in the Kohn-Sham DFT formalism), the time-dependent Hamiltonian of such a system will include more memory effects into the XC potential than when mapping a system described by TDCIS onto a system of non-interacting electrons described by the Kohn-Sham formalism. This effect is displayed in the increasing history-dependence when going from TDCIS to TDCASSCF, where the AO basis density-matrices, while not single-reference, act as proxy for observing memory effects in a one-particle description of a many-body system of interacting electrons.

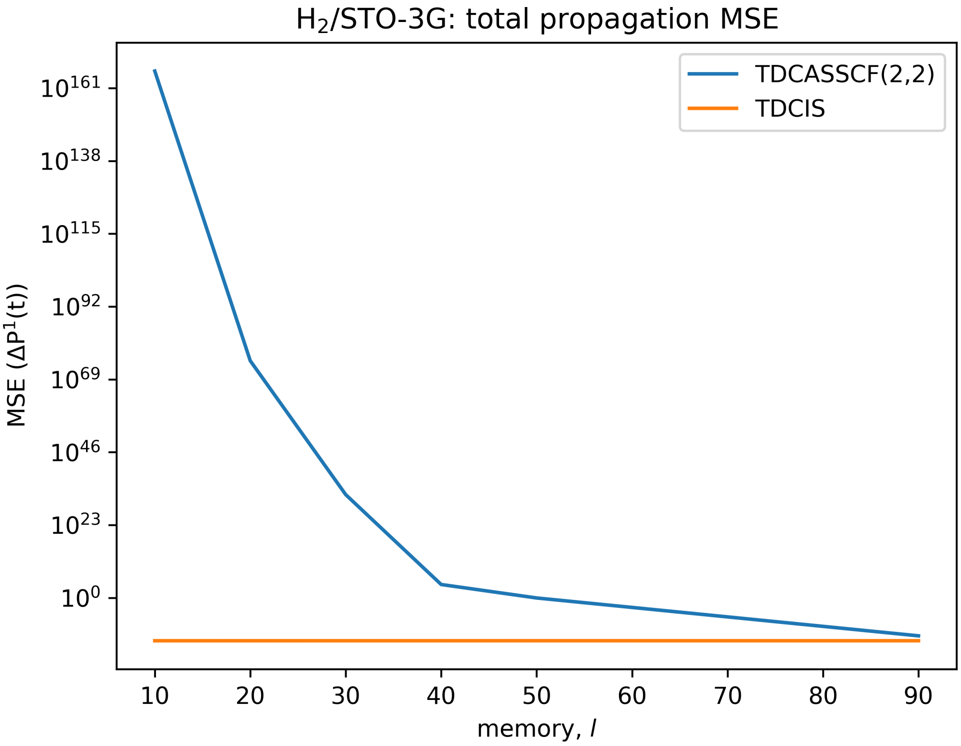

Figure 4.4: Propagation MSE vs memory-steps, plotted for H_2/STO-3G propagation data. The amount of history required, l, is much more in the case of TDCASSCF propagation than in the case of TDCIS propagation to obtain accurate propagation.

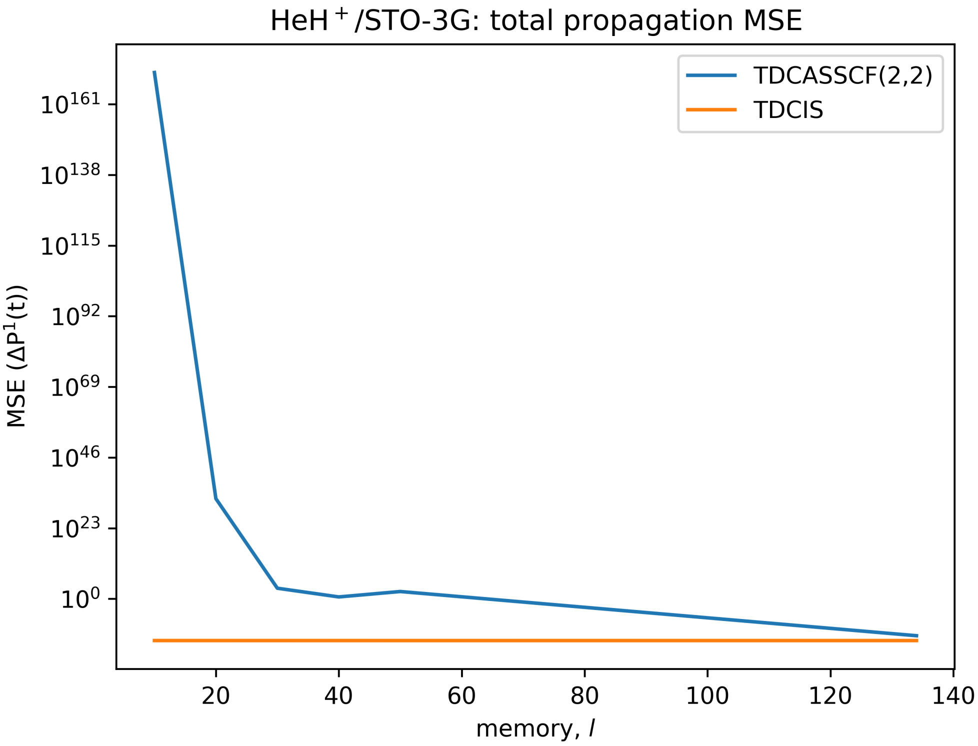

Figure 4.5: Propagation MSE vs memory-steps, plotted for HeH$^+$/STO-3G propagation data. The amount of history required is much more in the case of TDCASSCF propagation than in the case of TDCIS propagation to get a low propagation error, just as for H_2.

4.5.2 LiH

LiH, being a larger system than H_2 and HeH$^+$, has 6 basis functions and 4 electrons. Accordingly, the TDCIS density-matrix in the CIS basis is a 9×9 matrix, whereas the 1-RDM in the STO-3G basis is of size 6×6. The linear system of Eq. (4.31) is thus underdetermined for the LiH/STO-3G system within the TDCIS theory. Consequently, LiH shows more history-dependence relative to H_2 and HeH$^+$ based on the amount of memory-steps required to give accurate propagation using the TDCIS Hamiltonian. This can be attributed primarily to the dimension of the CIS basis, which exceeds the number of one-body basis functions in the STO-3G basis set, while the history also shows some dependence on the field-parameters. For LiH, three further frequencies were tested: the ($S_0 \rightarrow S_1$)

resonant frequency of 0.17 a.u., 0.085 a.u., and 0.34 a.u.. Preliminary analysis (see Fig. 4.6) shows that lower frequency trajectories require much more memory to describe the dynamics with the field on than higher frequency trajectories to give accurate propagation, suggesting frequency-dependence of the amount of memory required to describe electron dynamics accurately.

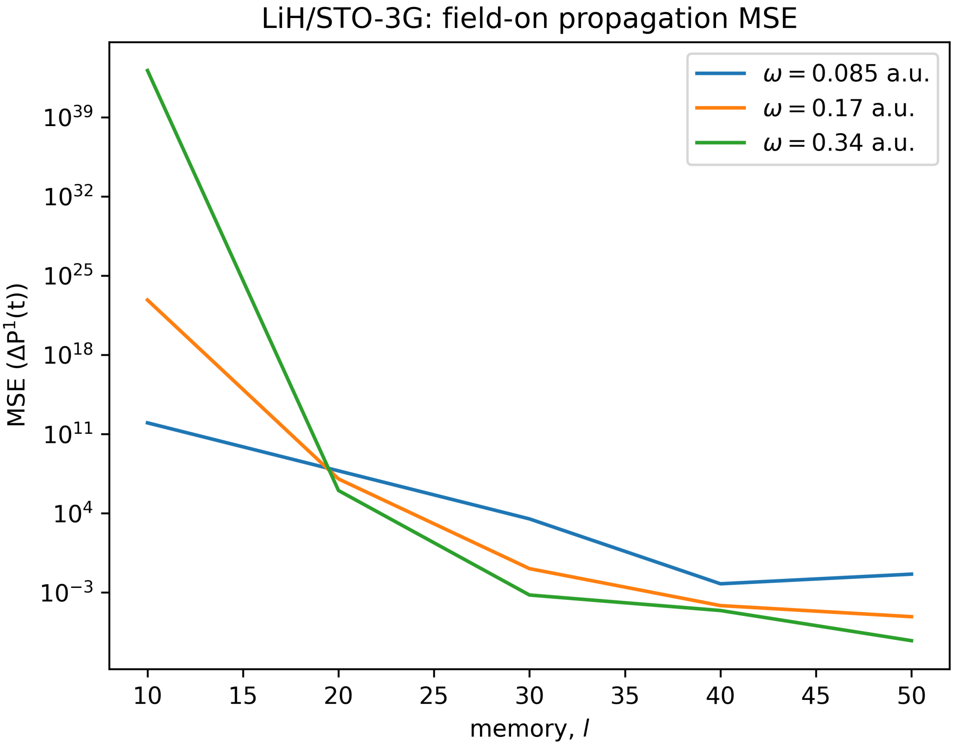

Figure 4.6: History, in previous time-steps, plotted against the mean-squared propagation error (with the field on) with respect to the time-dependent 1-RDM obtained from TDCIS propagation for the LiH/STO-3G system. Low frequency trajectory requires a higher amount of history to get accurate propagation.

To explore the field-frequency and field-amplitude dependence of the history, the total propagation MSEs for different memory-steps were plotted (Figs. 4.7 and 4.8). For exploring the frequency-dependence, a field-amplitude of 0.5 a.u. and duration of 5 field-cycles were chosen, whereas for propagation MSE vs field-amplitude plots a field-frequency of 0.1515 a.u. (near-resonant frequency, $S_0 \rightarrow S_1$ gap being 0.16836 Ha for LiH/STO-3G system at the CIS level of linear response) and field-duration of 5 cycles was chosen. To calculate the propagation MSE, the number of timesteps included in the trajectory with the field switched on, N_{on} is the minimum of either 0.8 fs ($N_{\text{off}} = 4000$ timesteps) or the duration for which the field is turned on ($N_{\text{off}} = (t_{\text{off}}/Deltat)$). A further 10000 timesteps are included with the field turned off.

Fig. 4.7 shows that the general trend is that the propagation error decreases as the number of memory-steps are increased, and the errors tend to decrease as field-frequency increases. While the history of $l = 10$ shows inconsistent results with respect to this trend, showing much better propagation for field-frequencies near 0.25 a.u. and 0.35 a.u., these are still achieved at a higher-than-resonant field-frequencies. Fig. 4.8 illustrates that, when it comes to amplitude-dependence, propagation errors are the least for high-magnitude field-amplitudes in the near-resonant case. It is possible that the field-dependent terms corresponding to the low-amplitude near-resonant applied fields are of a comparable magnitude as the field-independent terms of the Hamiltonian, causing a greater dynamic response in the density-matrix elements than that due to a high-amplitude near-resonant field, where the field-dependent term is expected to dominate the dynamics.

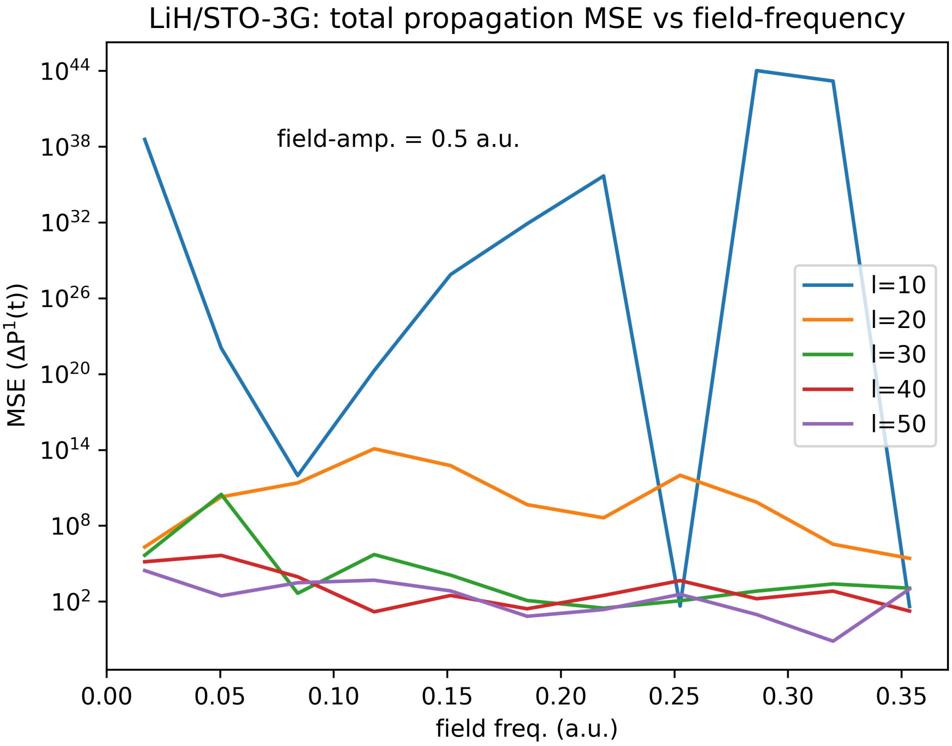

Figure 4.7: Total propagation MSE vs field-frequency, plotted for LiH TDCIS/STO-3G. The field-duration is 5 cycles, the field-amplitude is 0.5 a.u. and the propagation MSE is measured from up to 0.8 fs before the field is turned off (the starting point in the dynamics) to 2 fs after the field is turned off.

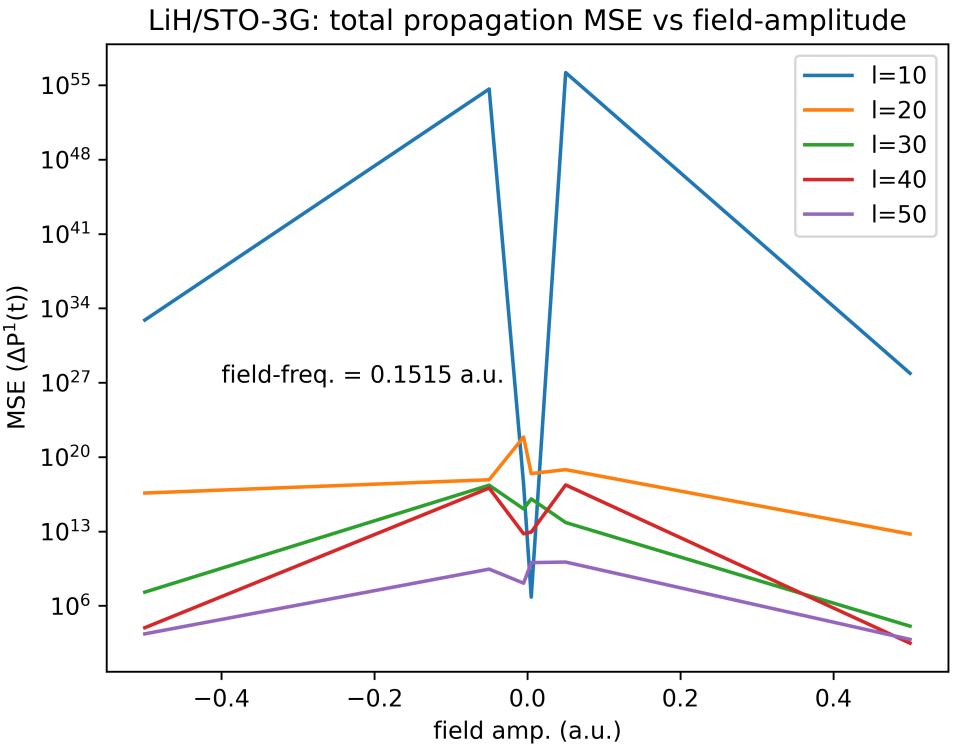

Figure 4.8: Total propagation MSE vs field-amplitude, plotted for LiH TDCIS/STO-3G. The field-duration is 5 cycles, the field-frequency is 0.1515 a.u. and the propagation MSE is measured from up to 0.8 fs before the field is turned off (the starting point in the dynamics) to 2 fs after the field is turned off.

4.6 Future work and outlook

The preliminary results indicate that a history of at least 1 timestep is required to reproduce accurate electron dynamics (and more for larger systems than H_2 and HeH^+). The dependence of history on field-frequency, field-strength, field duration as well as basis set size, which correlates with how much dynamic electron correlation is incorporated into the electronic structure of the chemical system being studied, needs to be explored further for the systems mentioned above, and LiH in particular. Some preliminary findings for the LiH/STO-3G system suggest that lower field-amplitudes require more history to accurately reproduce the 1-RDM dynamics, whereas as field-frequency increases, less history is required for accurate

1-RDM propagation.

This insight will be used together with statistical modeling of the time-dependent Hamiltonian to build better Hamiltonian models that can incorporate history dependence and to help inform construction of better approximated exchange-correlation functionals in the future.

Appendix A

Chapter 2 Supplemental Information

Excited state characterization

Table A.1: Transition energies between S_0, S_1 and S_2 states, calculated using the state-averaged CASSCF (SA-CASSCF) method for Systems 1, 2, and 3.

SA-CASSCF	ΔE (eV)		
	$S_0 \rightarrow S_1$	$S_0 \rightarrow S_2$	$S_1 \rightarrow S_2$
System 1	9.24	13.21	3.97
System 2	7.23	8.41	1.18
System 3	5.92	7.21	1.29

Table A.2: Total state and transition dipole moments calculated using linear response TDHF and CIS methods for Systems 1, 2, and 3.

LR-TDHF	μ (D)			CIS	μ (D)		
	S_0	S_1	$S_0 \rightarrow S_1$		S_0	S_1	$S_0 \rightarrow S_1$
System 1	1.23	2.97	4.18	System 1	1.23	4.02	4.58
System 2	2.04	4.32	6.72	System 2	2.04	5.11	7.34
System 3	2.66	5.50	8.90	System 3	2.66	6.14	9.62

Table A.3: Coefficients indicating the one-particle excitation MO contributions to the $S_0 \rightarrow S_1$ transition, calculated using linear response TDHF and CIS methods for Systems 1, 2, and 3.

LR-TDHF	HOMO → LUMO	HOMO → (LUMO+1)	(HOMO-1) → LUMO	(HOMO-1) → (LUMO+1)
System 1	0.698	0.003	-0.028	0.016
System 2	0.695	0.043	0.002	0.094
System 3	0.690	-0.050	-0.008	-0.122
CIS	HOMO → LUMO	HOMO → (LUMO+1)	(HOMO-1) → LUMO	(HOMO-1) → (LUMO+1)
System 1	0.685	0.011	0.040	0.019
System 2	0.687	0.032	0.035	0.085
System 3	0.685	-0.039	0.015	-0.116

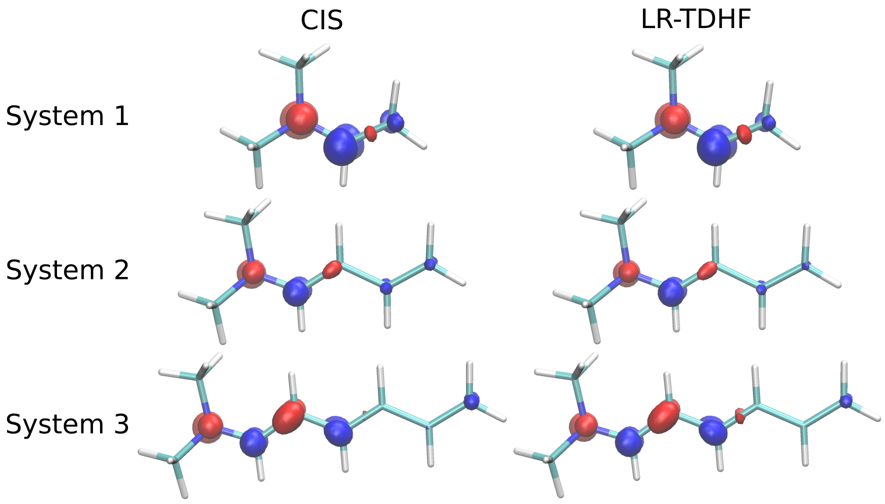

Figure A.1: Isodensity surface plots of density-difference between the S_1 and S_0 states. Isodensity values of ±0.02 (Systems 1, 2) and ±0.01 (System 3) have been chosen to visually emphasize the density-differences. One can see decreased density (red) at the nitrogen-center and increased density (blue) along the π-conjugated carbon-centers.

Table A.4: Molecular geometries: Cartesian coordinates in Å.

System 1

C	0.80047	-0.66509	-0.11827
C	2.00688	-0.11078	0.11778
N	-0.42044	-0.02054	-0.25877
H	0.72728	-1.74301	-0.25651
H	2.88973	-0.74049	0.12699
H	2.15580	0.95118	0.28205
C	-0.46614	1.40700	-0.00277
C	-1.60885	-0.76328	0.13660
H	0.28052	1.91830	-0.61906
H	-0.26928	1.65331	1.05622
H	-1.45497	1.79021	-0.27221
H	-1.76538	-0.76587	1.23004
H	-1.52099	-1.80168	-0.19844
H	-2.49378	-0.32528	-0.33773

System 2

C	0.37660	-0.15531	-0.05180
C	1.50144	0.57537	0.08036
C	-0.97813	0.36227	-0.02032
H	0.47343	-1.23402	-0.19311
H	2.48410	0.11402	0.05261
H	1.46960	1.65440	0.22000
H	-1.09658	1.43430	0.12154
C	-2.06288	-0.44237	-0.16982
H	-1.91028	-1.51513	-0.28397
N	-3.39100	-0.07100	-0.24466
C	-3.73854	1.32029	-0.01837
C	-4.38724	-1.04687	0.17495
H	-3.14914	1.96374	-0.67934
H	-3.55937	1.63523	1.02473
H	-4.79728	1.46829	-0.25026
H	-4.52016	-1.07120	1.27062
H	-4.08484	-2.04527	-0.15574
H	-5.35254	-0.81147	-0.28573

System 3

C	1.55032	-0.08117	-0.02431
C	2.70292	0.61171	0.07626
C	0.22121	0.49275	0.01714
H	1.60138	-1.16488	-0.14791
H	3.66932	0.11769	0.03696
H	2.70907	1.69304	0.20057
H	0.15369	1.57527	0.13999
C	-0.92269	-0.23357	-0.08723
H	0.83280	-1.31531	-0.21347
C	2.26215	0.29895	-0.04219
H	-2.36690	1.37438	0.08325
C	-3.36380	-0.49404	-0.15776
H	-3.22897	-1.57064	-0.25443
N	-4.68396	-0.10246	-0.21462
C	-5.01069	1.29759	-0.01120
C	-5.69630	-1.06006	0.20846
H	-4.42155	1.92079	-0.69152
H	-4.81439	1.62891	1.02333
H	-6.07017	1.45476	-0.23270
H	-5.83394	-1.07142	1.30343
H	-5.40646	-2.06557	-0.11126
H	-6.65587	-0.81510	-0.25893

Electron dynamics

TDCIS propagation

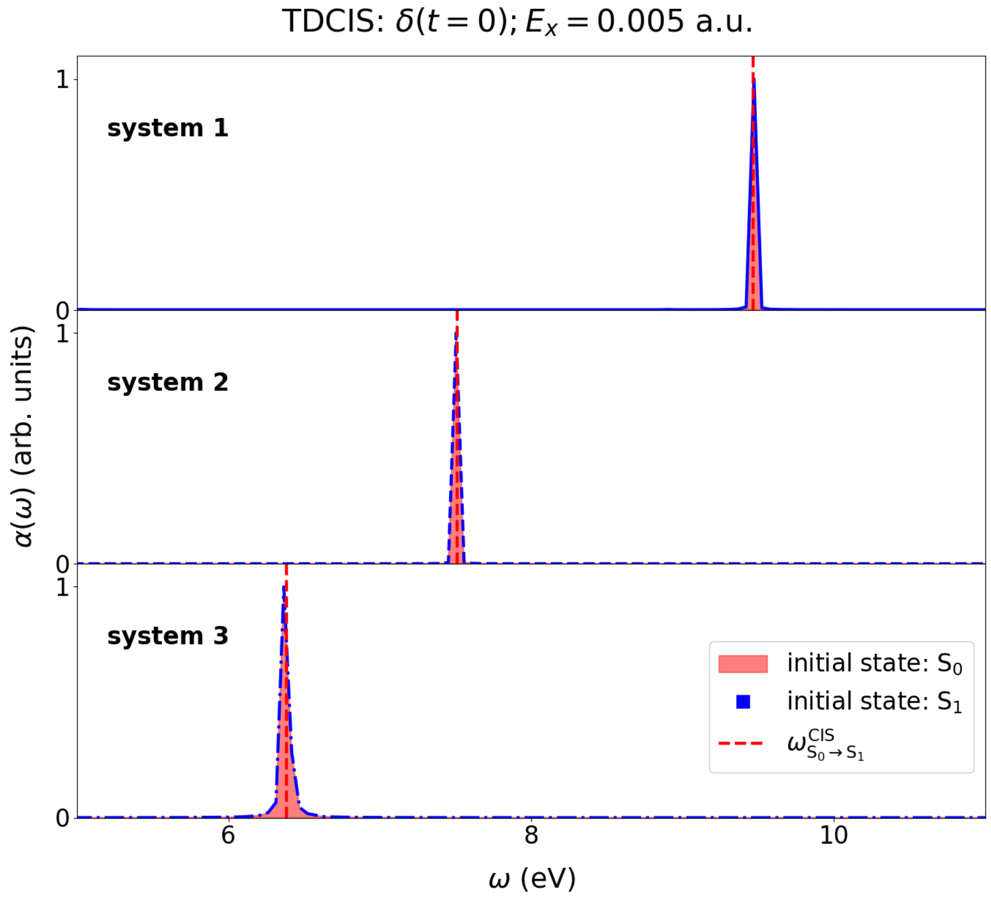

Figure A.2: Linear absorption spectra corresponding to the TDCIS dipole moments obtained with weak (pseudo-)delta-kick perturbations, with the systems starting in states S_0 and S_1 (CIS stationary states). The spectra show prominent peaks at the $S_0 \to S_1$ transition frequency in both cases.

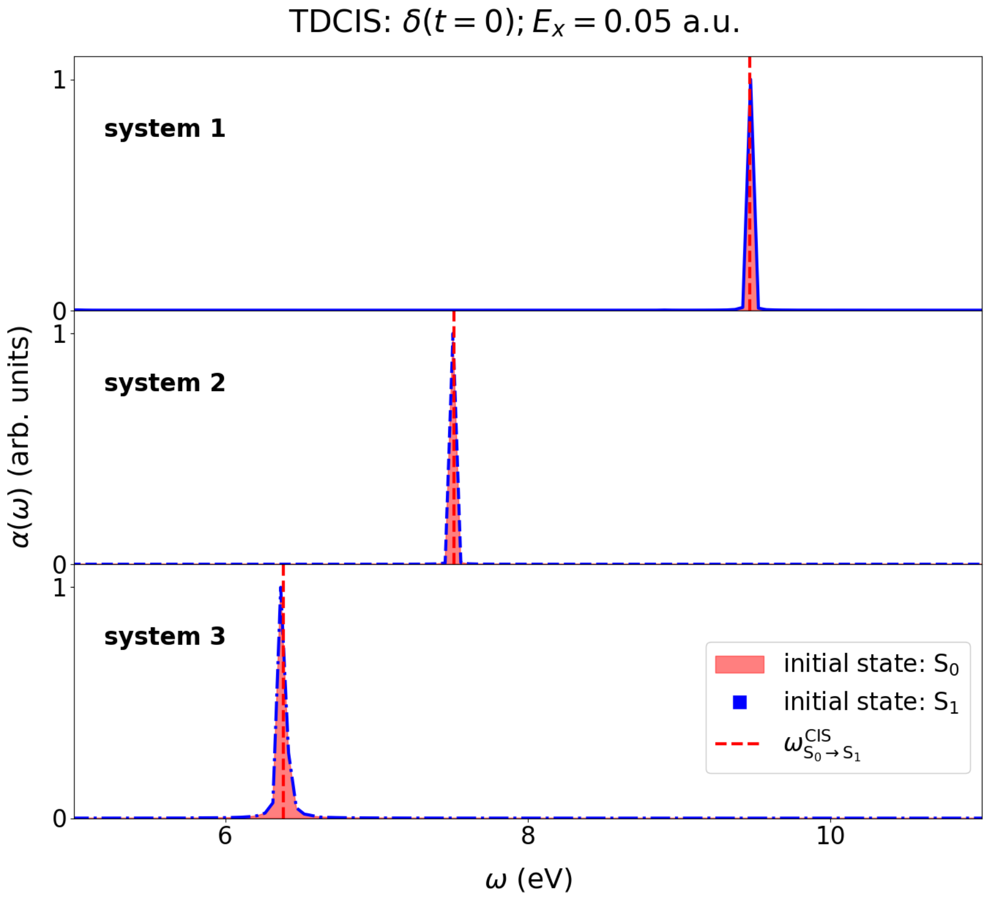

Figure A.3: Linear absorption spectra corresponding to the TDCIS dipole moments obtained with strong (pseudo-)delta-kick perturbations, with the systems starting in states S_0 and S_1 (CIS stationary states). The peaks at the $S_0 \to S_1$ transition frequency remain unshifted as expected.

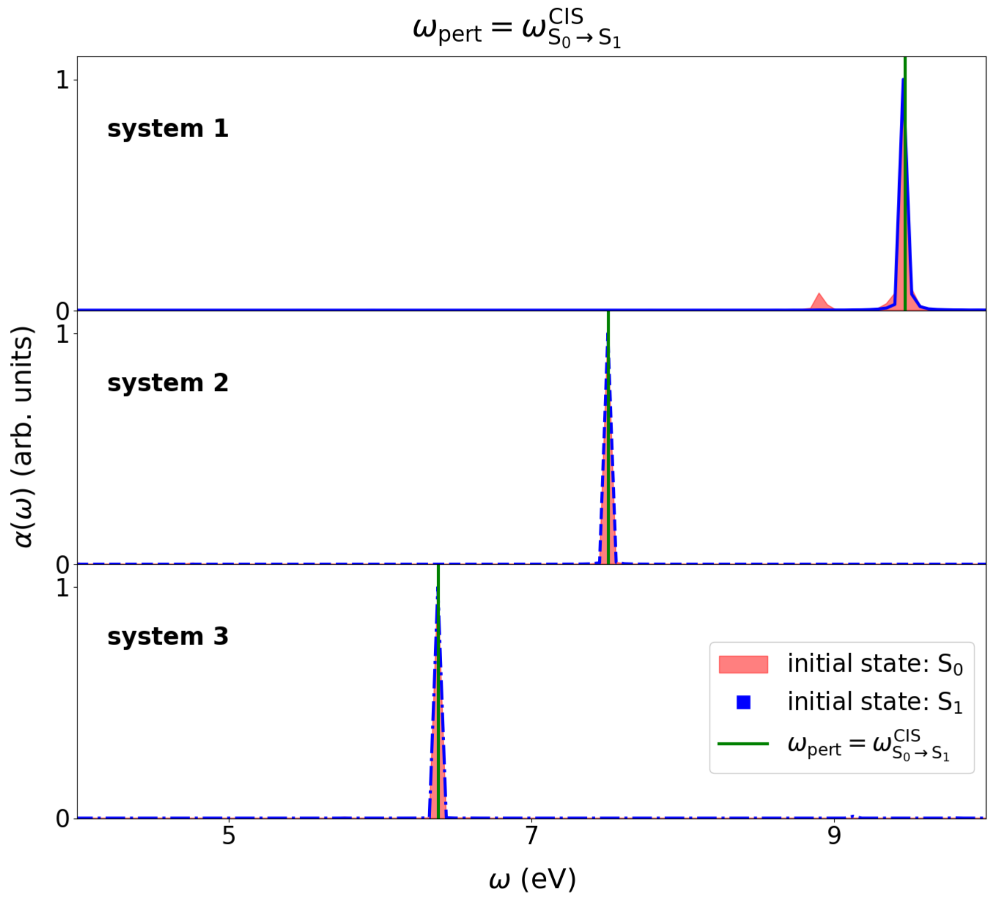

Figure A.4: Linear absorption spectra corresponding to the TDCIS dipole moments obtained with the CIS $S_0 \rightarrow S_1$ transition-resonant field perturbations, with the systems starting in states S_0 and S_1 (CIS stationary states). The spectra show prominent peaks at the field frequency in both cases.

Real-time TDHF propagation

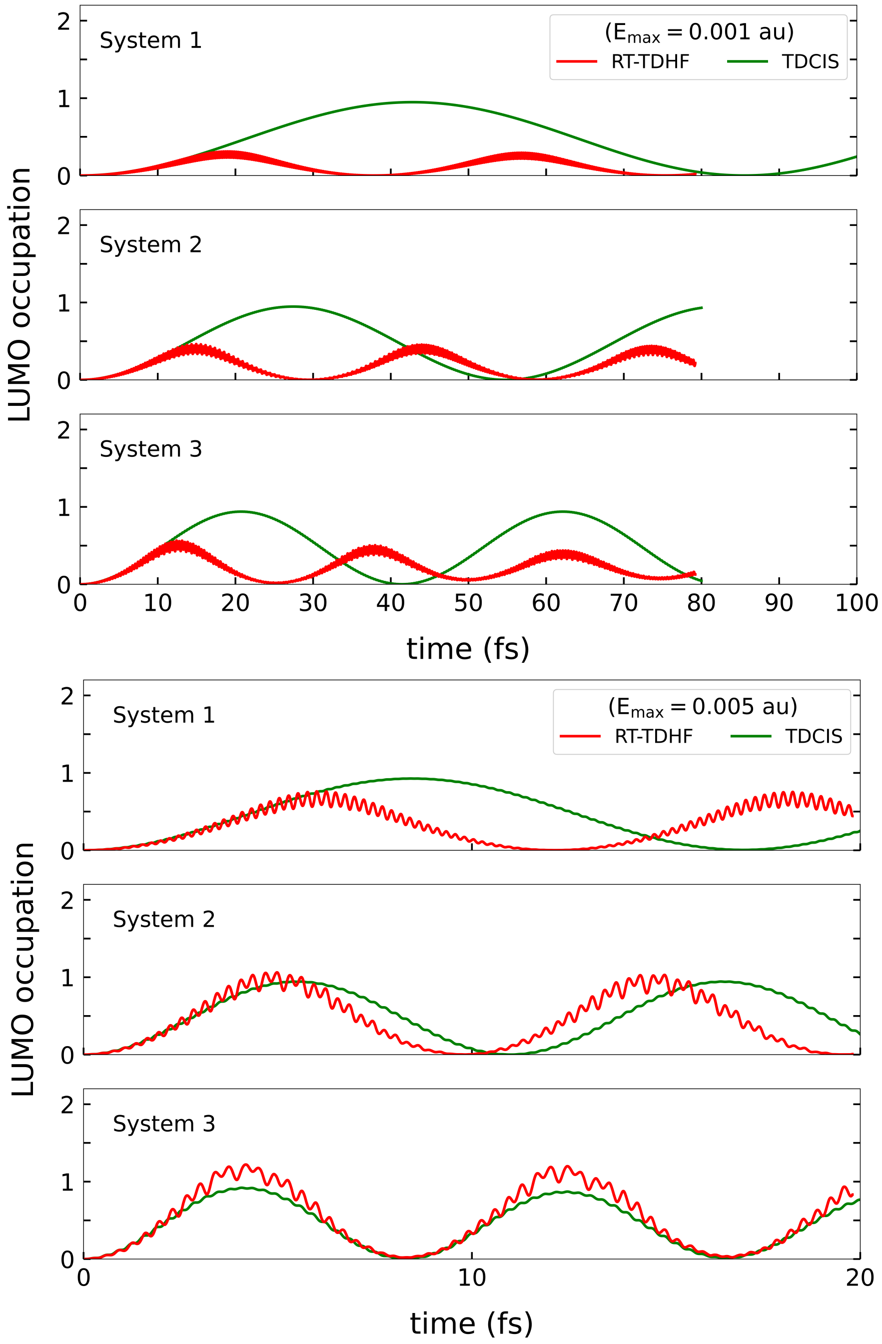

Figure A.5: Time-dependent LUMO occupations for Systems 1-3 with the field turned on, with $S_0 \rightarrow S_1$ transition (LR-TDHF) resonant field-frequencies and field-amplitudes of 0.001 a.u. (top) and 0.005 a.u. (bottom).

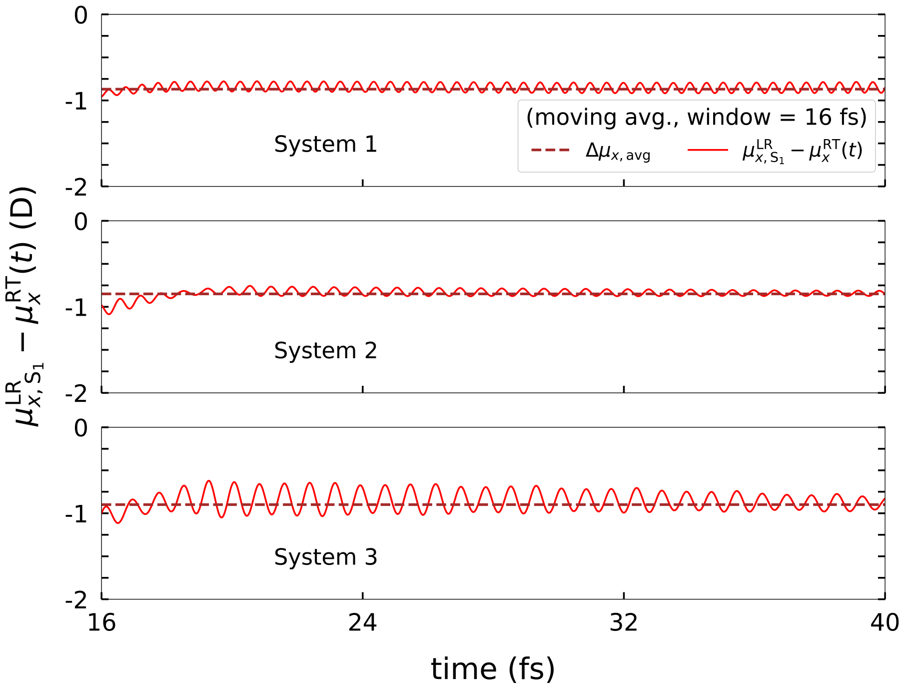

Figure A.6: Moving averaged time-dependent dipole difference, between the linear response TDHF and real-time TDHF dipole moment values of the S_1 state, plotted as a function of time for $\mathrm{S}_0 \to \mathrm{S}_1$ excitation. These values are used to estimate the final average values of the real-time TDHF S_1 dipole moments to quantify charge transfer. The average RT-TDHF dipole moment is calculated as $\Delta\mu_{x,\mathrm{avg}} + \mu^{\mathrm{HF}}_{x,\mathrm{S}_0}$.

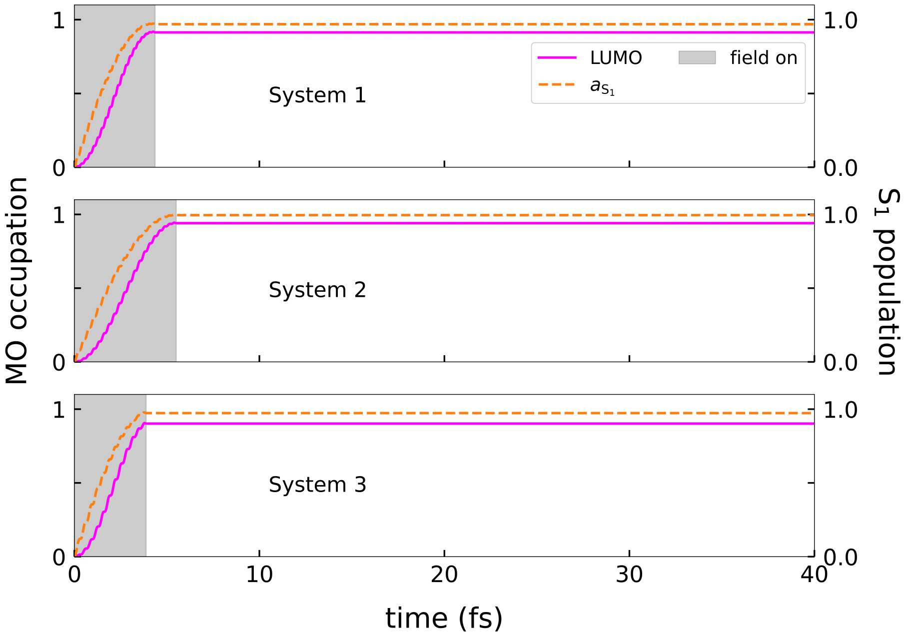

Figure A.7: TDCIS time-dependent occupations, obtained by projecting evolving MOs onto the initial set of MOs, and S_1 populations for TDCIS propagation plotted for different perturbations with systems initialized in S_0. The amplitudes of the perturbing fields are 0.01, 0.01, 0.01 a.u. and the fields are turned on for 10, 10, 6 cycles (gray area in the plot) for Systems 1, 2, and 3, respectively.

Table A.5: Peak-shifts, calculated as a percentage of the LR-TDHF $S_0 \rightarrow S_1$ transition energies, obtained as the difference between the RT-TDHF and LR-TDHF resonant peaks for Systems 1, 2, and 3. The percentage peak-shift value is unaffected by the system size within a numerical error of $\pm \sim 0.05$ eV.

TDHF	(eV)		%
	ω_{LR}	$\Delta\omega$	
System 1	8.95	0.85	~9.5
System 2	7.05	0.62	~8.8
System 3	5.99	0.57	~9.5

Appendix B

Chapter 3 Supplemental Information

Modeling the TDHF Hamiltonian

Canonical Orthogonalization

Let $\mathbf{S}$ be the overlap matrix with $S_{\mu\nu} = \langle \chi_\mu | \chi_\nu \rangle$. Because it is real and symmetric, we have $\mathbf{S} = \mathbf{U}\mathbf{s}\mathbf{U}^T$ where $\mathbf{s}$ is diagonal and real, and $\mathbf{U}$ is a real orthogonal matrix. Now we form $\mathbf{X} = \mathbf{U}\mathbf{s}^{-1/2}$. Then, we go from $\mathbf{P}$ to $\mathbf{P}'$ via

$$\mathbf{P}' = \mathbf{s}^{1/2}\mathbf{U}^T\mathbf{P}\mathbf{U}\mathbf{s}^{1/2}.$$

If $\mathbf{H}$ is the Hamiltonian in the AO basis, the Hamiltonian in the orthogonalized basis is

$$\mathbf{H}' = \mathbf{s}^{-1/2}\mathbf{U}^T\mathbf{H}\mathbf{U}\mathbf{s}^{-1/2}.$$

Modeling TDHF Hamiltonian of large systems

Dimensionality Reduction

We consider diatomic molecules in the 6-31G and 6-311++G** bases and the larger molecule C_2H_4 in the small STO-3G basis. Let N denote the dimension of the density and Hamiltonian matrices for each molecule in a given basis set. For larger basis sets or larger molecules, N^2 increases dramatically. We employ two tactics to reduce the dimensionality of β. First, we split Eq. (3.9) into two separate models, such that the parts of $\widetilde{\mathbf{h}}$ that correspond to real (respectively, imaginary) components of $\widetilde{\mathbf{H}}$ depend only on the real (respectively, imaginary) components of $\mathbf{P}$. This splitting, which can be justified based on physical properties of the Hartree-Fock Hamiltonian, was not present in our prior work [160]. At time $t_j = j\Delta t$, the true field-free Hamiltonian in the AO basis is,

$$\mathcal{H}^j = \mathcal{K} - \mathcal{N} + \mathcal{V}(\mathcal{P}^j). \tag{B.1}$$

Here $\mathcal{K}$ is the kinetic energy matrix, $\mathcal{N}$ is the electron-nuclear energy matrix, and $\mathcal{V}$ is the density-dependent combination of Coulomb and exchange matrices. Let $\mathcal{V}^j = \mathcal{V}(P^j)$, then for $u \leq v$,

$$\mathcal{V}^j_{u,v} = \sum_{l,s} 2\mathcal{P}^j_{l,s} \left(\mathcal{E}_{u,v,l,s} - \frac{1}{2}\mathcal{E}_{u,l,v,s} \right), \tag{B.2}$$

where $\mathcal{E}$ is a four-index tensor in the Coulomb and exchange calculations. Because this tensor is real, the real elements of the Hamiltonian depend on the real elements of the density-matrix and the imaginary elements of the Hamiltonian depend on the imaginary elements of the density-matrix. The second tactic used to reduce dimensionality is that when forming the flattened vector representation $\mathbf{h}$, we retain only those entries of $\mathbf{H}$ where the corresponding entries of $\mathbf{P}$ are not identically zero [160]. For these linear or flat molecular systems, elements are identically zero due to molecular symmetry, e.g., if they are constructed from orthogonal basis functions. In this way, for the largest problem under consideration, we reduce β from 842×841 to 226×225, reducing the number of coefficients by a factor > 13.9.

Ridge Regression

When we scale our method to molecular systems with large N, we also notice multicollinearity, e.g., numerous zero eigenvalues in the Hessian of the loss $\mathcal{L}$. With multicollinear data, the least squares estimator predicts poorly. We eliminate this problem by using ridge regression, for which we can write the penalized loss function as $\mathcal{L}_\lambda(\beta) = \mathcal{L}(\beta) + \lambda\|\beta\|_2^2$; note the use of the 2-norm, as opposed to the

1-norm in the penalty term for Lasso, i.e., $\lambda\|\beta\|_1$ [186]. In this work, we train our model by computing the ridge regression solution:

$$\beta_{\text{ridge}} = -\big(Q + 2\lambda I\big)^{-1} c^T, \tag{B.3}$$

where Q is the Hessian of $\mathcal{L}$ with respect to β and c is the gradient of $\mathcal{L}$ with respect to β computed at $\beta = 0$. For a grid of λ values, we compute β_{ridge} on the training set, and then compute the loss on a validation set that is disjoint from but equal in size to the training set.

The values of optimal λ are small ($\mathcal{O}(10^{-5})$ to $\mathcal{O}(10^{-2})$) but the propagation errors can be significantly lower depending on the λ value. This is rationalized in terms of accumulation and magnification of small one-step prediction errors (from Eq. (B.4)) in $\mathbf{P}(t)$ over thousands of timesteps used to calculate the propagation errors, as the commutator term in the Liouville-von Neumann equation depends quadratically on elements of $\mathbf{P}(t)$.

$$\widetilde{\mathbf{P}}_{j+1} = \mathbf{P}_{j-1} - 2i\Delta t\big[\widetilde{\mathbf{H}}(\mathbf{P}_j), \mathbf{P}_j\big] \tag{B.4}$$

Appendix C

Chapter 4 Supplemental Information

The CI Basis

Time-propagation using stationary CI states

The time-dependent configuration interaction (TDCI) wave-function is given by the superposition of stationary eigenstates of the exact Hamiltonian (denoted by $\hat{\mathcal{H}}$, from Eq. (2.10) in [7]), a set of CI states (Eq. (4.10)) evaluated such that every element of this set of wave-functions satisfies the time-independent Schrödinger equation:

$$\mathcal{H}\Psi_n^{\mathrm{CI}} = E_n \Psi_n^{\mathrm{CI}} \tag{C.1}$$

where E_n is the energy of the nth stationary state, the wave-function for which is given by Ψ_n^{CI}.

The TDCI wave-function can be thus written as (cf. Eq. (4.25)):

$$\Psi(\mathbf{x}_1, \mathbf{x}_2, \dots, t) = \sum_{A}^{\text{CI states}} a_A(t) \cdot \Psi_A^{\mathrm{CI}}(\mathbf{x}_1, \mathbf{x}_2, \dots) \tag{C.2}$$

The density corresponding to the multi-body wave-function above is given as:

$$\rho(\mathbf{x}_1, \mathbf{x}_2, \dots, t) = \Psi(\mathbf{x}_1, \mathbf{x}_2, \dots, t) \times \Psi^{\dagger}(\mathbf{x}_1, \mathbf{x}_2, \dots, t) \tag{C.3}$$

If we take the set of CI wave-functions as basis functions to represent the TDCI wave-function, we can represent $\Psi(\mathbf{x}_1, \mathbf{x}_2, \ldots, t)$ as a state-vector, $\vec{\Psi}(t)$:

$$\vec{\Psi}(t) = \begin{bmatrix} a_0(t) \\ a_1(t) \\ \vdots \\ a_i(t) \\ \vdots \\ a_f(t) \\ \vdots \end{bmatrix} \tag{C.4}$$

The corresponding density matrix (matrix representation of $\rho(\mathbf{x}_1, \mathbf{x}_2, \ldots, t)$) is given as an outer product of the state-vector:

$$\begin{aligned} \mathrm{P}_{\mathrm{CI}}^{\mathrm{TDCI}}(t) &= \vec{\Psi}(t) \times \vec{\Psi}^{\dagger}(t) \\ &= \begin{bmatrix} |a_0|^2(t) & a_0(t)a_1^*(t) & \ldots & a_0(t)a_i^*(t) & \ldots & a_0(t)a_f^*(t) & \ldots \\ a_1(t)a_0^*(t) & |a_1|^2(t) & \ldots & a_1(t)a_i^*(t) & \ldots & a_1(t)a_f^*(t) & \ldots \\ \vdots & \vdots & \ddots & \vdots & \ddots & \vdots & \ddots \\ a_i(t)a_0^*(t) & a_i(t)a_1^*(t) & \ldots & |a_i|^2(t) & \ldots & a_i(t)a_f^*(t) & \ldots \\ \vdots & \vdots & \ddots & \vdots & \ddots & \vdots & \ddots \\ a_f(t)a_0^*(t) & a_f(t)a_1^*(t) & \ldots & a_f(t)a_i^*(t) & \ldots & |a_f|^2(t) & \ldots \\ \vdots & \vdots & \ddots & \vdots & \ddots & \vdots & \ddots \end{bmatrix} \end{aligned} \tag{C.5}$$

We may choose to initiate the system by setting one of the CI state-coefficients, $\{a_{\mathrm{A}}(t)\}$, equal to 1. In the example of the HeH$^+$ TDCASSCF(2,2)/STO-3G system used above, we have three singlet CI states in the set of the CI basis functions. We choose to initiate the system in the S_0 state, and is perturbed at a frequency of the energy difference between S_0 and S_1. Thus, $a_0(0) = 1$, and the initial state-vector of the system is given by:

$$\vec{\Psi}(0) = \begin{bmatrix} 1.0 \\ 0.0 \\ 0.0 \end{bmatrix} \tag{C.6}$$

The corresponding density matrix in the CI basis is:

$$\mathrm{P}_{\mathrm{CI}}^{\mathrm{TDCI}}(0) = \begin{bmatrix} 1.0 & 0.0 & 0.0 \\ 0.0 & 0.0 & 0.0 \\ 0.0 & 0.0 & 0.0 \end{bmatrix} \tag{C.7}$$

The TDCI wave-function satisfies the time-dependent Schrödinger equation (TDSE) employing the dipole approximation for coupling of the electronic dipole operator with the applied electric field:

$$i\frac{\partial}{\partial t}\Psi(\mathbf{x}_1, \mathbf{x}_2, \ldots, t) = \left(\hat{\mathcal{H}} + \sum_{k}^{\{x,y,z\}} E_k(t) \times \hat{\mu}_k\right)\Psi(\mathbf{x}_1, \mathbf{x}_2, \ldots, t) \tag{C.8}$$

We use atomic units here. In matrix representation, the TDSE above can be re-written as:

$$i\frac{\partial}{\partial t}\vec{\Psi}(t) = \left(\mathbf{H} + \sum_{k} E_k(t)\upmu_k\right)\vec{\Psi}(t) \equiv \tilde{\mathbf{H}}(t)\vec{\Psi}(t) \tag{C.9}$$

where $\mathbf{d}_k$ is the dipole moment matrix along axis k. It is important to note that the Hamiltonian matrix, $\mathbf{H}$, is a diagonal matrix in the CI basis, owing to Eq. (C.1).

The solution (first-order term in the Magnus expansion[13]) to Eq. (C.9), for a discretized time-scale with a time-step Δt, is given by:

$$\vec{\Psi}(t+1) = \exp\left(-i\Delta t\tilde{\mathbf{H}}(t)\right)\vec{\Psi}(t) \tag{C.10}$$

Calculation of the elements of the dipole moment matrix

The $ij$the element of $\upmu_{k,\mathrm{CI}}$ is defined as:

$$[\upmu_{k,\mathrm{CI}}]_{ij} = \left\langle \Psi_i^{\mathrm{CI}} \left|\hat{\mu}_k\right| \Psi_j^{\mathrm{CI}} \right\rangle \tag{C.11}$$

This quantity can be calculated using matrices (represented in the AO basis) as follows:

$$[\upmu_{k,\mathrm{CI}}]_{ij} = \mathrm{Tr}\left(\mathrm{P}_{\mathrm{AO}}^{ij,\mathrm{CI}}\ \upmu_{k,\mathrm{AO}}\right) \tag{C.12}$$

(for a restricted reference, $\mathrm{P}_{\mathrm{AO}}^{ij,\mathrm{CI}} = \mathrm{P}_{\mathrm{AO},\alpha}^{ij,\mathrm{CI}} + \mathrm{P}_{\mathrm{AO},\beta}^{ij,\mathrm{CI}} = 2\mathrm{P}_{\mathrm{AO},\alpha}^{ij,\mathrm{CI}}$.)

Bibliography

[1] R. McWeeny. *An Overview of Molecular Quantum Mechanics*, pages 3–17. Springer US, 1992.

[2] Donald A. McQuarrie and John D. Simon. *Physical chemistry: a molecular approach.* University Science Books, 1997.

[3] Lucjan Piela, editor. *Ideas of Quantum Chemistry.* Elsevier, 2007.

[4] Rodney J. Bartlett and Monika Musiał. Coupled-cluster theory in quantum chemistry. *Rev. Mod. Phys.*, 79(1):291, 2007.

[5] Paul Hoerner, Mi Kyung Lee, and H. Bernhard Schlegel. Angular dependence of strong field ionization of N_2 by time-dependent configuration interaction using density functional theory and the Tamm-Dancoff approximation. *J. Chem. Phys.*, 151(5):054102, 2019.

[6] P. W. (Peter William) Atkins and Ronald Friedman. *Molecular quantum mechanics.* Oxford University Press, 5th ed. edition, 2011.

[7] Attila Szabo and Neil S. Ostlund. *Modern Quantum Chemistry: Introduction to Advanced Electronic Structure Theory.* Dover Publications, first edition, 1996.

[8] James B. Foresman, Martin Head-Gordon, John A. Pople, and Michael J. Frisch. Toward a systematic molecular orbital theory for excited states. *J. Phys. Chem.*, 96(1):135, 1992.

[9] C. David Sherrill and Henry F. Schaefer III. The configuration interaction method: Advances in highly correlated approaches. In *Advances in Quantum Chemistry*, pages 143–269. Elsevier, 1999.

[10] Jacob Townsend, Justin K. Kirkland, and Konstantinos D. Vogiatzis. Post-Hartree-Fock methods: configuration interaction, many-body perturbation theory, coupled-cluster theory. In *Mathematical Physics in Theoretical Chemistry*, pages 63–117. Elsevier, 2019.

[11] H. Bernhard Schlegel, Stanley M. Smith, and Xiaosong Li. Electronic optical response of molecules in intense fields: Comparison of TD-HF, TD-CIS, and TD-CIS(D) approaches. *J. Chem. Phys.*, 126(24):1, 2007.

[12] Fernando Casas and Arieh Iserles. Explicit Magnus expansions for nonlinear equations. *J. Phys. A: Mathematical and Theoretical*, 39(19):5445, 2006.

[13] S. Blanes, F. Casas, J. A. Oteo, and J. Ros. The Magnus expansion and some of its applications. *Phys. Rep.*, 470(5):151, 2009.

[14] David J. Tannor. *Introduction to Quantum Mechanics: A Time-Dependent Perspective.* University Science Books, 1st ed. edition, 2007.

[15] Pascal Krause, Tillmann Klamroth, and Peter Saalfrank. Time-dependent configuration-interaction calculations of laser-pulse-driven many-electron dynamics: Controlled dipole switching in lithium cyanide. *J. Chem. Phys.*, 123 (7):74105, 2005.

[16] Pascal Krause, Tillmann Klamroth, and Peter Saalfrank. Molecular response properties from explicitly time-dependent configuration interaction methods. *J. Chem. Phys.*, 127(3):034107, 2007.

[17] Jason A. Sonk, Marco Caricato, and H. Bernhard Schlegel. TD-CI simulation of the electronic optical response of molecules in intense fields: Comparison of RPA, CIS, CIS(D), and EOM-CCSD. *J. Phys. Chem. A*, 115(18):4678, 2011.

[18] Wei-Tao Tao Peng, B. Scott Fales, and Benjamin G. Levine. Simulating Electron Dynamics of Complex Molecules with Time-Dependent Complete Active Space Configuration Interaction. *J. Chem. Theory Comput.*, 14(8): 4129, 2018.

[19] Raghunathan Ramakrishnan. Charge-transfer selectivity and quantum interference in real-time electron dynamics: Gaining insights from time-dependent configuration interaction simulations. *J. Chem. Phys.*, 152(19):194111, 2020.

[20] Inga S. Ulusoy, Zachary Stewart, and Angela K. Wilson. The role of the CI expansion length in time-dependent studies. *J. Chem. Phys.*, 148(1):14107, 2018.

[21] Vladislav Kochetov and Sergey I. Bokarev. RhoDyn: A ρ-TD-RASCI framework to study ultrafast electron dynamics in molecules. *J. Chem. Theory Comput.*, 18(1):46, 2022.

[22] A. D. McLachlan and M. A. Ball. Time-Dependent Hartree-Fock Theory for Molecules. *Rev. Mod. Phys.*, 36(3):844, 1964.

[23] Xiaosong Li, Stanley M. Smith, Alexei N. Markevitch, Dmitri A. Romanov, Robert J. Levis, and H. Bernhard Schlegel. A time-dependent Hartree-Fock approach for studying the electronic optical response of molecules in intense fields. *Phys. Chem. Chem. Phys.*, 7(2):233, 2005.

[24] Wenkel Liang, Craig T. Chapman, and Xiaosong Li. Efficient first-principles electronic dynamics. *J. Chem. Phys.*, 134(18):184102, 2011.

[25] Adrián Gómez Pueyo, Miguel A. L. Marques, Angel Rubio, and Alberto Castro. Propagators for the Time-Dependent Kohn-Sham Equations: Multistep, Runge-Kutta, Exponential Runge-Kutta, and Commutator Free Magnus Methods. *J. Chem. Theory Comput.*, 14(6):3040, 2018.

[26] Ying Zhu and John M. Herbert. Self-consistent predictor/corrector algorithms for stable and efficient integration of the time-dependent Kohn-Sham equation. *J. Chem. Phys.*, 148(4):044117, 2018.

[27] Meilani Wibowo, Tom J. P. Irons, and Andrew M. Teale. Modeling Ultrafast Electron Dynamics in Strong Magnetic Fields Using Real-Time Time-Dependent Electronic Structure Methods. *J. Chem. Theory Comput.*, 17(4): 2137, 2021.

[28] David B. Williams-Young, Alessio Petrone, Shichao Sun, Torin F. Stetina, Patrick Lestrange, Chad E. Hoyer, Daniel R. Nascimento, Lauren Koulias, Andrew Wildman, Joseph Kasper, Joshua J. Goings, Feizhi Ding, A. Eugene DePrince, Edward F. Valeev, and Xiaosong Li. The Chronus Quantum software package. *Wiley Interdiscip. Rev.: Comput. Mol. Sci.*, 10(2):e1436, 2019.

[29] P. Hohenberg and W. Kohn. Inhomogeneous Electron Gas. *Phys. Rev.*, 136 (3B):B864, 1964.

[30] W. Kohn and L. J. Sham. Self-Consistent Equations Including Exchange and Correlation Effects. *Phys. Rev.*, 140(4A):A1133, 1965.

[31] Eberhard Engel and Reiner M. Dreizler. *Density functional theory.* Springer, Berlin, Germany, 2011.

[32] Kieron Burke. Perspective on density functional theory. *J. Chem. Phys.*, 136(15):150901, 2012.

[33] Kieron Burke and Lucas O. Wagner. DFT in a nutshell. *Int. J. Quantum Chem.*, 113(2):96, 2012.

[34] Erich Runge and E. K. U. Gross. Density-functional theory for time-dependent systems. *Phys. Rev. Lett.*, 52(12):997, 1984.

[35] Carsten A. Ullrich. *Time-Dependent Density-Functional Theory.* Oxford University Press, 2011.

[36] Miguel A. L. Marques, Neepa T. Maitra, Fernando Nogueira, Eberhard K. U. Gross, and Angel Rubio, editors. *Fundamentals of time-dependent density functional theory.* Springer, Berlin, Germany, 2012.

[37] Makenzie R. Provorse and Christine M. Isborn. Electron dynamics with real-time time-dependent density functional theory. *Int. J. Quantum Chem.*, 116 (10):739, 2016.

[38] Neepa T. Maitra. Perspective: Fundamental aspects of time-dependent density functional theory. *J. Chem. Phys.*, 144(22):220901, 2016.

[39] Davood Dar, Lionel Lacombe, and Neepa T. Maitra. The exact exchange–correlation potential in time-dependent density functional theory: Choreographing electrons with steps and peaks. *Chem. Phys. Rev.*, 3(3): 031307, 2022.

[40] Johanna I. Fuks, Kai Luo, Ernesto D. Sandoval, and Neepa T. Maitra. Time-Resolved Spectroscopy in Time-Dependent Density Functional Theory: An Exact Condition. *Phys. Rev. Lett.*, 114(18):183002, 2015.

[41] Lionel Lacombe and Neepa T. Maitra. Developing new and understanding old approximations in TDDFT. *Faraday Discuss.*, 224:382, 2020.

[42] Roi Baer. Prevalence of the adiabatic exchange-correlation potential approximation in time-dependent density functional theory. *J. Mol. Struct.: THEOCHEM*, 914(1):19, 2009.

[43] L. Mancini, J. D. Ramsden, M. J. P. Hodgson, and R. W. Godby. Adiabatic and local approximations for the Kohn-Sham potential in time-dependent Hubbard chains. *Phys. Rev. B*, 89(19):1, 2014.

[44] M. J. P. Hodgson and J. Wetherell. Accurate real-time evolution of electron densities and ground-state properties from generalized Kohn-Sham theory. *Phys. Rev. A*, 101(3):032502, 2020.

[45] Imam S. Wahyutama, Denawakage D. Jayasinghe, François Mauger, Kenneth Lopata, Mette B. Gaarde, and Kenneth J. Schafer. All-electron, density-functional-based method for angle-resolved tunneling ionization in the adiabatic regime. *Phys. Rev. A*, 106(5):052211, 2022.

[46] Neepa T. Maitra. Charge transfer in time-dependent density functional theory. *J. Phys.: Condens. Matter*, 29(42):423001, 2017.

[47] C. A. Ullrich and Kieron Burke. Excitation energies from time-dependent density-functional theory beyond the adiabatic approximation. *J. Chem. Phys.*, 121(1):28, 2004.

[48] H. O. Wijewardane and C. A. Ullrich. Time-Dependent Kohn-Sham Theory with Memory. *Phys. Rev. Lett.*, 95(8):086401, 2005.

[49] H. O. Wijewardane and C. A. Ullrich. Real-Time Electron Dynamics with Exact-Exchange Time-Dependent Density-Functional Theory. *Phys. Rev. Lett.*, 100(5):056404, 2008.

[50] Johanna I. Fuks, Lionel Lacombe, Søren E. B. Nielsen, and Neepa T. Maitra. Exploring non-adiabatic approximations to the exchange-correlation functional of TDDFT. *Phys. Chem. Chem. Phys.*, 20(41):26145, 2018.

[51] Robert van Leeuwen. Mapping from Densities to Potentials in Time-Dependent Density-Functional Theory. *Phys. Rev. Lett.*, 82(19):3863, 1999.

[52] Neepa T. Maitra, Kieron Burke, and Chris Woodward. Memory in Time-Dependent Density Functional Theory. *Phys. Rev. Lett.*, 89(2):023002, 2002.

[53] Neepa T. Maitra. Memory: History, Initial-State Dependence, and Double-Excitations. In *Fundamentals of Time-Dependent Density Functional Theory*, pages 167–184. Springer Berlin Heidelberg, 2012.

[54] Lionel Lacombe and Neepa T. Maitra. Density-matrix coupled time-dependent exchange-correlation functional approximations. *J. Chem. Theory Comput.*, 15(3):1672–1678, 2019.

[55] Graeme H. Gossel, Lionel Lacombe, and Neepa T. Maitra. On the numerical solution of the exact factorization equations. *J. Chem. Phys.*, 150(15):154112, 2019.

[56] E. K. U. Gross and Walter Kohn. Local Density-Functional Theory of Frequency-Dependent Linear Response. *Phys. Rev. Lett.*, 57:923–923, 1986.

[57] G. Vignale and Walter Kohn. Current-dependent exchange-correlation potential for dynamical linear response theory. *Phys. Rev. Lett.*, 77(10):2037–2040, 1996.

[58] E. K. U. Gross and Walter Kohn. Local density-functional theory of frequency-dependent linear response. *Phys. Rev. Lett.*, 55(26):2850–2852, 1985.

[59] C. A. Ullrich and G. Vignale. Time-dependent current-density-functional theory for the linear response of weakly disordered systems. *Phys. Rev. B*, 65(24), 2002.

[60] C. A. Ullrich. Time-dependent density-functional theory beyond the adiabatic approximation: Insights from a two-electron model system. *J. Chem. Phys.*, 125(23):234108, 2006.

[61] Lucas O. Wagner, Zeng hui Yang, and Kieron Burke. Exact conditions and their relevance in TDDFT. In *Fundamentals of Time-Dependent Density Functional Theory*, pages 101–123. Springer Berlin Heidelberg, 2012.

[62] M. Thiele, E. K U Gross, and S Kümmel. Adiabatic Approximation in Nonperturbative Time-Dependent Density-Functional Theory. *Phys. Rev. Lett.*, 100(15):153004, 2008.

[63] A. S. de Wijn, M. Lein, and S. Kümmel. Strong-field ionization in time-dependent density functional theory. *EPL (Europhysics Letters)*, 84(4): 43001, 2008.

[64] Kenneth Lopata and Niranjan Govind. Modeling Fast Electron Dynamics with Real-Time Time-Dependent Density Functional Theory: Application to Small Molecules and Chromophores. *J. Chem. Theory Comput.*, 7(5):1344, 2011.

[65] Yasumitsu Suzuki, Lionel Lacombe, Kazuyuki Watanabe, and Neepa T. Maitra. Exact time-dependent exchange-correlation potential in electron scattering processes. *Phys. Rev. Lett.*, 119:263401, 2017.

[66] P. Elliott, J. I. Fuks, A. Rubio, and N. T. Maitra. Universal dynamical steps in the exact time-dependent exchange-correlation potential. *Phys. Rev. Lett.*, 109(26), 2012.

[67] J. I. Fuks, P. Elliott, A. Rubio, and N. T. Maitra. Dynamics of Charge-Transfer Processes with Time-Dependent Density Functional Theory. *J. Phys. Chem. Lett.*, 4(5):735, 2013.

[68] Makenzie R. Provorse, Bradley F. Habenicht, and Christine M. Isborn. Peak-Shifting in Real-Time Time-Dependent Density Functional Theory. *J. Chem. Theory Comput.*, 11(10):4791, 2015.

[69] Kai Luo, Johanna I. Fuks, and Neepa T. Maitra. Studies of spuriously shifting resonances in time-dependent density functional theory. *J. Chem. Phys.*, 145 (4):044101, 2016.

[70] A. Seidl, A. Görling, P. Vogl, J. A. Majewski, and M. Levy. Generalized Kohn-Sham schemes and the band-gap problem. *Phys. Rev. B*, 53(7):3764, 1996.

[71] Roi Baer and Leeor Kronik. Time-dependent generalized Kohn-Sham theory. *Eur. Phys. J. B*, 91(7):paper no. 170, 2018.

[72] Christine M. Isborn and Xiaosong Li. Modeling the doubly excited state with time-dependent Hartree–Fock and density functional theories. *J. Chem. Phys.*, 129(20):204107, 2008.

[73] So Hirata and Martin Head-Gordon. Time-dependent density functional theory within the Tamm-Dancoff approximation. *Chem. Phys. Lett.*, 314(3): 291, 1999.

[74] Felipe Cordova, L. Joubert Doriol, Andrei Ipatov, Mark E. Casida, Claudia Filippi, and Alberto Vela. Troubleshooting time-dependent density-functional theory for photochemical applications: Oxirane. *J. Chem. Phys.*, 127(16):164111, 2007.

[75] Christine M. Isborn, Nathan Luehr, Ivan S. Ufimtsev, and Todd J. Martínez. Excited-State Electronic Structure with Configuration Interaction Singles and Tamm-Dancoff Time-Dependent Density Functional Theory on Graphical Processing Units. *J. Chem. Theory Comput.*, 7(6):1814, 2011.

[76] Joseph E. Subotnik. Communication: Configuration interaction singles has a large systematic bias against charge-transfer states. *J. Chem. Phys.*, 135 (7):071104, 2011.

[77] Stefan Grimme. A simplified Tamm-Dancoff density functional approach for the electronic excitation spectra of very large molecules. *J. Chem. Phys.*, 138(24):244104, 2013.

[78] Karnamohit Ranka and Christine M. Isborn. Size-dependent errors in real-time electron density propagation. *J. Chem. Phys.*, 158(17):174102, 2023.

[79] H. Flocard, S. E. Koonin, and M. S. Weiss. Three-dimensional time-dependent Hartree-Fock calculations: Application to $^{16}\mathrm{O} + {}^{16}\mathrm{O}$ collisions. *Phys. Rev. C*, 17(5):1682, 1978.

[80] Kazuyuki Sekizawa. TDHF Theory and Its Extensions for the Multinucleon Transfer Reaction: A Mini Review. *Front. Phys.*, 7:paper no. 20, 2019.

[81] Henk Eshuis, Gabriel G. Balint-Kurti, and Frederick R. Manby. Dynamics of molecules in strong oscillating electric fields using time-dependent Hartree-Fock theory. *J. Chem. Phys.*, 128(11):114113, 2008.

[82] Christine M. Isborn and Xiaosong Li. Singlet-Triplet Transitions in Real-Time Time-Dependent Hartree-Fock/Density Functional Theory. *J. Chem. Theory Comput.*, 5(9):2415, 2009.

[83] Umberto De Giovannini, Gustavo Brunetto, Alberto Castro, Jessica Walkenhorst, and Angel Rubio. Simulating Pump-Probe Photoelectron and Absorption Spectroscopy on the Attosecond Timescale with Time-Dependent Density Functional Theory. *ChemPhysChem*, 14(7):1363, 2013.

[84] Abhisek Ghosal and Amlan K. Roy. A real-time TDDFT scheme for strong-field interaction in Cartesian coordinate grid. *Chem. Phys. Lett.*, 796:139562, 2022.

[85] John Heslar, Dmitry A. Telnov, and Shih-I Chu. Subcycle dynamics of high-harmonic generation in valence-shell and virtual states of Ar atoms: A self-interaction-free time-dependent density-functional-theory approach. *Phys. Rev. A*, 91(2):023420, 2015.

[86] Emanuele Coccia and Eleonora Luppi. Time-dependent ab initio approaches for high-harmonic generation spectroscopy. *J. Phys.: Condens. Matter*, 34 (7):073001, 2021.

[87] Carlo Andrea Rozzi, Sarah Maria Falke, Nicola Spallanzani, Angel Rubio, Elisa Molinari, Daniele Brida, Margherita Maiuri, Giulio Cerullo, Heiko Schramm, Jens Christoffers, Christoph Lienau, Carlo Andrea Rozzi, Sarah Maria Falke, Nicola Spallanzani, Angel Rubio, Elisa Molinari, Daniele Brida, Margherita Maiuri, Giulio Cerullo, Heiko Schramm, Jens Christoffers, and Christoph Lienau. Quantum coherence controls the charge separation in a prototypical artificial light-harvesting system. *Nat. Commun.*, 4(1):1602, 2013.

[88] Sarah M. Falke, Carlo A. Rozzi, Daniele Brida, Margherita Maiuri, Michele Amato, Ephraim Sommer, A. De Sio, Angel Rubio, Giulio Cerullo, Elisa Molinari, and Christoph Lienau. Coherent ultrafast charge transfer in an organic photovoltaic blend. *Science*, 344(6187):1001, 2014.

[89] Sean A. Fischer, Christopher J. Cramer, and Niranjan Govind. Excited State Absorption from Real-Time Time-Dependent Density Functional Theory. *J. Chem. Theory Comput.*, 11(9):4294, 2015.

[90] Adam Bruner, Samuel Hernandez, François Mauger, Paul M. Abanador, Daniel J. LaMaster, Mette B. Gaarde, Kenneth J. Schafer, and Kenneth Lopata. Attosecond Charge Migration with TDDFT: Accurate Dynamics from a Well-Defined Initial State. *J. Phys. Chem. Lett.*, 8(17):3991, 2017.

[91] T. Trepl, I. Schelter, and S. Kümmel. Analyzing Excitation-Energy Transfer Based on the Time-Dependent Density Functional Theory in Real Time. *J. Chem. Theory Comput.*, 18(11):6577, 2022.

[92] Adonay Sissay, Paul Abanador, François Mauger, Mette Gaarde, Kenneth J. Schafer, and Kenneth Lopata. Angle-dependent strong-field molecular ionization rates with tuned range-separated time-dependent density functional theory. *J. Chem. Phys.*, 145(9):094105, 2016.

[93] Tomoko Akama and Hiromi Nakai. Short-time Fourier transform analysis of real-time time-dependent Hartree–Fock and time-dependent density functional theory calculations with Gaussian basis functions. *J. Chem. Phys.*, 132(5):054104, 2010.

[94] Adam Bruner, Stefano M. Cavaletto, Niranjan Govind, and Shaul Mukamel. Resonant X-ray Sum-Frequency-Generation Spectroscopy of K-Edges in Acetyl Fluoride. *J. Chem. Theory Comput.*, 15(12):6832, 2019.

[95] Min Chen and Kenneth Lopata. First-Principles Simulations of X-ray Transient Absorption for Probing Attosecond Electron Dynamics. *J. Chem. Theory Comput.*, 16(7):4470, 2020.

[96] Tuomas P. Rossi, Mikael Kuisma, Martti J. Puska, Risto M. Nieminen, and Paul Erhart. Kohn-Sham Decomposition in Real-Time Time-Dependent Density-Functional Theory: An Efficient Tool for Analyzing Plasmonic Excitations. *J. Chem. Theory Comput.*, 13(10):4779, 2017.

[97] Jannis Krumland, Ana M. Valencia, Stefano Pittalis, Carlo A. Rozzi, and Caterina Cocchi. Understanding real-time time-dependent density-functional

theory simulations of ultrafast laser-induced dynamics in organic molecules. *J. Chem. Phys.*, 153(5):054106, 2020.

[98] Andreas Dreuw. Quantum Chemical Methods for the Investigation of Photoinitiated Processes in Biological Systems: Theory and Applications. *ChemPhysChem*, 7(11):2259, 2006.

[99] Johann Mattiat and Sandra Luber. Recent Progress in the Simulation of Chiral Systems with Real Time Propagation Methods. *Helv. Chim. Acta*, 104(12):e2100154, 2021.

[100] Johann Mattiat and Sandra Luber. Comparison of Length, Velocity, and Symmetric Gauges for the Calculation of Absorption and Electric Circular Dichroism Spectra with Real-Time Time-Dependent Density Functional Theory. *J. Chem. Theory Comput.*, 18(9):5513, 2022.

[101] Erik W. Draeger, Xavier Andrade, John A. Gunnels, Abhinav Bhatele, André Schleife, and Alfredo A. Correa. Massively parallel first-principles simulation of electron dynamics in materials. *J. Parallel Distrib. Comput.*, 106:205, 2017.

[102] Gowri U. Kuda-Singappulige and Christine M. Aikens. Excited-State Absorption in Silver Nanoclusters. *J. Phys. Chem. C*, 125(45):24996, 2021.

[103] Luke Bhan, Cody Covington, and Kálmán Varga. Signatures of atomic structure in subfemtosecond laser-driven electron dynamics in nanogaps. *Phys. Rev. B*, 105(8):085416, 2022.

[104] Christopher Shepard, Ruiyi Zhou, Dillon C. Yost, Yi Yao, and Yosuke Kanai. Simulating electronic excitation and dynamics with real-time propagation approach to TDDFT within plane-wave pseudopotential formulation. *J. Chem. Phys.*, 155(10):100901, 2021.

[105] Alina Kononov, Cheng-Wei Lee, Tatiane Pereira dos Santos, Brian Robinson, Yifan Yao, Yi Yao, Xavier Andrade, Andrew David Baczewski, Emil Constantinescu, Alfredo A. Correa, Yosuke Kanai, Normand Modine, and

André Schleife. Electron dynamics in extended systems within real-time time-dependent density-functional theory. *MRS Commun.*, 12(6):1002, 2022.

[106] Shunsuke Yamada, Masashi Noda, Katsuyuki Nobusada, and Kazuhiro Yabana. Time-dependent density functional theory for interaction of ultrashort light pulse with thin materials. *Phys. Rev. B*, 98(24):245147, 2018.

[107] Tor S. Haugland, Christian Schäfer, Enrico Ronca, Angel Rubio, and Henrik Koch. Intermolecular interactions in optical cavities: An ab initio QED study. *J. Chem. Phys.*, 154(9):094113, 2021.

[108] Chang-Kai Li, Jian-ming Xue, and Feng-Shou Zhang. Channeling electronic stopping power of lithium ions in diamond: Contribution of projectile inner-shell electrons. *Phys. Rev. A*, 106(2):022807, 2022.

[109] M. T. Entwistle and R. W. Godby. Exact nonadiabatic part of the Kohn-Sham potential and its fluidic approximation. *Phys. Rev. Materials*, 4(3): 035002, 2020.

[110] Bradley F. Habenicht, Noriyuki P. Tani, Makenzie R. Provorse, and Christine M. Isborn. Two-electron Rabi oscillations in real-time time-dependent density-functional theory. *J. Chem. Phys.*, 141(18):184112, 2014.

[111] M. Ruggenthaler and D. Bauer. Rabi Oscillations and Few-Level Approximations in Time-Dependent Density Functional Theory. *Phys. Rev. Lett.*, 102(23):233001, 2009.

[112] Shampa Raghunathan and Mathias Nest. The Lack of Resonance Problem in Coherent Control with Real-Time Time-Dependent Density Functional Theory. *J. Chem. Theory Comput.*, 8(3):806, 2012.

[113] Davood Dar, Lionel Lacombe, Johannes Feist, and Neepa T. Maitra. Exact time-dependent density-functional theory for nonperturbative dynamics of the helium atom. *Phys. Rev. A*, 104(3):032821, 2021.

[114] Axel D. Becke. Density-functional thermochemistry. III. The role of exact exchange. *J. Chem. Phys.*, 98(7):5648, 1993.

[115] P. J. Stephens, F. J. Devlin, C. F. Chabalowski, and M. J. Frisch. Ab Initio Calculation of Vibrational Absorption and Circular Dichroism Spectra Using Density Functional Force Fields. *J. Phys. Chem.*, 98(45):11623, 1994.

[116] Benjamin P. Pritchard, Doaa Altarawy, Brett Didier, Tara D. Gibson, and Theresa L. Windus. New Basis Set Exchange: An Open, Up-to-Date Resource for the Molecular Sciences Community. *J. Chem. Inf. Model.*, 59(11): 4814, 2019.

[117] M. J. Frisch, G. W. Trucks, H. B. Schlegel, G. E. Scuseria, M. A. Robb, J. R. Cheeseman, G. Scalmani, V. Barone, G. A. Petersson, H. Nakatsuji, X. Li, M. Caricato, A. V. Marenich, J. Bloino, B. G. Janesko, R. Gomperts, B. Mennucci, H. P. Hratchian, J. V. Ortiz, A. F. Izmaylov, J. L. Sonnenberg, D. Williams-Young, F. Ding, F. Lipparini, F. Egidi, J. Goings, B. Peng, A. Petrone, T. Henderson, D. Ranasinghe, V. G. Zakrzewski, J. Gao, N. Rega, G. Zheng, W. Liang, M. Hada, M. Ehara, K. Toyota, R. Fukuda, J. Hasegawa, M. Ishida, T. Nakajima, Y. Honda, O. Kitao, H. Nakai, T. Vreven, K. Throssell, J. A. Montgomery, Jr., J. E. Peralta, F. Ogliaro, M. J. Bearpark, J. J. Heyd, E. N. Brothers, K. N. Kudin, V. N. Staroverov, T. A. Keith, R. Kobayashi, J. Normand, K. Raghavachari, A. P. Rendell, J. C. Burant, S. S. Iyengar, J. Tomasi, M. Cossi, J. M. Millam, M. Klene, C. Adamo, R. Cammi, J. W. Ochterski, R. L. Martin, K. Morokuma, O. Farkas, J. B. Foresman, and D. J. Fox. Gaussian Development Version Revision I.14+, 2018. Gaussian Inc. Wallingford CT.

[118] Michael W. Schmidt and Mark S. Gordon. The Construction and Interpretation of MCSCF Wavefunctions. *Ann. Rev. Phys. Chem.*, 49(1):233, 1998.

[119] Jeanne L. McHale. *Molecular Spectroscopy.* CRC Press, 2017.

[120] J. I. Fuks, N. Helbig, I. V. Tokatly, and A. Rubio. Nonlinear phenomena in time-dependent density-functional theory: What Rabi oscillations can teach us. *Phys. Rev. B*, 84(7):075107, 2011.

[121] John C. Snyder, Matthias Rupp, Katja Hansen, Klaus Robert Müller, and Kieron Burke. Finding density functionals with machine learning. *Phys. Rev. Lett.*, 108(25):1–5, 2012.

[122] Grégoire Montavon, Matthias Rupp, Vivekanand Gobre, Alvaro Vazquez-Mayagoitia, Katja Hansen, Alexandre Tkatchenko, Klaus Robert Müller, and O. Anatole Von Lilienfeld. Machine learning of molecular electronic properties in chemical compound space. *New J. Phys.*, 15:095003, 2013.

[123] Raghunathan Ramakrishnan, Mia Hartmann, Enrico Tapavicza, and O Anatole von Lilienfeld. Electronic spectra from TDDFT and machine learning in chemical space. *J. Chem. Phys.*, 143:084111, 2015.

[124] Florian Häse, Stéphanie Valleau, Edward Pyzer-Knapp, and Alán Aspuru-Guzik. Machine learning exciton dynamics. *Chem. Sci.*, 7(8):5139–5147, 2016.

[125] Michael Gastegger, Jörg Behler, and Philipp Marquetand. Machine learning molecular dynamics for the simulation of infrared spectra. *Chem. Sci.*, 8(10): 6924–6935, 2017.

[126] Albert P. Bartók, Sandip De, Carl Poelking, Noam Bernstein, James R. Kermode, Gábor Csányi, and Michele Ceriotti. Machine learning unifies the modeling of materials and molecules. *Sci. Adv.*, 3(12), 2017.

[127] Wen Kai Chen, Xiang Yang Liu, Wei Hai Fang, Pavlo O. Dral, and Ganglong Cui. Deep Learning for Nonadiabatic Excited-State Dynamics. *J. Phys. Chem. Lett.*, 9(23):6702–6708, 2018.

[128] Hiroyuki Fujita, Yuya O. Nakagawa, Sho Sugiura, and Masaki Oshikawa. Construction of Hamiltonians by supervised learning of energy and entanglement spectra. *Phys. Rev. B*, 97:075114, 2018.

[129] Andrea Grisafi, David M. Wilkins, Gábor Csányi, and Michele Ceriotti. Symmetry-Adapted Machine Learning for Tensorial Properties of Atomistic Systems. *Phys. Rev. Lett.*, 120(3):36002, 2018.

[130] Benjamin Nebgen, Nicholas Lubbers, Justin S. Smith, Andrew E. Sifain, Andrey Lokhov, Olexandr Isayev, Adrian E. Roitberg, Kipton Barros, and Sergei Tretiak. Transferable Dynamic Molecular Charge Assignment Using Deep Neural Networks. *J. Chem. Theory Comput.*, 14(9):4687–4698, 2018.

[131] Federico M. Paruzzo, Albert Hofstetter, Félix Musil, Sandip De, Michele Ceriotti, and Lyndon Emsley. Chemical shifts in molecular solids by machine learning. *Nat. Commun.*, 9:4501, 2018.

[132] Wiktor Pronobis, Kristof T. Schütt, Alexandre Tkatchenko, and Klaus Robert Müller. Capturing intensive and extensive DFT/TDDFT molecular properties with machine learning. *Eur. Phys. J. B*, 91(8):178–184, 2018.

[133] Andrew E. Sifain, Nicholas Lubbers, Benjamin T. Nebgen, Justin S. Smith, Andrey Y. Lokhov, Olexandr Isayev, Adrian E. Roitberg, Kipton Barros, and Sergei Tretiak. Discovering a Transferable Charge Assignment Model Using Machine Learning. *J. Phys. Chem. Lett.*, 9(16):4495–4501, 2018.

[134] Mirta Rodríguez and Tobias Kramer. Machine learning of two-dimensional spectroscopic data. *Chem. Phys.*, 520:52–60, 2019.

[135] Anders S. Christensen, Felix A. Faber, and O. Anatole Von Lilienfeld. Operators in quantum machine learning: Response properties in chemical space. *J. Chem. Phys.*, 150(6):064105, 2019.

[136] Kunal Ghosh, Annika Stuke, Milica Todorović, Peter Bjørn Jørgensen, Mikkel N. Schmidt, Aki Vehtari, and Patrick Rinke. Deep Learning Spectroscopy: Neural Networks for Molecular Excitation Spectra. *Adv. Sci.*, 6 (9):1801367–1801374, 2019.

[137] David M. Wilkins, Andrea Grisafi, Yang Yang, Ka Un Lao, Robert A. DiStasio, and Michele Ceriotti. Accurate molecular polarizabilities with coupled cluster theory and machine learning. *Proc. Natl. Acad. Sci. U. S. A.*, 116(9): 3401–3406, 2019.

[138] Sheng Ye, Wei Hu, Xin Li, Jinxiao Zhang, Kai Zhong, Guozhen Zhang, Yi Luo, Shaul Mukamel, and Jun Jiang. A neural network protocol for electronic excitations of N-methylacetamide. *Proc. Natl. Acad. Sci. U. S. A.*, 116(24):11612–11617, 2019.

[139] Anand Chandrasekaran, Deepak Kamal, Rohit Batra, Chiho Kim, Lihua Chen, and Rampi Ramprasad. Solving the electronic structure problem with machine learning. *NPJ Comput. Mater.*, 5(1), 2019.

[140] Gabriel R Schleder, Antonio C M Padilha, Carlos Mera Acosta, Marcio Costa, and Adalberto Fazzio. From DFT to machine learning: recent approaches to materials science–a review. *J. Phys.: Materials*, 2(3):032001, 2019.

[141] Mathias S. Jørgensen, Henrik L. Mortensen, Søren A. Meldgaard, Esben L. Kolsbjerg, Thomas L. Jacobsen, Knud H. Sørensen, and Bjørk Hammer. Atomistic structure learning. *J. Chem. Phys.*, 2019.

[142] Justin S. Smith, Benjamin T. Nebgen, Roman Zubatyuk, Nicholas Lubbers, Christian Devereux, Kipton Barros, Sergei Tretiak, Olexandr Isayev, and Adrian E. Roitberg. Approaching coupled cluster accuracy with a general-purpose neural network potential through transfer learning. *Nat. Commun.*, 2019.

[143] Michele Ceriotti. Unsupervised machine learning in atomistic simulations, between predictions and understanding. *J. Chem. Phys.*, 150(15), 2019.

[144] Chengqiang Lu, Qi Liu, Qiming Sun, Chang-Yu Hsieh, Shengyu Zhang, Liang Shi, and Chee-Kong Lee. Deep Learning for Optoelectronic Properties of Organic Semiconductors. *J. Phys. Chem. C*, 124:7048–7060, 2020.

[145] Joshua J. Goings, Hang Hu, Chao Yang, and Xiaosong Li. Reinforcement learning configuration interaction. *J. Chem. Theory Comput.*, 17(9):5482–5491, 2021.

[146] Guoqing Zhou, Nicholas Lubbers, Kipton Barros, Sergei Tretiak, and Benjamin Nebgen. Deep learning of dynamically responsive chemical hamiltonians with semiempirical quantum mechanics. *Proc. Natl. Acad. Sci. U. S. A.*, 119(27), 2022.

[147] Basile Herzog, Bastien Casier, Sébastien Lebègue, and Dario Rocca. Solving the schrödinger equation in the configuration space with generative machine learning. *J. Chem. Theory Comput.*, 19(9):2484–2490, 2023.

[148] Nongnuch Artrith, Tobias Morawietz, and Jörg Behler. High-dimensional neural-network potentials for multicomponent systems: Applications to zinc oxide. *Phys. Rev. B*, 83(15):153101, 2011.

[149] Jörg Behler and Michele Parrinello. Generalized neural-network representation of high-dimensional potential-energy surfaces. *Phys. Rev. Lett.*, 98(14): 146401, 2007.

[150] J. S. Smith, O. Isayev, and A. E. Roitberg. ANI-1: an extensible neural network potential with DFT accuracy at force field computational cost. *Chem. Sci.*, 8(4):3192–3203, 2017.

[151] Bastiaan J Braams and Joel M Bowman. Permutationally invariant potential energy surfaces in high dimensionality. *Int. Rev. Phys. Chem.*, 28(4):577–606, 2009.

[152] Alexis W. Mills, Joshua J. Goings, David Beck, Chao Yang, and Xiaosong Li. Exploring potential energy surfaces using reinforcement machine learning. *J. Chem. Inf. Model.*, 62(13):3169–3179, 2022.

[153] Fenris Lu, Lixue Cheng, Ryan J. DiRisio, Jacob M. Finney, Mark A. Boyer, Pattarapon Moonkaen, Jiace Sun, Sebastian J. R. Lee, J. Emiliano Deustua, Thomas F. Miller, and Anne B. McCoy. Fast Near *Ab Initio* Potential Energy Surfaces Using Machine Learning. *J. Phys. Chem. A*, 126(25):4013–4024, 2022.

[154] Gunnar Schmitz, Ian Heide Godtliebsen, and Ove Christiansen. Machine learning for potential energy surfaces: An extensive database and assessment of methods. *J. Chem. Phys.*, 150(24):244113, 2019.

[155] Oliver T Unke, Debasish Koner, Sarbani Patra, Silvan Käser, and Markus Meuwly. High-dimensional potential energy surfaces for molecular simulations: from empiricism to machine learning. *Mach. Learn.: Sci. Technol.*, 1 (1):013001, 2020.

[156] Apurba Nandi, Chen Qu, Paul L. Houston, Riccardo Conte, and Joel M. Bowman. δ-machine learning for potential energy surfaces: A PIP approach to bring a DFT-based PES to CCSD(t) level of theory. *J. Chem. Phys.*, 154 (5):051102, 2021.

[157] Geng Sun and Philippe Sautet. Toward fast and reliable potential energy surfaces for metallic pt clusters by hierarchical delta neural networks. *J. Chem. Theory Comput.*, 15(10):5614–5627, 2019.

[158] Apoorv Kushwaha and Thogluva Janardhanan Dhilip Kumar. Benchmarking PES-learn's machine learning models predicting accurate potential energy surface for quantum scattering. *Int. J. Quantum Chem.*, 123(1), 2022.

[159] Apurba Nandi. *Development of Machine-Learned Potential Energy Surfaces with Application to the Reactive and Vibrational Dynamics of High Dimensional Molecular Systems.* PhD thesis, Emory University, 2022.

[160] H. S. Bhat, K. Ranka, and C. M. Isborn. Machine learning a molecular Hamiltonian for predicting electron dynamics. *Int. J. Dyn. Control*, 8(4): 1089, 2020.

[161] David A. Micha and Keith Runge. Time-dependent many-electron approach to slow ion-atom collisions: The coupling of electronic and nuclear motions. *Phys. Rev. A*, 50:322–336, 1994.

[162] Andreas Dreuw and Martin Head-Gordon. Single-reference ab initio methods

for the calculation of excited states of large molecules. *Chem. Rev.*, 105(11): 4009–4037, 2005. hidePMID: 16277369.

[163] Christine M. Isborn, Xiaosong Li, and John C. Tully. TDDFT Ehrenfest dynamics: Collisions between atomic oxygen and graphite clusters. *J. Chem. Phys.*, 126:134307, 2007.

[164] Henk Eshuis, Gabriel G Balint-Kurti, and Frederick R Manby. Dynamics of molecules in strong oscillating electric fields using time-dependent Hartree–Fock theory. *J. Chem. Phys.*, 128(11):114113, 2008.

[165] Ying Zhu and John M Herbert. Self-consistent predictor/corrector algorithms for stable and efficient integration of the time-dependent Kohn-Sham equation. *J. Chem. Phys.*, 148(4):044117, 2018.

[166] Daniel R. Nascimento and A. Eugene DePrince III. Linear absorption spectra from explicitly time-dependent equation-of-motion coupled-cluster theory. *J. Chem. Theory Comput.*, 12(12):5834–5840, 2016.

[167] Tom Bertalan, Felix Dietrich, Igor Mezić, and Ioannis G. Kevrekidis. On learning Hamiltonian systems from data. *Chaos: An Interdisciplinary Journal of Nonlinear Science*, 29(12):121107, 2019.

[168] Harish S. Bhat. Learning and interpreting potentials for classical Hamiltonian systems. In P. Cellier and K. Driessens, editors, *Machine Learning and Knowledge Discovery in Databases. ECML PKDD 2019*. Springer, 2020. Communications in Computer and Information Science **1167**.

[169] Danilo Jimenez Rezende, Sébastien Racanière, Irina Higgins, and Peter Toth. Equivariant Hamiltonian flows. arXiv:1909.13739, 2019.

[170] Zhengdao Chen, Jianyu Zhang, Martin Arjovsky, and Léon Bottou. Symplectic recurrent neural networks. In *8th International Conference on Learning Representations, ICLR 2020*, 2020.

[171] Pengzhan Jin, Zhen Zhang, Aiqing Zhu, Yifa Tang, and George Em Karniadakis. Sympnets: Intrinsic structure-preserving symplectic networks for identifying Hamiltonian systems. arXiv:2001.03750, 2020.

[172] Scott T. Miller, John F. Lindner, Anshul Choudhary, Sudeshna Sinha, and William L. Ditto. Mastering high-dimensional dynamics with Hamiltonian neural networks. arXiv:2008.04214, 2020.

[173] Marios Mattheakis, David Sondak, Akshunna S. Dogra, and Pavlos Protopapas. Hamiltonian Neural Networks for solving differential equations. arXiv:2001.11107, 2020.

[174] Peter Toth, Danilo Jimenez Rezende, Andrew Jaegle, Sébastien Racanière, Aleksandar Botev, and Irina Higgins. Hamiltonian generative networks. In *8th International Conference on Learning Representations, ICLR 2020*, 2020.

[175] Yaofeng D. Zhong, Biswadip Dey, and Amit Chakraborty. Symplectic ODE-Net: Learning Hamiltonian Dynamics with Control. In *8th International Conference on Learning Representations, ICLR 2020*, 2020.

[176] Jorg Behler. Perspective: Machine learning potentials for atomistic simulations. *J. Chem. Phys.*, 145(17):170901, 2016.

[177] Haichen Li, Christopher Collins, Matteus Tanha, Geoffrey J. Gordon, and David J. Yaron. A density functional tight binding layer for deep learning of chemical Hamiltonians. *J. Chem. Theory Comput.*, 14(11):5764–5776, 2018.

[178] Luca Innocenti, Leonardo Banchi, Alessandro Ferraro, Sougato Bose, and Mauro Paternostro. Supervised learning of time-independent Hamiltonians for gate design. *New J. Phys.*, 22(6):065001, 2020.

[179] Yasumitsu Suzuki, Ryo Nagai, and Jun Haruyama. Machine learning exchange-correlation potential in time-dependent density-functional theory. *Phys. Rev. A*, 101:050501, 2020.

[180] P. A. M. Dirac. Note on Exchange Phenomena in the Thomas Atom. *Math. Proc. Camb. Philos. Soc.*, 26(3):376–385, 1930.

[181] Prachi Gupta, Harish S. Bhat, Karnamohit Ranka, and Christine M. Isborn. Statistical learning for predicting density–matrix-based electron dynamics. *Stat*, 11(1):e439, 2022.

[182] J.R. Dormand and P.J. Prince. A family of embedded Runge-Kutta formulae. *J. Comput. Appl. Math.*, 6(1):19–26, 1980.

[183] Xiaosong Li, Niranjan Govind, Christine Isborn, A. Eugene III DePrince, and Kenneth Lopata. Real-Time Time-Dependent Electronic Structure Theory. *Chem. Rev.*, 120(18):9951, 2020.

[184] Harish S Bhat, Prachi Gupta, and Karnamohit Ranka. Electron Dynamics. `https://github.com/hbhat4000/electrondynamics`, 2021.

[185] Aleksander P. Woźniak, Maciej Lewenstein, and Robert Moszyński. Chapter Three - Exploring the attosecond laser-driven electron dynamics in the hydrogen molecule with different real-time time-dependent configuration interaction approaches. In Monika Musiał and Ireneusz Grabowski, editors, *Polish Quantum Chemistry from Kołos to Now*, volume 87 of *Adv. Quantum Chem.*, pages 167–190. Academic Press, 2023.

[186] Trevor Hastie, Robert Tibshirani, and Jerome Friedman. *The Elements of Statistical Learning*. Springer, 2001.